Stony Brook University

OFFICIAL COPY

The official electronic file of this thesis or dissertation is maintained by the University Libraries on behalf of The Graduate School at Stony Brook University.

© All Rights Reserved by Author.

Development of Novel Nuclear Imaging Systems for Bioscience Applications

A Dissertation Presented

by

Tuoyu Cao

to

The Graduate School

in Partial Fulfillment of the

Requirements

for the Degree of

Doctor of Philosophy

in

Biomedical Engineering

Stony Brook University

December 2015

Stony Brook University

The Graduate School

Tuoyu Cao

We, the dissertation committee for the above candidate for the
Doctor of Philosophy degree, hereby recommend
acceptance of this dissertation.

Paul Vaska, PhD – Dissertation Adviser
Professor, Department of Biomedical Engineering, Stony Brook University

Terry Button, PhD - Chairperson of Defense
Associate Professor, Department of Radiology, Stony Brook University

David J. Schlyer, PhD
Professor, Department of Biomedical Engineering, Stony Brook University

Craig Woody, PhD
Senior Physicist, Brookhaven National Laboratory

This dissertation is accepted by the Graduate School

Charles Taber
Dean of the Graduate School

Abstract of the Dissertation

Development of Novel Nuclear Imaging Systems for Bioscience Applications

by

Tuoyu Cao

Doctor of Philosophy

in

Biomedical Engineering

Stony Brook University

2015

Biological systems are incredibly complex and their scientific study can be facilitated by the assessment of multiple independent parameters from the same location, ideally in way that provides quantitative and time-synchronized data, with high spatial sampling, and throughout a living subject. Our group has advanced this *in vivo*, quantitative, multimodal imaging approach by developing and combining various nuclear imaging modalities that provide complementary data to better understand the physiology of humans, animal models, and even plants.

Multi-modality imaging in clinical and pre-clinical settings has been shown to provide better diagnostic interpretation compared to stand-alone imaging systems. In recent years, combining PET and MRI together has opened a new area of imaging technology compared with well-established PET-CT because of the inherently different imaging contrast mechanism of MRI compared with CT. At Brookhaven National Laboratory, a PET system has been developed for the purpose of simultaneous PET-MRI whole rodent imaging in conjunction with a Varian large-bore 9.4T MRI system with a commercial Insight birdcage coil. The main aims of the dissertation include developing hardware and software for this new PET system, evaluating the system performance and investigating the system under scenarios of meaningful preclinical studies.

Positron Emission Tomography can also be used to study plant biology. However, since some important structures found on plants (e.g, leaves) are very thin, a large portion of the positrons emitted from PET isotopes escape before annihilation, leading to low efficiency and quantification inaccuracies. A gas tracking detector is developed here to measure escaping

positrons from PET radiotracer isotopes which has the ability to reconstruct three dimensional tracks that can be used to form an image of the emitting object. This device uses a triple GEM detector with a short drift region and an XY strip readout plane to measure a vector for positrons passing through a drift gap. By projecting each particle track back to the object surface, a 2-D image of the spatial distribution of the positrons that escaped from that surface can be reconstructed. We describe the basic principle of the GEM detector and present results on its performance using various types of phantoms and actual plant specimens. Monte Carlo simulations are also used to better understand the detector performance and compare to actual measurements.

Finally, I performed a simulation study of a new nuclear imaging method that can provide quantitative imaging data on elemental composition within the human body. Such information is currently measurable only via biopsy, and a non-invasive measure could have far-ranging benefits from nutrition to cancer diagnosis, especially if assessed in conjunction with other imaging modalities such as PET and MRI. The method involves inelastic neutron scattering and it shares many parallels to modern forms of PET, including the concepts of line-of-response and time-of-flight. My analysis shows that the approach is very promising, achieving quantitative measures of heavy elements with acceptable radiation dose to the patient.

Dedicated to my family

Table of Contents

List of Figures

List of Abbreviations

APD	Avalanche Photodiode
SiPM	Silicon Photomultiplier
CT	Computer Tomography
EM	Electromagnetic
MRI	Magnetic Resonance Imaging
PET	Positron Emission Tomography
RatCAP	Rat Conscious Animal PET
ASIC	Application Specific Integrated Circuit
LYSO	Lutetium Yttrium Oxyorthosilicate
FPGA	Field Programmable Gate Array
BNL	Brookhaven National Laboratory
TSPM	Timestamp and Signal Processing Module
TDC	Time to Digital Converter
FOV	Field of View
RF	Radio Frequency
DAC	Digital to Analog Converter
ADC	Analog to Digital Converter
DAQ	Data Acquisition
SFP	Small Form-Factor Pluggable
LOR	Line of Response
MLEM	Maximum Likelihood Expectation Maximization
FWHM	Full Width at Half Maximum
NECR	Nosie Equivalent Count Rate
FBP	Filtered Back Projection
SNR	Signal to Noise Ratio
^{18}F-FDG	Fluorine-18 Radiolabeled Fludeoxyglucose
GEM	Gas Electron Multiplier
SSS	Single Scatter Simulation

Acknowledgments

The projects in this dissertation are collaboration efforts from many brilliant, hard-working scientists and engineers from Brookhaven National Laboratory, Stony Brook University and University of Pennsylvania. It has been an honor for me to work with them and learn from them.

I would like to thank my advisor, Dr. Paul Vaska, who has always been patient, supportive and providing great guidance. I cannot overstate what I learned from Dr.Vaska, because not only I learned great amount of knowledge from him, more importantly, I learned methodologies to do research. Like a Chinese old saying says, "Give a man a fish and he will eat for a day; teach a man to fish he will eat for a lifetime". I am sure I will keep benefitting in my career and in my life.

I would like to thank Dr. Craig Woody, who is a great mentor, for guiding me through the GEM detector project, also for providing support and insightful suggestions on my academic and career path.

I also want to express my gratitude to Dr. David Schlyer, who introduced me to the lab and to the world of medical imaging. I cannot imagine how it would have been in the BNL group if without your support and your sense of humor.

I would also like to thank Dr. Terry Button for serving as the chairperson in my defense committee.

I am truly privileged to work with Dr.Martin Purschke and Jack Fried, who have built the framework of the software and hardware systems for the PET detector. I want to thank Sean Stoll, who provides great support on mechanical design and system integration. I also want to thank Bob Azmoun, without whom, it is impossible to build the GEM tracking detector.

I would like to thank all my lab mates, especially Dr. Michael Budassi, who has been working with me side by side in the past 5 years.

I would like to thank our many collaborators in University of Pennsylvania, Dr. Joel Karp, Dr. Stephen Pickup, Eric Blankemeyer and Matthew Werner for their help and support on developing and testing the PET/MRI system.

I would like to thank Department of Energy (under Prime Contract No. DE-AC02-98CH10886) and Baldwin Foundation for providing funding for the research projects.

Finally, I would like to thank my parents and my girlfriend Yamei, with love and gratitude. This thesis is dedicated to them.

Chapter 1: Overview

Nuclear imaging, or Molecular imaging is a branch of medical imaging that uses small amount of radioactive material to provide detailed pictures of what is happening inside the object at the molecular and cellular level. While other diagnostic imaging procedures, such as Computed Tomography (CT) and ultrasound, offer pictures of physical structure. Nuclear imaging allows people to see how a biological system is functional and to measure its chemical and biological processes. Different nuclear imaging techniques have been used in a wide variety of areas, such as clinical diagnostics, basic scientific research with small animals and even in plant biology studies.

Positron Emission Tomography (PET) is a major type of nuclear imaging technique that produces a three-dimensional image of functional processes in the object. Brookhaven National Laboratory (BNL) has been a pioneer in the development of PET. In 1961, James Robertson and his associates at BNL built the first single-plane PET ring scanner, nicknamed the "head-shrinker". In 1976, a BNL group under the direction of Al Wolf and Joanna Fowler developed 2-deoxy-2-(^{18}F)fluoro-D-glucose (FDG) [1], which is a glucose analog and still the most widely used PET tracer today. The development of FDG is a major factor in expanding the scope of PET imaging. And since 2001, a PET system, named Rat Conscious Animal PET (RatCAP) has been designed at BNL specifically to image the awake animals to avoid the use of anesthesia [2].

The detector technology originally designed for RatCAP are then extended for applications including a PET insert for 9.4T MRI[3, 4], a wrist scanner to non-invasively access input function[5], a MR compatible breast PET scanner[6] and a plant PET scanner for plant biology studies at BNL[7]. All these systems share the same detector technology[8]. This dissertation describes a new PET system based on the RatCAP block technology, which is designed as an insert for a large bore 9.4 T preclinical MRI system. Moreover, to address the positron escape problem during the PET imaging in plant applications, a gaseous detector has been developed for direct positron imaging, which will be described in detail in this dissertation.

Dissertation outline

Chapter 2 will give a brief overview of the PET principles, including PET physics and data acquisition, image reconstruction and correction techniques to achieve quantitative PET images. It also includes a review of PET/MR systems. Chapter 3 will discuss the system architecture of the PET-MRI insert as well as the data calibration and image reconstruction schemes. Chapter 4 contains performance evaluation of the system and some recent imaging results. Chapter 5 will discuss the GEM tracking detector for positron imaging in plant applications. And chapter 6 will discuss a Time-of-flight (TOF) neutron imaging system for detecting trace element concentration *in vivo*.

Chapter 2: Quantitative PET-MRI Imaging

2.1 Introduction of Positron Emission Tomography

Positron Emission Tomography (PET) is a nuclear medicine imaging technique which can produce a three-dimensional distribution map of the injected radioactive tracer. With biologically relevant molecules tagged with positron emitting radioactive isotopes, PET can assess functional processes inside the body, which is different and complementary to most other imaging modalities such as CT and MRI. The most commonly used radioactive tracers is ^{18}FDG (2- fluoro-2-deoxy-D-glucose), which has a similar biological pathway as glucose; thus a FDG based PET scan is a non-invasive way to measure glucose metabolism *in vivo* and is a very powerful tool for early stage cancer diagnosis and cancer staging.

The physics of this process is shown below. The radionuclides used in PET decay to their stable state through the emission of a positron with a neutrino. The positron has some amount of initial energy (the mean energy of positrons from ^{18}F is ~250 keV) and travels a small distance in the tissue before annihilates with an electron in the surrounding medium. Two back to back 511 keV energy gamma photons are created, and if they are both captured and fall into the time window of the PET detector, this annihilation event is recorded as a "prompt coincidence". The location of the annihilation is assumed to be along the straight line (also known as the line of response or LOR) connecting the two detector units capturing these two photons. With many annihilations events, mathematical algorithms can be used to reconstruct the 3D image of the source distribution.

Two important resolution degrading effects are involved in the positron annihilation process. The first is the positron range effect which is due to the fact that there is a small distance between the location of the radionuclide and the point of positron annihilation. The average distance could be ranging from 100 microns to more than 1 mm depending on the energy of the positron and the density of the tissue. This effect is usually negligible in clinical studies but might be important in some preclinical applications if sub-mm resolution is expected especially when isotopes with high energy positron (such as ^{15}O) are used. Furthermore, positrons close to the surface of the object may escape without annihilation which could be a major issue in plant studies, as described above. The second effect is called "noncollinearity" which describes the

fact that the angle between two gamma photons coming from the same annihilation event is not strictly 180 degrees. This comes from the fact that the positron and electron are not completely at rest when they annihilate. The angular uncertainty is approximately 4 mrad (0.23°). And its impact on image resolution increases with the dimension of the detector, thus it is less a problem in preclinical systems than in clinical settings.

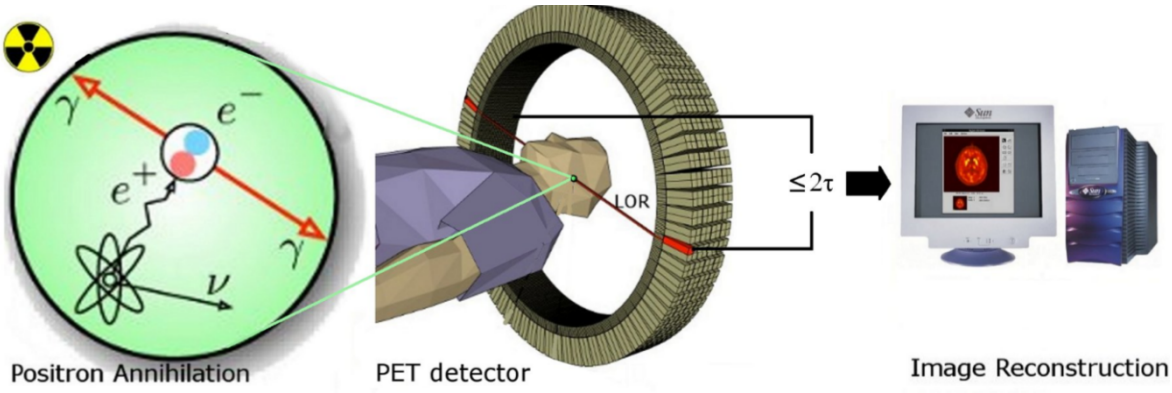

Figure.1 Schematics of PET imaging process (Picture made by Jens Maus, the author grants anyone the right to use this work for any purpose)

2.1.1 Types of coincidence events

There are three types of prompt coincidence events in the recorded raw data, including true coincidence, random coincidence and scattered coincidence, illustrated in the figure below. A true coincidence event is the ideal scenario, contains two unscattered photons originating from the same annihilation event. A random coincidence happens when two photons coming from different annihilation events fall into the time window and get recorded as a coincidence event. The rate of random events can be estimated by the formula:

$$r_{ij} = 2\tau s_i s_j \qquad (2.1)$$

Where r_{ij} is the rate of random events in the LOR between channel i and j, 2τ is the time window of the system and s represents the rate of single photon events. This formula shows that the random rate is linear with the width of the time window and roughly proportional to the square of the activity of the object.

A scattered event happens when at least one of the two photons undergoes Compton scattering. Photons lose energy during Compton scattering; thus a low level energy threshold can be used to filter out scattered events. However, due to the finite energy resolution of current PET systems, it is impossible to rule out scattered events solely based on an energy window. More details on scatter and random correction techniques are discussed below. Obviously only true coincidence events contain useful information of the positron location, while the other two would give misplaced line of response and would degrade the image resolution and contrast without proper corrections.

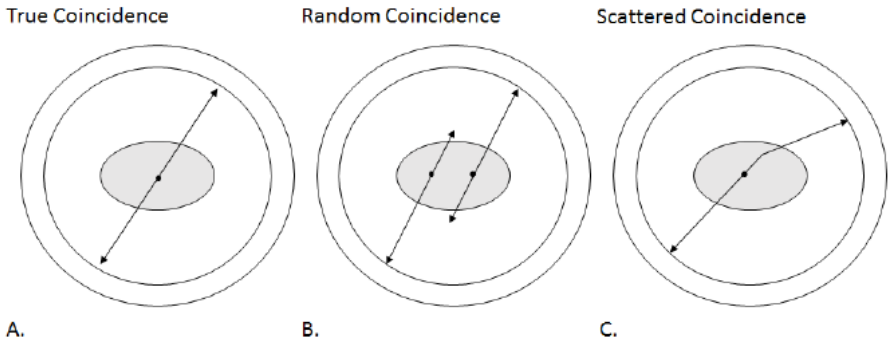

Figure.2 Types of coincidence events [9] (reuse with permission)

2.2 PET detector components

The function of the PET detector system is to capture gamma photons from positron-electron annihilation and determine the time and energy information of these gamma photons. The timing information is used to differentiate true events and random events. As described above, two gamma photons coming from the same annihilation event would have very similar arrival time at the detector, thus a time window is used to capture coincidences. The width of the time window usually depends on the timing resolution of the detector. PET systems with better timing resolution can use a narrower window. And with a narrower window, less random events would be recorded. Furthermore, if a detector has very high time resolution which is even smaller than the photon travelling time from the object to the detector, a technique called Time-of-Flight (TOF) can be used to improve the performance of the system [10]. The energy information is used to filter out part of the scattered events and other noise.

It is obvious that a good detector would require a strong stopping power to the 511-keV photons and provide high timing and energy resolution. There are three types of gamma photon detectors used in PET. One type is proportional gas chamber based [11] and another is solid state detector based such like Cadmium zinc telluride (CZT) which has been proposed by our group [12]. The major limitation of gas chamber is the low stopping power and poor energy resolution. And even though CZT based detectors can provide very good energy resolution, the stopping power is still relatively low and its timing resolution is poor which limits its application in PET. The dominant detector type is still scintillator based, combined with a photodetector for low energy optical photons, such as a photomultiplier tube (PMT) or an avalanche photodiode (APD).

The scintillator is usually very dense so it can stop the gamma photon through Compton scatter and photoelectric effect. Electrons in the scintillator can get excited to a higher energy level and return to the ground state during which scintillation photons are released. Scintillators used in PET applications usually create photons around the visible light range. Different scintillator materials have been studied in the past, such as sodium iodide (NaI), Bismuth Germanate (BGO), Lutetium Oxyorthosilicate (LSO), Gadolinium Oxyorthosilicate (GSO) and Barium Fluoride (BaF_2). Different scintillators have different characteristics such as stopping power, light output, output wavelength, decay constant etc. The most popular scintillator material is LSO, given its good and balanced stopping power (Effective Z:65.5), light output (29 photons/keV) and decay constant (40 ns). Other material types may have better performance in a few categories but often much worse performance in other categories. For example, BaF_2 has a much faster timing with 0.6 ns decay constant, but its stopping power and light output are low.

With LSO as the scintillator, one 511 keV gamma photon creates ~14000photons with 420 nm wavelength. The photons are coupled to photodetectors through light guide with either one-by-one coupling or light sharing. The traditional photodetector in PET applications is the PMT, which is usually coupled to scintillator arrays and the crystals are decoded through Anger logic since there are more crystals than PMTs. With semiconductor devices such as APDs and Silicon Photomultipliers (SiPM) one-to-one coupling becomes possible due to the highly flexible physical dimension of silicon devices.

2.3 PET data structure

The raw PET data is usually a series of coincidence events in time order, containing spatial, energy and timing information based on the type of detector system. Then the data is usually reorganized into a structure called a "sinogram". As shown in the figure below, with a cylindrical ring shape PET detector, if we denote z axis parallel to the axial direction, then x and y axis define the transverse plane. Early versions of PET detectors usually work in a 2D mode, meaning only accepting LORs within each transverse plane. So the sinogram is described by s, Φ and z, where s denotes the perpendicular distance between the LOR and the center of each ring, Φ denotes the projection angle and z denotes the position on the axial direction. Modern PET scanners usually operate in a 3D mode, meaning accepting all possible LORs formed with in the detector. So another dimension θ is added denoting the angle between the LOR and the x-y plane, which makes the sinogram a 4D data structure.

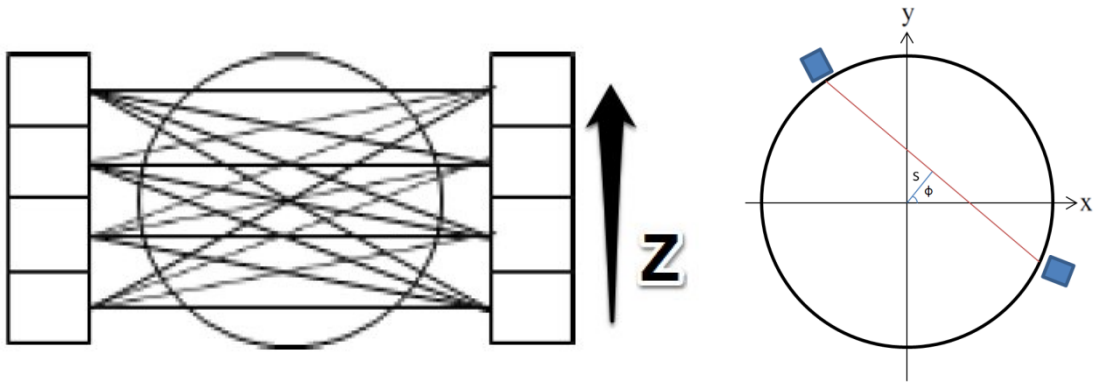

Figure.3 (left) Fully 3D PET acquisition; (right) LOR define in one plane

Most real PET detectors are block-based with many small crystals like in figure 1. So the raw sinogram has non-uniform sampling but contains LORs connecting real crystals. For a ring detector with m rings and n crystals within each ring, the sinogram has m^2 slices and within each slice there are n projection angles. Since ring PET systems are typically under-sampled in the s direction and adequately sampled in the Φ direction, the projection data are usually rearranged by "interleaving" adjacent angular views as shown in Figure.9 to form a sinogram with half the angular sampling rate and twice the linear sampling rate. So the size of each slice sinogram becomes $n(n-1)/2$.

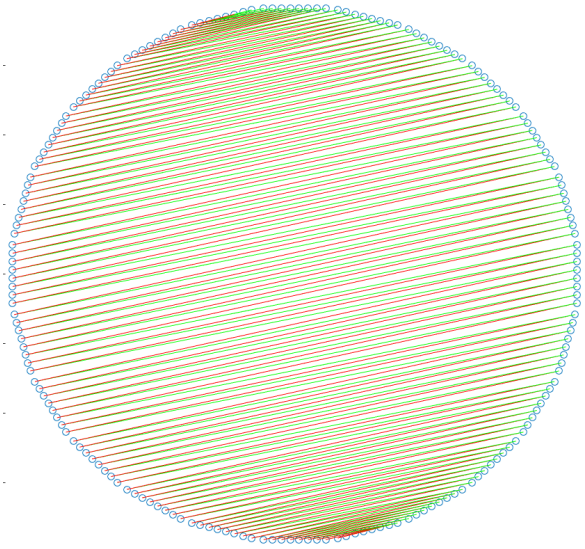

Figure.4 Example of sinogram interleaving (geometry of BNL-PENN PET insert), LORs marked with red and LORs marked with green are interleaved into one projection angle

Based on Shannon's theory, the maximum recoverable spatial frequency is one half of the detector pitch, and can be obtained with uncompressed sinogram. However, PET systems are usually limited by low statistics thus sinogram is sometimes compressed in either axial direction (span) or transaxial direction (meshing) or both.

2.4 PET image reconstruction

Image reconstruction algorithms are divided into two main categories - analytical methods and iterative methods. The analytical methods used in PET have very similar format as those used in X-ray Computed Tomography (CT). It is usually done by the filtered back projection (FBP) algorithm. It is based on a few assumptions as shown below:

(1) Acquired data is noise free or has very low noise

(2) Data is the radon transform of the activity distribution, meaning the count of each LOR is proportional to the line integral of activity along this LOR

(3) Adequate linear and angular sampling

However, all these simplifying assumptions are violated in practice, which makes analytical methods not ideal for PET image reconstruction. PET data usually is considered to contain

Poisson noise and a practical PET study is often limited by the noise. The events in each LOR also cannot be estimated by a simple line integral model.

It is possible to more accurately model the physics of PET data acquisition, but it is difficult to invert these models with analytical methods, which naturally leads to the development of iterative methods. A more general linear model than radon transform allows better description of the blurring and attenuation mechanisms in the imaging process, and with a proper statistical model it can also deal with noisy PET data better. Although iterative methods come with the price of a bigger computational burden so it is significantly slower than analytical methods, with fast growing computing powers and parallel computing techniques, iterative algorithms are the main stream of PET image reconstruction currently.

There are a few basic components in iterative methods:

(1)A mathematical model to describe the image space

(2)A system response model to describe the physics of data acquisition

(3) A statistical model for the noise in the data

(4)A statistical estimation criterion or the objective function

(5)An algorithm to extract the parameters so the objective function is maximized

2.4.1. Image representation

In the computer, the continuous value of activity distribution is often discretized as a weighted combination of translation invariant basis functions. The most popular basis function is the continuous and non-overlapping rectangular basis function, also known as voxels. Another popular basis function is the Kaiser-Bessel function [13, 14]. With properly selected parameters, this spherically symmetric basis function has a finite response in spatial domain and practically band limited in frequency domain, in contrast to voxels which has high frequency component. Reconstruction with these “blob” basis functions has been proved to have lower noise level without losing resolution. However, because of the overlapping nature of blobs, the computational demand tends to be larger than voxel based reconstruction. Other types of basis functions have been proposed for the purpose of fast reconstruction, such as polar voxels [15]

which is developed to take advantage of the symmetries in cylindrical detectors. This results in a block-circulant system response matrix so less storage and computational power are required.

2.4.2. System response matrix

A linear model is often used to describe the physics of PET system

$$g = Hf \qquad (2.2)$$

In this equation, **g** denotes the projection space, **f** denotes the image space and **H** is the system response matrix in which each element h_{ij} represents the possibility that an emission from image voxel j is detected by LOR i. Any linear physical effect can be modeled into this function and the accuracy of the system matrix determines the accuracy of the reconstruction results. Ideally the system matrix should model the complete process from positron annihilation to registration of coincidence events to each LORs and take into consideration all the physics effects including positron range, noncollinearity, photon scatter, photon attenuation, detector solid angle, inter-crystal scatter, detector dead time, response of readout electronics, etc. An intuitive way of building the system matrix is to measure the system response with a point source at all locations within the FOV, or to simulated multiple positions with a point source in a Monte Carlo simulation package. However, this methods is not practical for clinical systems and most preclinical systems, because (1) the measuring process will be very time consuming due to the fact that high counts are required to ensure low statistical noise, and (2) the system matrix will be so big that it requires gigantic storage space and very slow to use since it won't fit into computer memory in most cases.

Due to these limitations, assumptions and approximations are usually used to form the system matrix. Since the system matrix is usually very sparse, it can be factorized into a few components, first proposed by Qi [16]. Based on this idea, a system matrix can be written in the format below:

$$H = H_{\det e.sens} H_{\det .blur} H_{attn} H_{geom} H_{positron} \qquad (2.3)$$

In which $\boldsymbol{H} \in \mathbb{R}^{\boldsymbol{I}\times\boldsymbol{J}}$ is the overall system response matrix, I is the number of LORs and J is the number image voxels. $\boldsymbol{H_{positron}} \in \mathbb{R}^{\boldsymbol{J}\times\boldsymbol{J}}$ represents the blurring effects in image space, such

as the positron range effect. $\boldsymbol{H_{det.blur}} \in \mathbb{R}^{\boldsymbol{I}\times\boldsymbol{I}}$ models the blurring effects in sinogram space, such as inter-crystal scattering, crystal penetration and crystal misidentification. $\boldsymbol{H_{dete.sens}} \in \mathbb{R}^{\boldsymbol{I}\times\boldsymbol{I}}$ and $\boldsymbol{H_{attn}} \in \mathbb{R}^{\boldsymbol{I}\times\boldsymbol{I}}$ are both diagonal matrix and account for attenuation factors and normalization factors.

Different levels of approximations based on this model have been implemented and tested with various types of PET detectors. The most basic component in these factors is H_{geom}, the geometric factor. It can be pre-calculated and stored in the memory or calculated on-the-fly. Note that there are also several symmetries can be taken advantage of when calculating these factors, even for rectangular voxels. The simplest way of acquiring this matrix is through single ray-tracing, which essentially calculates the LOR length of interception through each voxel. This is usually done with Siddon's algorithm[17] or its expedited version [18]. However, the length of interception is not a perfect description of the solid angle effect in photon detection in PET (the idea of length of interception comes from CT image reconstruction). Thus more accurate algorithms with bigger computational burden have been developed such as using tube of response instead of line of response [19], calculating the solid angle and storing the matrix before reconstruction [16], and multi-ray tracing based method [20]. More modern implantations use GPU to compute the matrix in parallel so a significant increase in speed can be achieved [21-24]. Trade off exists between accuracy and time/space complexities and since part of the geometrical effect can be accounted in sinogram or image space blur, most systems, especially full-body systems, use simple on-the-fly calculated geometrical models to achieve faster reconstruction speed.

Ignoring the two diagonal matrices of normalization and attenuation, the system matrix is usually further simplified to either $H = H_{\det.blur} H_{geom}$ or $H = H_{geom} H_{positron}$.The sinogram space blurring is usually adequate when the positron range effect is not very strong since it can model the blurring effect in sinogram space as well as the shift-invariant positron range effect. Image space blurring can model the shift-variant positron range effect but the accuracy of modeling the detector blurring effect depends on the overlap of the range spaces of matrices $H_{\det.blur}$ and $H_{positron}$ [25]. The blurring matrix can be either simulated with Monte Carlo software or measured with a real source[26]. Note that for list mode reconstruction, only image space blurring model

can be used since there is no sinogram during reconstruction process. Drawbacks of using resolution models includes edge artifact and bigger noise; thus it should be used with caution especially when partial volume effect is not the dominating problem. A thorough review of this topic can be found in Rahmim's article [27].

2.4.3. Noise modeling and objective function

Photon emissions are known to obey the Poisson distribution and so is the photon detecting process, provided that detector dead time can be neglected and no corrections have been applied to the data.

The maximum-likelihood (ML) criterion[28] is a standard statistical-estimation criterion often used in PET image reconstruction. The ML criterion can be stated as: Choose the reconstructed image f so the measured data would have the largest probability $p(g;f)$, or written symbolically as:

$$f = \arg\max_{f} p(g;f) \quad (2.4)$$

The ML estimators have some desirable properties: (1) ML estimators are asymptotically unbiased, meaning that the estimate become unbiased when the number of observations becomes large, and (2) the ML estimators are asymptotically efficient, meaning that they yield the minimum variance among unbiased estimators.

2.4.4. EM Algorithm

The EM algorithm, first proposed by Dempster et al. in 1977 [29], and proved of convergence in 1983 by Wu[30], is a general algorithm to solve ML estimation problems with incomplete data, which means there is no explicit way to write out the object function. The specific iterative formula for imaging reconstruction was proposed by Lange and Carson[31]. The basic idea of EM algorithm is to construct a "complete dataset" so the ML estimator can be easily written, and then repeat two alternating steps until convergence. These steps are called the expectation step (E-step) and the maximization step (M-step). Within E-step, the current estimated parameters are used to calculate the complete data, while during M-step, the complete data is fixed and a new set of parameters are chosen to maximize the ML estimator.

Mathematically the EM algorithm can be considered as a weighted version of gradient descent, meaning the update step is weighted by the current value. So convergence rate of MLEM is faster for voxels with higher initial values. More detail on the connection between EM algorithm and gradient descent can be found in Xu's paper [32]. Under the scenario of imaging reconstruction of PET, the observed data, which is incomplete, is line integrals with different projection angles, denoted by **g**, while the complete data is usually chosen as **s**, where s_{ij} means the number of photon emitted by voxel j detected by LOR i. The complete data **s** can be connected to the observed projection data **g** and the image **f** as follows:

$$g_i = \sum_m s_{im} \quad (2.5)$$

$$E\left[s_{im}\right] = h_{im} f_m \quad (2.6)$$

h_{im} is one element of the system matrix **H**, as defined in equation 2.2. With the knowledge of complete data **s**, and assume s_{im} are independent Poisson-distributed random variables, the object function can be easily written as:

$$p(s;f) = \prod_i \prod_m \frac{E\left[s_{im}\right]^{s_{im}} e^{-E\left[s_{im}\right]}}{s_{im}!} \quad (2.7)$$

And the log-likelihood is (consider equation 2.6):

$$\ln p(s;f) = \sum_i \sum_m \left[s_{im} \ln(h_{im} f_m) - h_{im} f_m - \ln(s_{im}!) \right] \quad (2.8)$$

In E-step the conditional expectation of s_{im} can be calculated as follow:

$$E(S_{im} \mid g, f^{(n)}) = \frac{h_{im} f_m^{(n)}}{\sum_k h_{ik} f_k^{(n)}} g_i \quad (2.9)$$

The first portion of the right term simply calculates the ratio between activity within voxel m and all voxels along projection i. With this conditional expectation of s_{im}, the M-step is trivial now. Simply take partial derivative of f and set it to zero, we can get the well-known ML-EM iteration for PET reconstruction:

$$f_j^{(n+1)} = \frac{f_j^{(n)}}{\sum_i h_{ij}} \sum_i h_{ij} \frac{g_i}{\sum_k h_{ik} f_k^{(n)}} \quad (2.10)$$

The term $\sum_k h_{ik} f_k^{(n)}$ is usually called "forward projection," which is a transformation from image space to sinogram space. While multiply the transpose of the system matrix is referred as "backward projection", which updates the image. The term $\sum_i h_{ij}$ is referred as "sensitivity image". If replace g_i with 1, we get the ML-EM formula for list-mode reconstruction. Note that the system response model h_{ik} includes all physical effects in sector 2. And since components of system matrix such as attenuation and normalization are diagonal matrixes, they are only included in the sensitivity image because they cancel out during forward and backward projections.

2.4.5. Variations on ML-EM

The ML-EM algorithm has two major drawbacks, (1) it is much slower than FBP, and (2) it can yield very noisy reconstructed images when close to convergence. Thus there are variations of ML-EM algorithms to solve these problems. A simple modification of ML-EM, called OS-EM (Ordered subset EM) [33]is widely used to speed up the reconstruction by only using a subset of data to update the image during one iteration. And it appears to have most of the desirable properties of ML-EM. Note that OS-EM has no proof of convergence even though it generally gives good results nearly identical to ML-EM in tomography reconstruction.

To solve the noise problem of ML-EM, the most widely used method is to simply stop the iteration early before convergence. Other approaches such as applying a filter or Maximum A Posteriori (MAP) algorithm have also been used, which offers more flexible ways for different applications.

2.5 Quantitative Techniques in PET

PET is considered as a quantitative imaging tool, which means with a single calibration factor, the voxel values of the reconstructed images represents the true concentration of the tracer. However, the quantitative accuracy of PET is strongly based on exact corrections for

multiple physical effects during data acquisition, including random correction, attenuation correction, normalization, scatter correction and dead time correction.

2.5.1 Random correction

As illustrated in section 2.1, there are three types of coincidence events and only the true coincidence contains useful information. The random coincidence, which occurs when two photons fall into the same time window but originate from different positron annihilation events, can blur the image and induce bias on quantification. The fraction of random events depends on the time window and the activity of the radionuclide. The most commonly used random correction technique is delayed window method. This method utilizes another window the same length of the regular coincidence window but being delayed for a time much longer than the window width, so all coincidence falling into this delayed window would be random coincidence and can be a good estimate of random coincidence in the regular time window. This method is more accurate than singles rate based method because the delayed window has exactly same dead-time environment and the accuracy of random estimate is not affected by time-variant activity distribution. The major drawback of this method is that the random estimate is much noisier than singles based method. Random variance reduction methods has been proposed to solve this problem [34, 35].

2.5.2 Attenuation Correction

The detection of coincidence events requires both gamma photons reach the detector and the transportation of gammas follows Beer-Lambert law, so the possibility of both gammas reaching the detector can be described as:

$$P = P_1 P_2 = e^{-\int_A^B \mu dl} e^{-\int_A^C \mu dl} = e^{-\int_B^C \mu dl} \qquad (2.11)$$

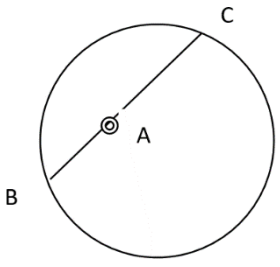

Where A is the annihilation point, B and C are detector point. So the attenuation effect of each LOR can be calculated by integrating the linear attenuation coefficient along the LOR path, and independent of the location of the annihilation point, which is a very appealing feature of PET compared with SPECT systems. The remaining question is how to acquire the attenuation map.

Historically, the attenuation map is acquired by using “transmission scan”. A rotating source is used to acquire data with and without the object inside the FOV and the difference between them shows the attenuation effect. Both coincidence mode and singles mode with collimated source[36] can be used in transmission scan. Later with the combined PET-CT system, people explored that CT image can provide the attenuation map[37]. Since the energy of X-ray photons (70-140 keV) is different than PET photons (511 keV), a bi-linear transform is used to scale the attenuation coefficients. Compared with transmission scan, CT based attenuation correction is much faster with better statistics.

As described in the introduction section, MRI based PET attenuation correction is a major problem for the hybrid PET/MR system, since MRI cannot provide direct information about electron density. Different approaches have been proposed in the past few years, and can be divided into 4 categories: template-based, atlas-based, direct segmentation and method based on special bone representing sequence.

Both template and atlas methods relies on mapping the subject to reference data sets so they are not robust enough to deal with non-rigid organs, organ motion or abnormal subjects. The most popular attenuation correction method used today is still direct segmentation [38-40], because it does not require reference data and it is fast in terms of both MR sequence and computation time. Two point Dixon sequences [41] are usually used to provide separate images for water and fat and further segmentations of MR images into lungs, adipose tissue, soft tissue and background. The major limitation of this sequence is that bone cannot be separated with background but bone usually has the highest attenuation coefficient, which could cause strong image artifact especially at regions close to bone. To solve this issue, MR attenuation based on Ultrashort echo time (UTE) or Zero echo time (ZTE) sequences were developed to visualize anatomical regions with very short relaxation time[42]. In clinical PET-MRI systems, UTE based attenuation correction is becoming a standard in brain studies, while it is still not widely used in whole body scans due to the extra MRI time required.

2.5.3 Scatter correction

Compton scatter is the dominating effect when 511 keV gammas interact with tissue. The relation between scattering angle and the energy loss of the incident gamma can be described by:

$$E_{after\_scatter} = \frac{E_{before\_scatter}}{1 + \frac{E_{before\_scatter}}{m_e c^2}(1 - \cos\Omega)} \quad (2.12)$$

Where $m_e c^2$ is the rest energy of the electron and Ω is the scattering angle. Because of the limited energy resolution (10%-20%) of the current PET detectors, it is impossible to reject these scattered gammas by simply setting an energy threshold. In a typical clinical study, scatter events can be as high as 50% of prompts or even higher for large patients. While the scatter fraction is much smaller in preclinical studies, it can still be about 10%-20% of prompts [43]. Thus accurate scatter correction is very important to achieve high image quality and quantification accuracy. There are a few different approaches to apply scatter correction, including fitting a simple Gaussian function, multiple energy window based, convolution based, single scatter simulation (SSS) [44, 45] and Monte Carlo based methods [46-49]. Monte Carlo simulation has the potential to be the most accurate method since it can include all physics effect but there are trade-offs between accuracy and speed and it is still not practical in clinical settings. Even if it will be a promising method with better hardware such as GPU and implementation optimization, the most prevalent method nowadays is still single scatter simulation (SSS) which is fast enough and gives very accurate results for most applications.

SSS is based on the fact that the differential cross section of Compton Scattering is accurately described by the Klein-Nishina formula:

$$\frac{d\sigma}{d\Omega} = \alpha^2 \gamma_c^2 P(E_\gamma, \theta)^2 [P(E_\gamma, \theta) + P(E_\gamma, \theta)^{-1} - 1 + \cos^2(\theta)] / 2 \quad (2.13)$$

Where $\frac{d\sigma}{d\Omega}$ is the differential cross section, α is the fine structure constant (~1/137.04), θ is the scattering angle; γ_c is the reduced Compton wavelength of the electron (~0.38616 pm); and $P(E_\gamma, \theta)$ is the ratio of photon energy after and before the collision, which can be calculated from (2.12).

The scatter events in each LOR can be estimated with:

$$P_{scat}^{AB} = \int_{V_s} dV_s \frac{\mu d\sigma}{\sigma d\Omega}(I^A + I^B) \qquad (2.14)$$

Where

$$I^A = \varepsilon_{AS}\varepsilon'_{BS} e^{-(\int_S^A \mu ds + \int_S^B \mu' ds)} \int_S^A \lambda ds \,, I^B = \varepsilon_{BS}\varepsilon'_{AS} e^{-(\int_S^A \mu' ds + \int_S^B \mu ds)} \int_S^A \lambda ds \qquad (2.15)$$

In these equations, λ is the emitter intensity, μ is the attenuation coefficient (μ' is the attenuation coefficient for the photon after scatter), V_s is the whole scatter volume, ε is the detecting efficiency, including the solid angle effect, energy threshold and energy resolution. σ is the total Compton Scatter cross section while $\frac{d\sigma}{d\Omega}$ is the differential cross section which can be obtained from the Klein-Nishina formula.

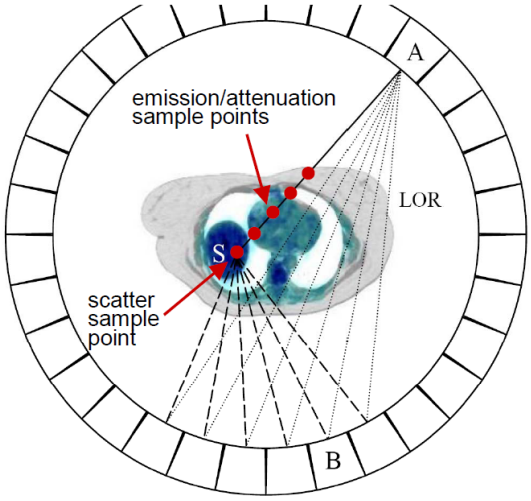

Figure.5 Single Scatter Simulation model[50] (©2005 IEEE)

Since SSS requires the information of emission distribution which is not available, so it is usually done in an iterative fashion, meaning updating the image and scatter estimation alternatively. And the result of SSS is scaled with a tail fitting technique, meaning fitting the scatter distribution to the tail region of the random corrected prompt data, where the tail region is usually defined by the attenuation map. Moreover, since the scatter distribution usually only contains low frequency components, down-sampled sinogram and image are usually used to

speed up the process. One major drawback of SSS is that it only includes scatter events which contain Compton scatter once and so multiple scatter is not explicitly modeled. A few approaches have been used to improve the accuracy of SSS. The most basic one just assumes multiple scattering has a flat distribution so it can be modeled with a constant[51], which is accurate enough for most cases as long as the emission distribution only contains low frequency components. More advanced methods estimate the multiple scattering distribution by convolving the single scatter distribution with a Gaussian kernel [45, 52], with the underlying intuition that the multiple scatter distribution is wider than the single scatter distribution.

2.5.4 Normalization

The normalization process aims to compensate any detector efficiency effects not in the system matrix. So normalization factors need to match the system matrix type. The normalization factors for the system can be estimated under ML framework with known activity distribution[53], which gives a good insight of the correlation between system model and normalization factors.

In general, there are two major ways of doing normalization correction. A straightforward way, called direct normalization, is usually used with small scale detector systems. With this method, a uniform phantom with activity filling the whole FOV is acquired and the data is binned into a sinogram. Then a model sinogram is generated by forward projecting the same phantom in the image space using the same projector in image reconstruction. Then the bin by bin ratio of these two sinograms gives the normalization factors for each LOR. The major drawback of this method is that it requires a scan with very high statistics since it's done in the LOR space. And this method fails to consider the fact that scatter events technically should have different normalization factors than true events. It also does not include count rate dependent factors.

To address these problems, a component based method [54, 55] was developed and its variations are used in most clinical systems right now due to the speed and flexibility. The basic idea is to break down normalization into a few factors so it can be done in the crystal space rather than the LOR space thus it would require much less statistics. And it is more flexible to

account for more physical effects. A general component based normalization modal can be expressed as:

$$NC_{uivj} = \varepsilon_{ui}\varepsilon_{vj}b_u b_v c_{ui \bmod D} c_{vj \bmod D} d_{uvrk} f_{uv} g_{uvr} h_{uivj} \qquad (2.16)$$

NC_{uivj} is the normalization factor for LOR connecting crystal i in ring u and crystal j in ring v. ε_{ui} is the "intrinsic crystal efficiencies" which mostly related to the gain of the photo detector and the efficiency of the scintillation crystal. b_u and $c_{ui \bmod D}$ are transaxial and axial component of the block profile. These two factors can be combined with crystal efficiencies but they can be used separately to account for count rate dependent factors (dead time correction). d_{uvrk}, f_{uv}, g_{uvr} are crystal interference factors, axial geometric factors and radial geometric factors accordingly. They are fixed factors with certain detector system and they can be fully or partially incorporated into the system matrix. There are also multiple folds of symmetries in these factors so they can be further compressed. h_{uivj} is the time-window alignment factor, which can be ignored if all detector channels are well synchronized or t0 effect is well compensated.

Most PET systems utilize a simple version of this model since some factors in this model can be combined. With this method, only the crystal efficiency factor needs to be calibrated regularly since the gain of photon detectors may shift over time. And the rest factors can be just calibrated once and kept fixed afterwards.

2.5.5 Apply calibration factors

These calibration factors can be grouped into two types, multiplicative factors including normalization and attenuation, and additive factors including scatter and random events. In MLEM reconstruction, to maintain the Poisson statistics of the raw data, all the correction factors cannot be applied to the raw data directly. A MLEM formula with all the correction terms would be:

$$f_j^{(n+1)} = \frac{f_j^{(n)}}{\sum_i h_{ij} h_{norm} h_{attn}} \sum_i h_{ij} h_{norm} h_{attn} \frac{g_i}{\sum_k h_{ik} h_{norm} h_{attn} f_k^{(n)} + scatter + randoms} \qquad (2.17)$$

2.6 Basic Principles of Magnetic Resonance Imaging (MRI)

This section does not intend to give a comprehensive introduction on MRI physics, but rather a quick review on MRI from the PET-MRI perspective. A detailed description of MRI can be found in any MRI textbook, such as [56].

2.6.1 MRI physics

All imaging modalities share some basic common philosophies. To acquire information from an object, e.g. the body of humans or animals, the imaging system needs to provide an input signal and then detect the output signal from the object. Most imaging system use one type of electromagnetic(EM) wave as the information carrier (ultrasound systems being an exception). The figure below shows the spectrum of EM wave.

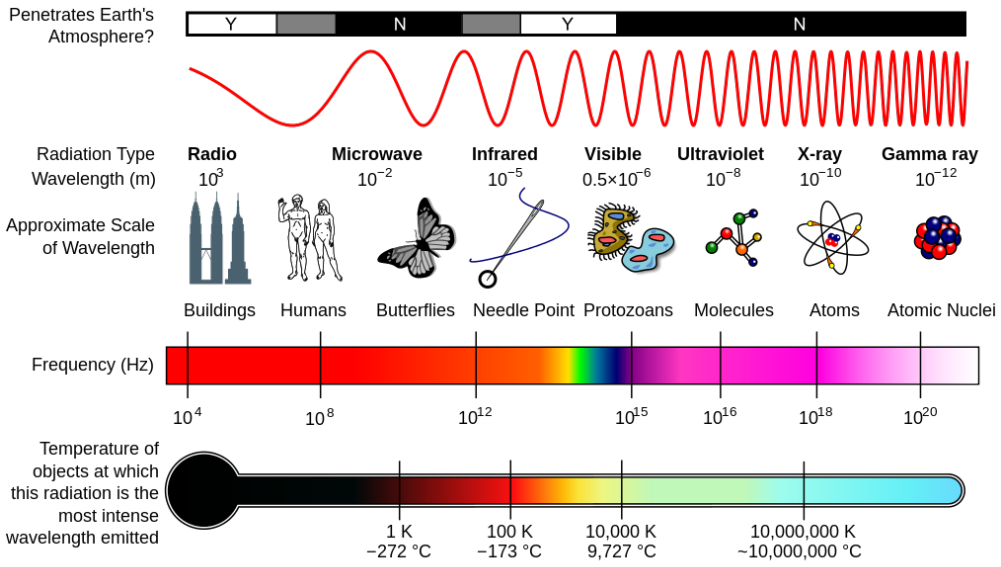

Figure. 6 A diagram of the electromagnetic spectrum, showing various properties across the range of frequencies and wavelengths (figure made by NASA, free to reuse)

Different imaging systems utilize different regions in this spectrum. Optical imaging such as Microscopy takes the region between Infrared to Ultraviolet. X ray, CT, SPECT, PET use the region of X-ray to Gamma ray. And MRI is generally in the region of Microwave with frequency ranging from 10 MHz for low field systems to more than 500 MHz for ultra-high field systems. Since EM wave with different frequency has different mechanism of interacting with the object, they also provide different contrast information. The complexity of MRI system is mainly due to the fact that the contrast mechanism is not as straightforward as other modalities.

The source of signal in human body is usually Hydrogen nuclei (proton), which are in abundance in the form of water and fat. When a Hydrogen nucleus is placed in an external magnetic field (often called B_0 field in MRI), it "precesses" around the applied field with a frequency proportional to the external field strength (This is only an analogy in classical mechanics, while quantum mechanics gives the comprehensive explanation). The relationship of the precession frequency and the B0 field is given by the Larmor equation: $\boldsymbol{\omega = \gamma B_0}$, Where ω is the angular precession frequency (Larmor frequency) of the proton in rad/s, B_0 is the field strength and γ is a constant known as the gyromagnetic ratio with the value of $\boldsymbol{2.7\times10^8 rad \cdot s^{-1} \cdot T^{-1}}$for Hydrogen nuclei in fat or water. So the Larmor frequency for a 9.4T system is 400 MHz. Since there are many nuclei in the object, the average effect is a net polarization that is parallel to the external field with no transverse magnetization (perpendicular to the main field) because the precession of the protons is not in phase. The net magnetization M_0 can be expressed as $\boldsymbol{M_0 = \rho\gamma^2\hbar^2 B_0/4k_B T}$, where ρ is the proton density, $\hbar$is the Planck constant, k_B is the Boltzmann constant and T is temperature in Kelvin. This formula indicates that the signal of MRI is proportional to the main field strength, which is the major reason for using high field MRI systems. Another major advantage of using high field is better resolution in MR spectroscopy.

When a Radio Frequency (RF) pulse (also referred as B_1 field in MRI) is transmitted into the object perpendicular to the external magnetic field B_0 at Larmor frequency, it excites the protons away from their stable state. The macroscopic phenomenon is that both the longitudinal and transverse magnetization change. For example, in the case of 90 degree RF pulse, the longitudinal magnetization becomes 0 after excitation while the transverse magnetization becomes the maximum. After this RF pulse, the protons return back to their stable state and during this process they emit weak EM wave which is the source of the signal in MRI. The strength of the signal is proportional to the magnitude of the transverse magnetization. The recovery of the longitudinal magnetization is called "Spin-lattice relaxation" while the decay of the transverse magnetization is called "Spin-spin relaxation". Each relaxation process follows an exponential curve with time constant of T1 and T2 respectively. And the difference of T1 and T2 for different tissue types is the major contrast mechanism of MRI. By choosing different

imaging parameters, different MRI image contrast can be obtained. A typical Spin Echo sequence is shown in the figure below.

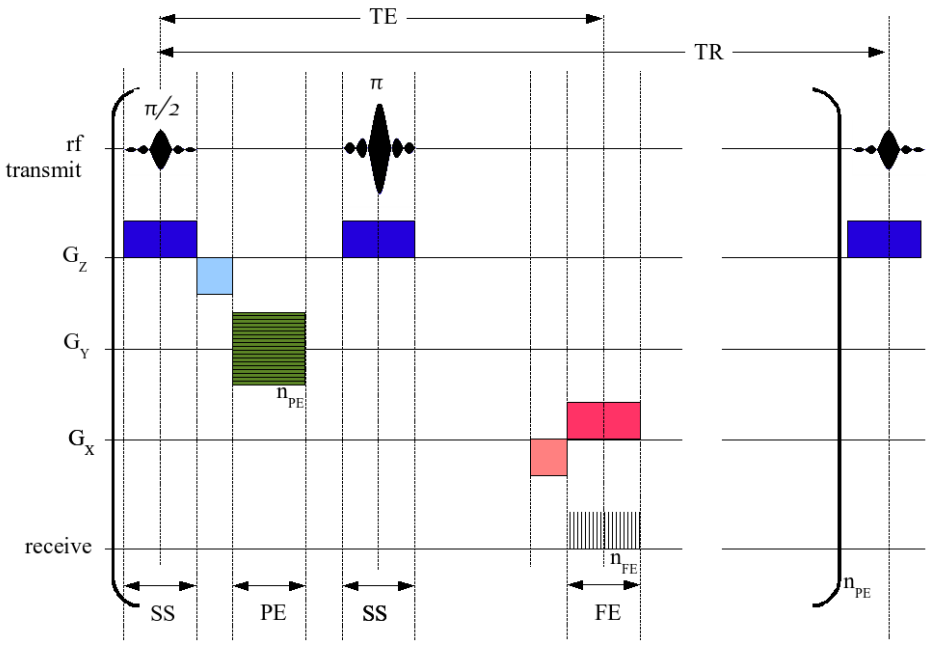

Figure.7 MRI Spin Echo pulse sequence (From Wikipedia, free to reuse)

2.6.2 MRI Hardware

There are three major components in a modern MRI system, a magnet, a gradient system and a RF system. The superconducting magnet is creating a strong B_0 field. The RF system is used to excite the object and then receive the EM wave from the object. And the gradient system is for spatial encoding.

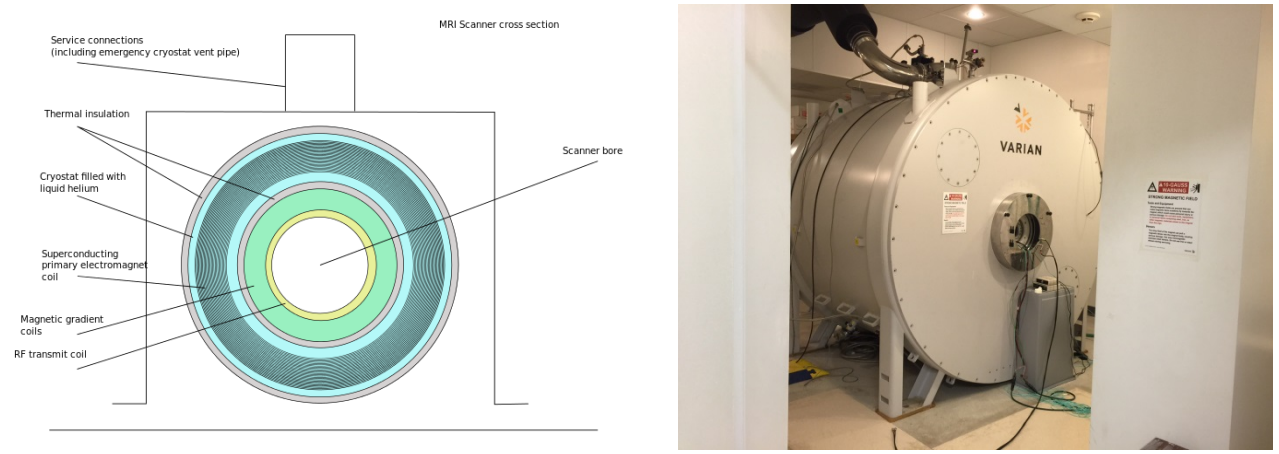

Figure.8 (left) Schematic of construction of a cylindrical superconducting MR scanner (image obtained from Wikipedia, free to reuse); (right) Varian 9.4T MRI in University of Pennsylvania

2.6.2.1 The magnet

Most modern MRI systems, especially high field system (B_0>1T), use superconducting coils to create the B_0 field. A cooling system with liquid helium is required for these magnets to maintain zero resistance on the wires. The most important consideration of choosing these high field MRI systems is that the image Signal to Noise Ratio (SNR) is proportional to the field strength. Another benefit of using high field MRI systems is better resolution for MR spectroscopy. However, high field systems also have greater challenges with field homogeneity.

2.6.2.2 The gradient system

Gradient systems are designed to create linear variations on three perpendicular directions upon the main field so that the MRI system can create 3D images. The magnitude of gradient field is usually on the order of 10mT/m, which is much lower compared to the B0 field. However, fast changing gradient sequences are necessary for many imaging applications - thus the gradient system requires a very high slew rate, in the range of 100-200 T/m/s for high field systems.

2.6.2.3 The RF system

The function of the RF system is to transmit RF excitation pulse and receive the EM signal from the tissue. So the system contains a transmitter and receiver. Preclinical systems usually use the combined transceiver coil which can both transmit and receive.

2.7 Simultaneous PET/MRI system

2.7.1 Motivation

PET is a nuclear medicine imaging technique that produces a three-dimensional map of functional processes in the body. This functional capability is different from and also a complement to other structural imaging modalities that mostly provide anatomical information such as Computed Tomography (CT) and Magnetic Resonance Imaging (MRI). Thus combing two modalities together could utilize the strengths of both, which are high sensitivity functional information and high resolution anatomical information. The combination of PET and CT scanners has been proved to be very successful in the past 15 years and nowadays almost all clinical PET scanners are shipped as PET-CT scanners.

As an alternative to CT, MRI provides better soft-tissue contrast without additional radiation dose. MRI also has a large variety of tissue contrast mechanisms such as diffusion imaging, magnetic resonance spectroscopy (MRS) and functional MRI (fMRI). Unlike PET-CT, the acquisition of PET and MRI data can be made truly simultaneous, allowing accurate spatial and temporal correlation of the PET and MR images, which leads to better image coregistration and provides the possibility to combine the dynamic information from PET and MRI (such as fMRI). And simultaneous PET-MRI also has the advantages of shorter imaging duration and reduction of positron range effect. Because of these unique characteristics of PET-MRI system, it is getting more and more attention in the past few years and a few combined preclinical systems have been developed and evaluated already.

2.7.2 Technical Challenges of Combining PET and MRI

Combining PET and MRI together in one device that can obtain both images simultaneously requires significant modification of PET systems due to the fact that the technologies used are mutually interfering.

The traditional PET photodetector, PMTs cannot operate under magnetic field because of the Lorentz force induced by the MRI main field interrupts the electron transfer process. Besides PMTs are very bulky in size which makes the mechanical integration of PET hardware inside the

MRI bore extremely difficult. So recently developed PET-MRI systems use silicon based photodetectors. However, the influence of electromagnetic fields on the detector system still cannot be underestimated. The interference of the EM fields on PET system strongly depends on the signal read-out architecture, shielding design and geometry of the PET system.

The rapid-switching MR gradient sequences can create strong eddy current in any conductive loop within the PET system. It may cause problem in the power supply chain of the PET system which in turn makes the PET performance unstable. The eddy current can also cause changing temperature which could also degrade the PET performance, especially for temperature-sensitive PET photodetectors. Unfortunately, the gain of silicon based photodetectors is usually very sensitive to temperature change. For example, each degree Celsius increase in temperature makes the gain of APD decrease by ~3%, while for SiPM the number could as high as 8%. Moreover, MRI gradient fields can also cause mechanical vibration so the components of PET system need to be very stable mechanically to avoid any loose connections.

The strong RF pulse can also cause misbehavior of PET systems. The electronic signal in the PET front-end electronics is usually very weak which makes the signal chain very susceptible to noise. We had observed very strong pickup noise with an earlier design of PET insert when MRI is pulsing RF[4].

The major interference on MRI from PET is main field homogeneity. The presence of any metallic objects in the PET scanner may disturb the main field homogeneity leading to distorted MR images. Furthermore, when the PET system is powered, the current on the power cable can also create an extra magnetic field creating non uniformity on the main field. Active shimming can be used to partially solve these problems depending on the order and magnitude of the distortion. Another issue is the degraded MR image SNR due the presence of the PET, especially when the clock frequency of the PET system or its harmonics is close to the MR resonance frequency. Thus special care is needed when designing the PET electronics.

Besides the magnetic compatibility issues between PET and MRI systems, there are also a few other practical issues. One of the most challenging issues of PET imaging in hybrid PET-MRI systems is attenuation correction since it is not practical to conduct PET transmission scans with positron-emitting rod sources or additional computed tomography (CT) scans and

fundamentally MRI images cannot provide direct information about photon attenuation map. Moreover, the RF coil inside the PET field of view (FOV) will also cause artifacts in PET images if its attenuation effect is not taken into consideration.

2.7.3 Approaches to combine PET and MRI scanners

In 1995, Christensen et al [57] first reported to use optical light guide in order to move the PMR-based detector modules outside the magnetic field. Number of research groups have followed this idea to develop simultaneous PET-MRI systems, such researchers from UC Davis [58],West Virginia University [59] and Osaka University [60]. In this configuration, the interference between the two scanners is minimized with only the scintillators being in the MR field-of-view (FOV). Thus there is no shielding required inside the MRI FOV and is relatively easy to implement with regular PET readout electronics. The major drawback of using long fibers is that there is significant loss of scintillation light which can result in degraded energy resolution, inaccurate crystal identification and poor timing resolution. Another PMT based PET-MR system was developed by a research group from the University of Cambridge[61]. The technique is different as it is based on split magnet design where the PET scanner is installed between the two 1T superconducting magnets and the PMTs are positioned in the radial direction of the MR scanner, as opposed to axial directions as employed in other approaches. However, it still suffers from the same scintillation light loss problem due to the 120 cm light guides used.

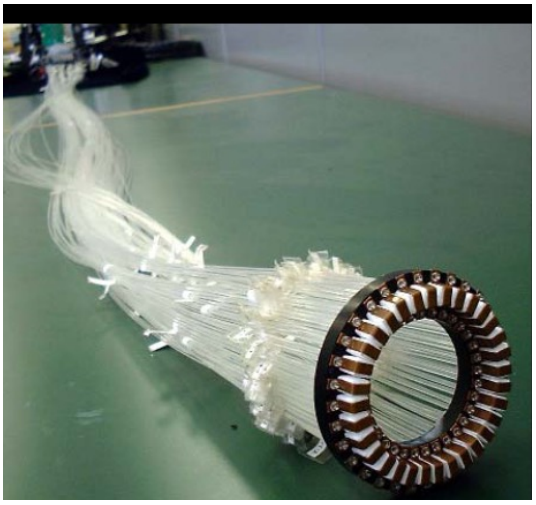

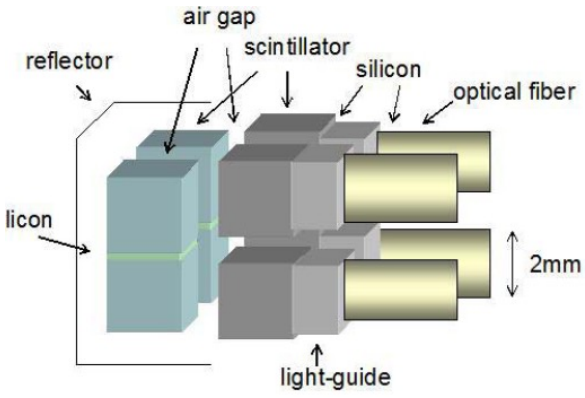

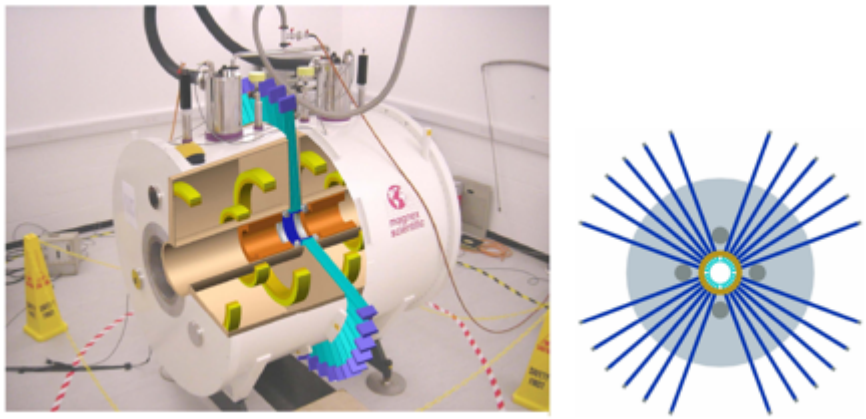

Figure.9 Top: One PMT based system with optical fibers [62] (©2004 IEEE), Bottom: PET-MRI system based on split magnet design [61] (©2006 IEEE)

Recently most simultaneous PET-MRI systems are based on silicon light detectors to avoid the usage of long light guides. Our group had developed a system which adapts the RatCAP scanner and uses 1:1 coupling between Cerium-doped Lutetium Yttrium Orthosilicate (LYSO) and APD[2] allowing rodent imaging at high field[4]. It is sufficiently compact axially to allow rat brain imaging as well as fit within a small-bore 9.4 T MRI. Researchers from University of Tuebingen, has developed an APD based PET detector which has an large inner diameter of 113 mm and operates with a 7T preclinical MRI[63]. And they have successfully demonstrated the ability of simultaneous PET/fMRI acquisition. The research group from University of California Davis has used a position-sensitive APD (PSAPD) with short optical fibers to build a full-ring PET with FOV large enough for imaging mice and could fit within a 7 T small animal MRI [64].

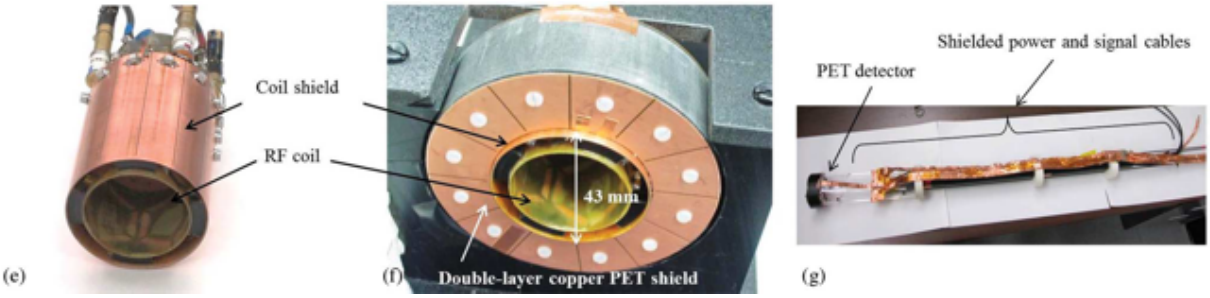

Figure.10 PET insert based on RatCAP technology [4](©2012 IEEE)

Although the APD has the advantage compared with PMT in the applications of PET-MRI, it has much lower gain, which is on the order of 50 compared to 10^6 of PMTs. So an APD based PET detector requires delicate front-end readout electronics and time and energy resolution are usually compromised. Most recent developments started to use a silicon photomultiplier (SiPM) as a replacement for an APD. This device is essentially an array of hundreds of micro APDs which are working under Geiger mode. The energy of the photons is measured by counting the number of micro cells fired, either digitally or in an analog way. Since it is working under Geiger mode, it allows an operating gain comparable to PMTs and is also insensitive to magnetic fields as a silicon device. The group at Seoul National University has developed a SiPM based small animal PET insert for clinical 3T MRI[65]. And in Japan, a high-resolution small-animal system with a phoswich-based Depth of Interaction (DOI) capability was built and evaluated in a low-field permanent magnet MRI[66]. Philips has developed a novel device called digital SiPM (dSiPM) putting as much processing power and digitization as possible at the detector. SiPMs are essentially digital devices so by measuring the energy of photon digitally, better gain stability can be achieved and the whole detector system can be simplified. The system based on dSiPM has been built and tested with 3T clinical MRI [67]. This device is still not widely available on market and is still at an experimental stage.

Chapter 3. BNL/PENN PET Insert- Technique and Validation

3.1 Introduction of the RatCAP technology

As described in Chapter 1, the detector technology originally designed for PET studies of awake animals [2] has been extended for applications including a PET insert for 9.4T MRI[3, 4], a wrist scanner to non-invasively access the amount of radioactivity in blood[5], a MR compatible breast PET scanner[6] and a plant PET scanner for plant biology studies at BNL[7], as well as the BNL/PENN PET insert. All these systems share the same detector technology[8].

A detector block is a 4-by-8 array of LSO crystals one to one coupled to a Hamamatsu S8550 APD array and readout by a custom Application Specific Integrated Circuit (ASIC). Each ASIC has 32 independent channels. Each channel includes a Charge Sensitive Preamplifier (CSP), optimized for this certain type of APD. The CSP is followed by a third order bipolar Gaussian shaper and a zero-crossing discriminator (ZCD) is used to measure the timing information for every event. The design of the ASIC is limited by space and power consumption so the energy information is not included in the output; instead an energy window is used as an energy discriminator. The output of the ASIC contains an asynchronous edge with timing information followed by 5-bit address of the fired channel. The ASIC is realized with TSMC 180 nm technology and each chip has a power consumption of 117 mW.

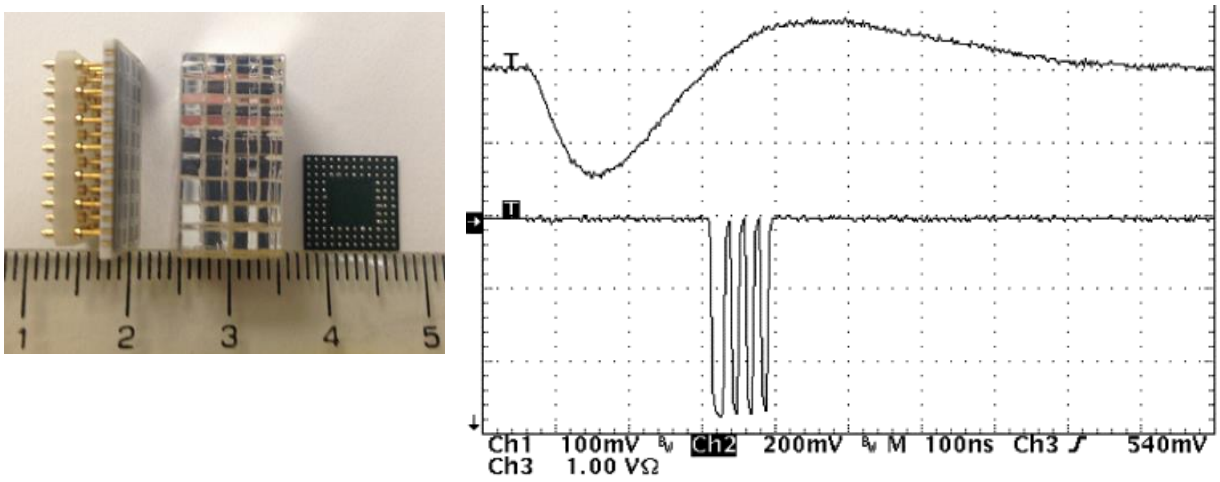

Fig. 11 (left) APD array, LYSO crystal and ASIC[9] (reuse with permission). (right) Bipolar signal and the output signal of the ASIC[8] (© 2007 IEEE)

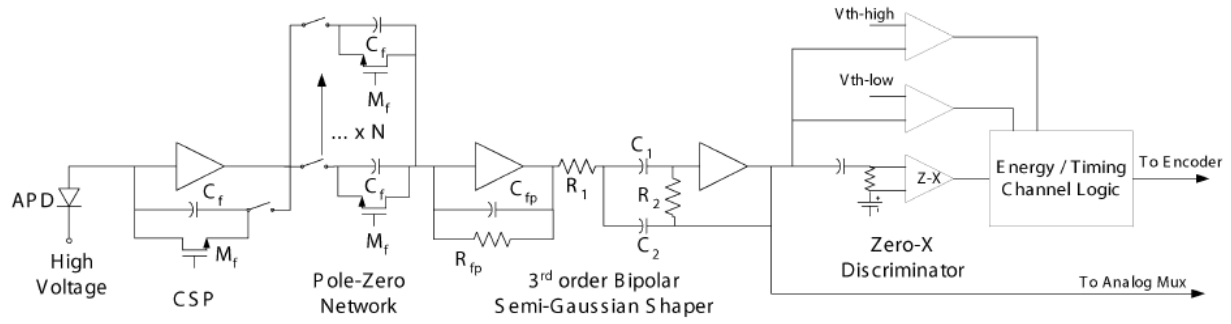

Fig. 12 Block diagram of the ASIC[8] (© 2007 IEEE)

3.2 BNL-PENN PET Insert Design

The new simultaneous PET-MRI system is being developed as a collaboration between Brookhaven National Laboratory (BNL) and the University of Pennsylvania. This system is capable of whole body rodent imaging in a large aperture MRI magnet. It is designed to be implemented with a commercial RF transceiver coil compatible with a Varian 9.4 T MRI. The cylinder-shaped system has an outer diameter of 20.6 cm and an inner diameter of 15.3 cm. The resulting axial FOV is 4.5 cm, limited by the PET, while the transaxial FOV is 7 cm in diameter, limited by the RF coil.

The system is based on an annular motherboard with 24 tower boards each of which contains 4 detector blocks. Each block has a crystal array of $\mathbf{2.4\times2.4\times14}$ mm LYSO scintillators and coupled with the same APD-ASIC detector as described above.

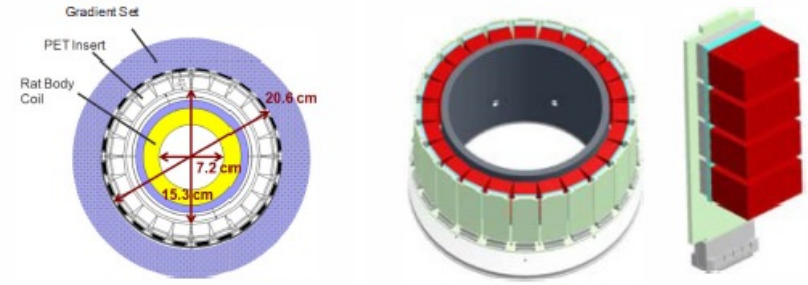

Fig.13 (left) Geometry of the scanner within the Varian 9.4 T MRI system, with the RF coil in place. (right) CAD drawing of assembled scanner and detector tower, LYSO detector blocks are in red, APD arrays are in blue.

Fig.14 (Left) Side view of the scanner, without the side cover. (Middle) Bottom view of the scanner, displaying four TSPM boards without SFP modules, plastic clamps are design to hold the SFP modules from pulling by the magnetic field, (Right) TSPM board with SFP module plugged in.

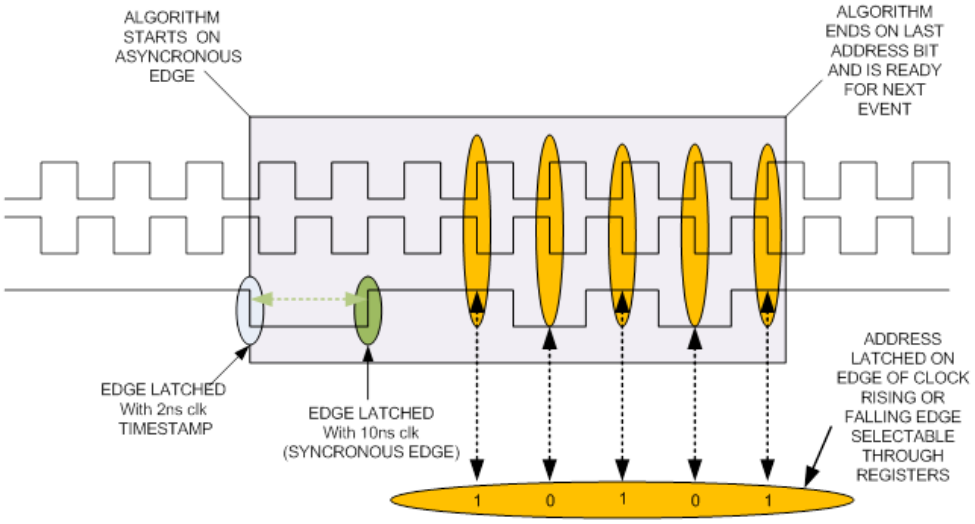

Figure.15 ASIC readout schematics, phase of the readout can be adjusted to read the following address bits correctly

The whole detector is mounted on a clear plastic tube so it can be placed in the bore of the 9.4 T MRI in UPENN as shown below. Cables coming out of enclosure are power cables and fiber cables. Beryllium copper tape is used for RF shielding on the support tube.

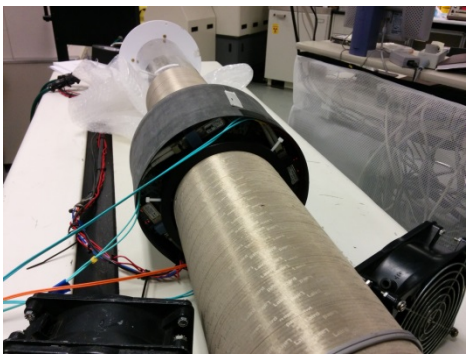

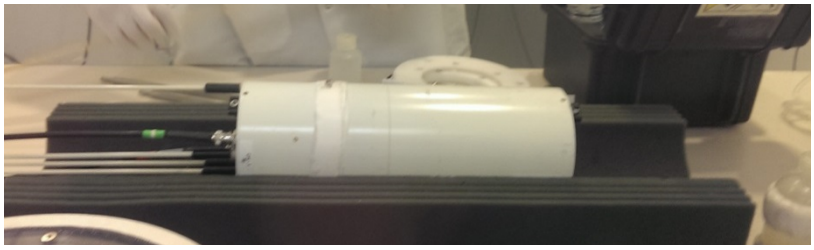

Figure.16 (Left)Scanner on the plastic tube, (Right) RF body coil

To reduce the power consumption on board, three different voltages, 2.6V, 3.3V and 5V are supplied to the board to minimize the number of onboard power regulators. Since all the power supplies need to be placed outside the MRI room, long power cables are necessary and there is significant voltage drop on the cables due to large amount of current (>10A). So the output of the power supplies need to be adjusted accordingly to achieve the voltage level on board as required. The whole system is operating with about 30 Watts of power which generates a significant amount of heat. A new MRI-compatible cooling system (fig.1) has been designed and 3D printed to stabilize the system performance. The cooling chamber is mounted on the tower board side of the system and connected to a powerful duct fan through 4 15-feet tubes so we can place the fan outside the MRI room to avoid creating interference to the MRI system.

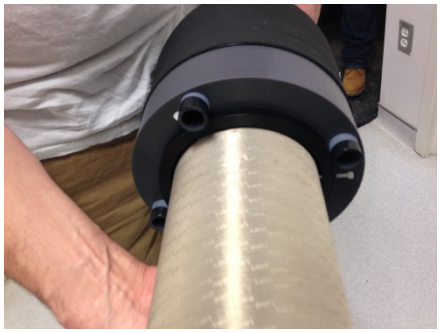

Fig.17 (Left) Cooling chamber, (Middle) Cooling chamber on the detector, (Right) The fan with four tubes connected.

3.3 DAQ system

Upon receiving the User Datagram Protocol (UDP) packets transmitted by the detector system, the data stream is handle by a data acquisition (DAQ) system based on the PHENIX RCDAQ and PMonitor frameworks [68, 69]. It is a Linux based software package which has high flexibility and is able to handle high speed data. This DAQ software extracts information of many singles event from the UDP packages and re-packs them into a new data structure called PHENIX Raw Data Format (PRDF) with information for later data processing and debugging. A real-time monitoring and data processing software has been developed based on ROOT [70]. More detailed information can be found in [9].

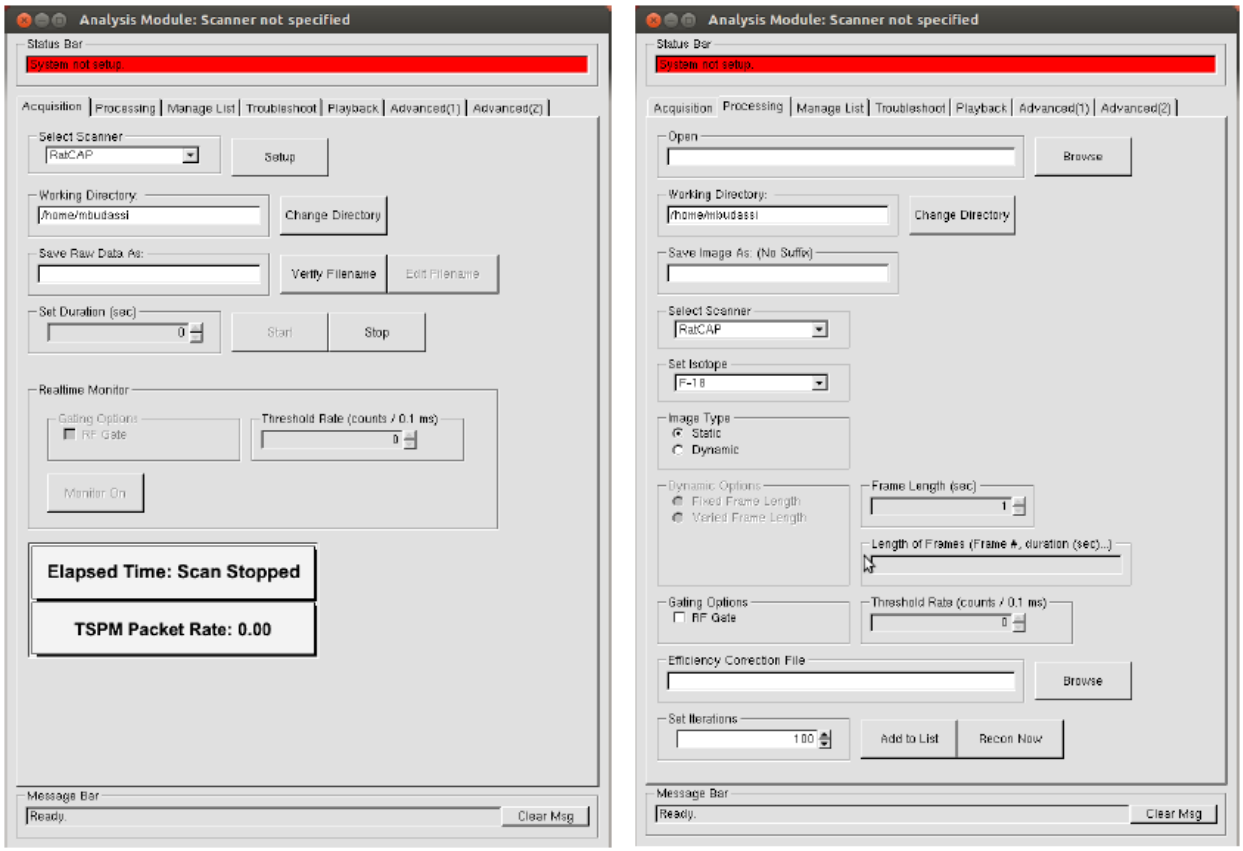

Figure.18 Acquisition (left) and processing (right) panel [9] (reuse with permission)

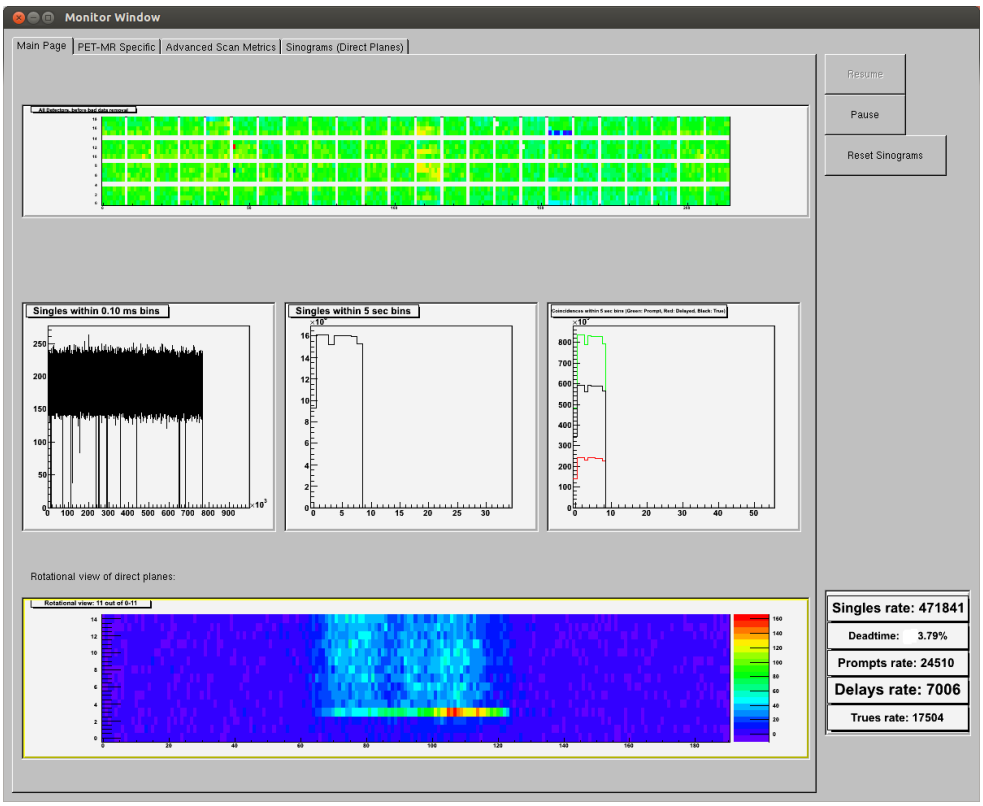

Figure.19 Real time monitor window, showing real time information including crystal hit map, time profile of singles, prompts, delays, also a rotating view of direct sinograms.

This detector is also capable of acquiring data with an external gating signal. There are two sets of hardware input pins for the gating signal. The system can operate under either "gating" mode or "flagging" mode. In "gating" mode, the system will stop acquiring data when the gating input is enabled while in "flagging" mode, with gating input enabled, the system will keep taking data but mark the raw data with a gating flag. Details of the raw data structure is shown in the section 3.4.

The gating function was tested with a signal generator, which generates square waves with 5V amplitude (to simulate the TTL gating signal from ECG) and 8 Hz frequency (to simulate the rat heart beat frequency). Three different duty cycles were tested, including 20%, 50% and 80%. Results are shown below.

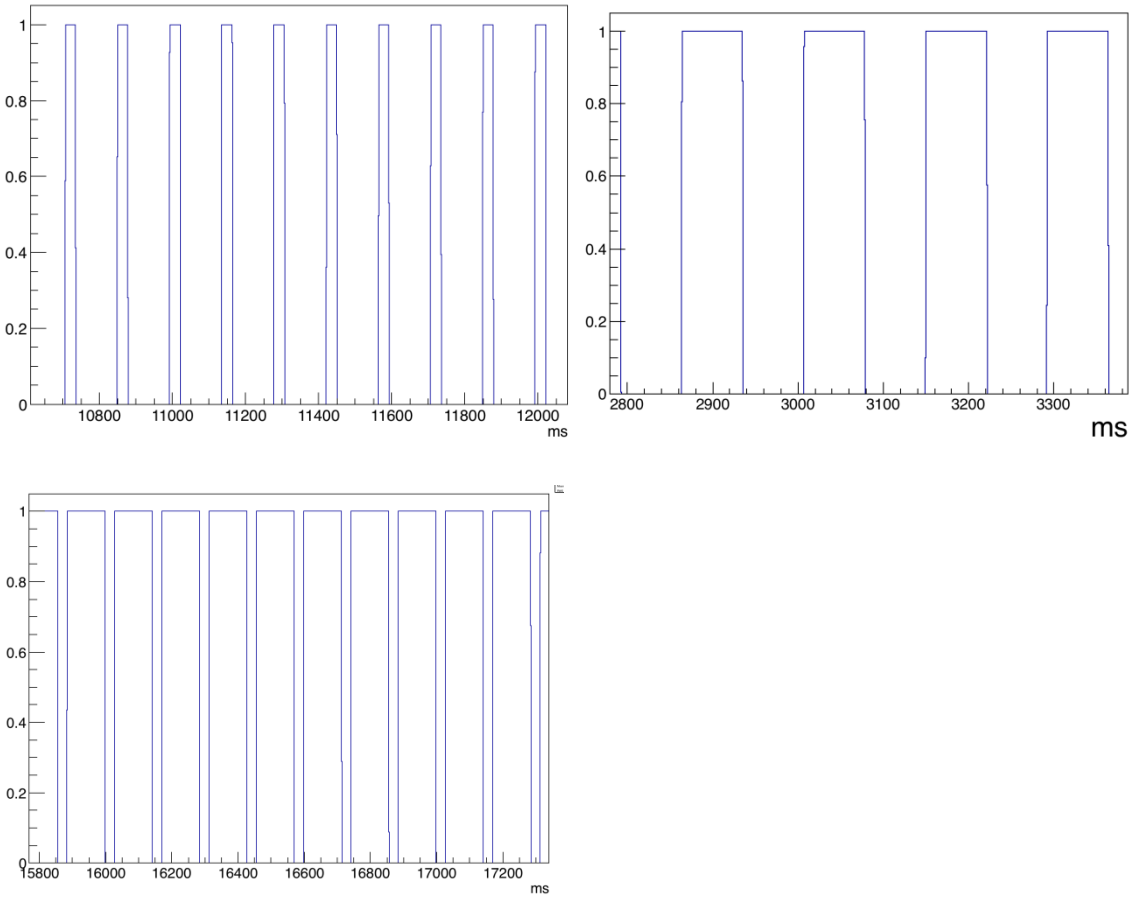

Figure.20 Top-left: 20% duty cycle; Top-right: 50% duty cycle; Bottom: 80% duty cycle. Each bin (1 ms time frame) of these figures is the ratio between the number of singles marked with gating and total number of singles within this frame.

3.4 Detector Calibration and Data Processing

The raw data of the detector system is a vector of 64-bit words each representing one single event as shown below. Since there are four TSPMs with this system, TSPM decoding is done with the RCDAQ system by adding the index of Ethernet port in the PRDF header. The first two bits are corresponding to two sets of gating input on the motherboard. When there is gating input (High), the corresponding gating bit is turned from 1 to 0. ASIC number is used to decoding the position of the fired block out of 24 blocks in this quadrant while channel number shows the fired crystal out of 32 crystals in one block. 45 bits are used for timestamp with 2 ns second time bin so the total time range is ~39 hours. And each time resetting the power or using the resetting function on board can clear the time clock back to 0 so no "time overflow" would occur for most applications.

63	62	61 - 57	56 - 52	51 - 46	45 - 0
CARDIAC	RFGATE	ASIC NUMBER	CHANNEL	SAMPLE SERIAL	TIME STAMP

Figure. 21 Bit map of raw data.

The singles events are then sorted with C++ "set" object which is part of the Standard Template Library (STL). Since the time complexity of this operation is Nlog(N) with N the number of events and the raw data is usually too big to be fitted in the memory, the raw data is divided into multiple frames and coincidence processing is done with each frame independently. Then the prompts and randoms are binned into fully 3D sinograms with dimension of $191 \times 96 \times 256$. Each sinogram bin is a 4-byte integer so the size of a sinogram is ~18MB.

3.4.1 Energy calibration

It is important to get uniform response from all crystals to achieve a good image quality. Even though part of the non-uniformity effect can be corrected by normalization later, it is still essential for the accuracy of single scatter simulation. As described earlier, there are no ADCs implemented in the RatCAP ASIC for energy information. Thus acquiring the energy spectrum requires a special "threshold scan". Energy resolution is measured with a Ge-68 rod source placed in the middle of the field of view. Counts rate was measured with different low level energy discriminator (LLD) settings to acquire an "integral" energy spectrum. Then the energy spectra for each channel are calculated by taking the derivative of the measured count rates as a function of energy threshold. The energy resolution for a given crystal was measured as ~22% FWHM.

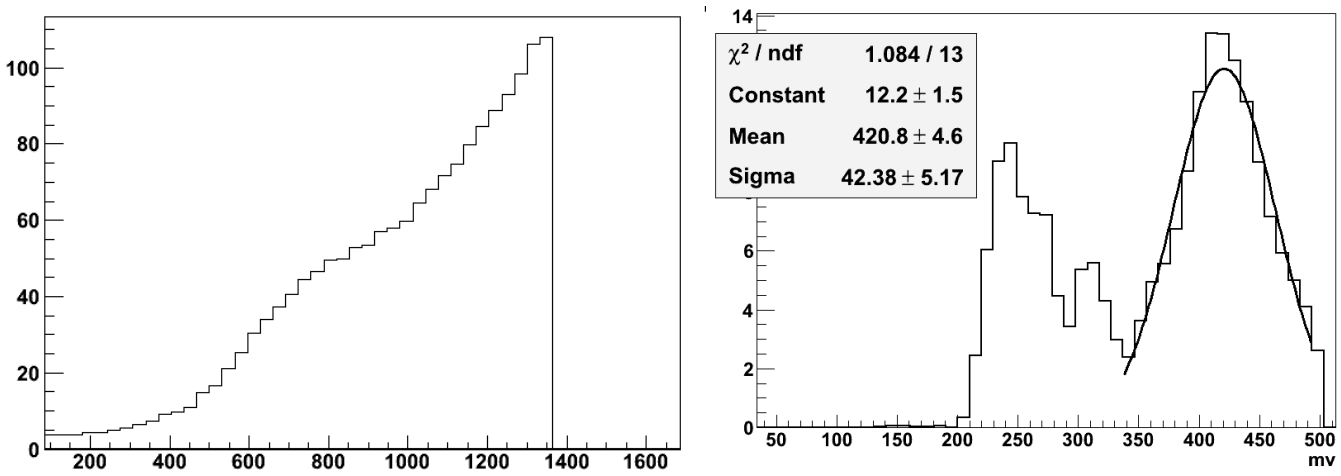

Figure.22 (Left) the integral energy spectrum for one channel; unit is ADC values (Right) the energy spectrum for one channel

Since the ASIC allows the programming of individual gains for each channel, an initial threshold scan is done with unity gain for each channel and the gains for each channel can be calculated from the energy peak centroid locations. However, the dynamic range of the ASIC gains is limited (1-2.7). And in practice setting ASIC gains are not enough to align all peaks together. So the peaks of all crystals is still not perfectly aligned but spreading over a much narrower range after gain correction. This can be further improved by rearranging the blocks with similar intrinsic gain values to the same quadrant and then setting different APD bias voltages to different quadrant.

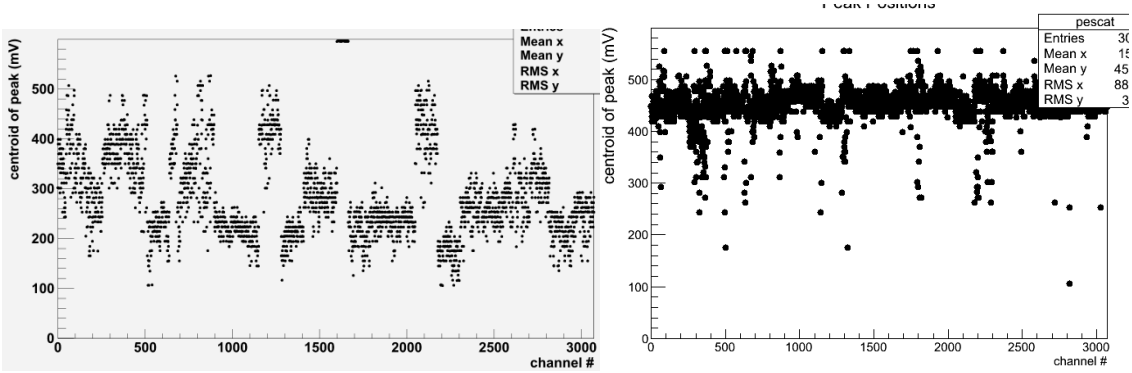

Fig.23 (left) scatter plot of peak positions of all channels with unity gain (Right) Scatter plot of peak positions of all channels with adjusted gain

Moreover, the new cooling system provides a stable air flow for the detector and greatly improves the gain stability of the PET system.

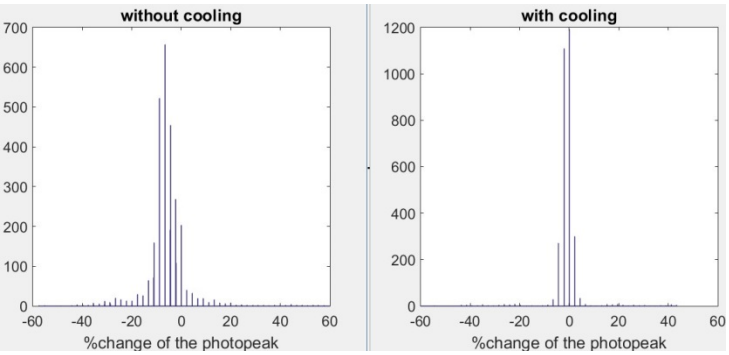

Fig. 24 (left) histogram of the gain changes of every channel between two gain calibrations separated by a day, without the new cooling setup; (right): same plot with the new cooling system. The x-axis is the percent of change in terms of the photo peak position.

3.4.2 Timing calibration

Any differences within the photon detection process may cause a time delay (called t0) between two channels, such as ASIC triggering circuits, gain variations and signal pathway to TSPMs. And different crystal pairs would have different time offsets so the overall effect broadens the overall system timing resolution. Without correcting this effect, the system would require a large energy window to accommodate all crystal pairs, resulting in an increased randoms fraction. Time correction is done by acquiring a very high statistic data with a uniform phantom. The central 3 radial bins of each projection angles are used and time difference histograms are made for those bins. Gaussian fitting is applied to these histograms and the positions of each peak are fed into another program to perform singular value decomposition (SVD). The number of unknowns is 3071 (the number of crystals -1) while the total number of equations is $3 \times 96 \times 256$ (in reality the number of equations can be slightly smaller than this, since some bins do not have enough counts to make a good Gaussian fit), so this overdetermined problem is solved in the least squares sense. After time correction, the time resolution of the system is ~9 ns FWHM. The time resolution of this system has insignificant correlation with time walk caused by gain variation which means the timing correction factors are relatively stable over time. The coincidence time window of this system is set to be 20 ns.

The t0 stability has also been evaluated. The figure below shows the t0 difference histogram from two calibrations separated by 1 days. The FWHM of this time difference is less than 1 ns.

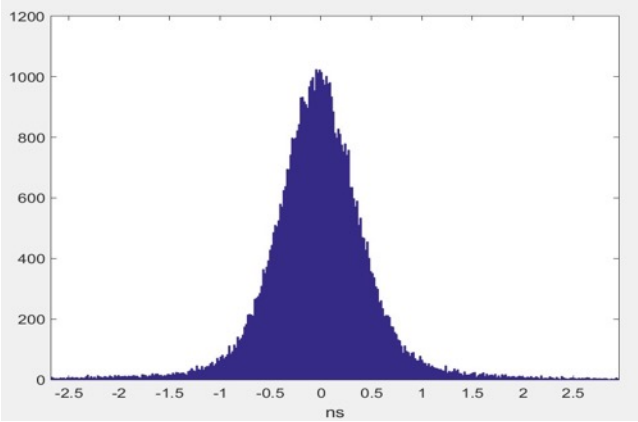

Figure.25 Histogram of t0 difference between two calibrations

Since this system has four TSPMs, one unique problem is the time offsets between quadrants shift frequently (time offsets within quadrants are still stable). To solve this problem, we plot the time difference histograms between 4 quadrants to show the time offsets and apply correction to the time correction factors. The cause of this issue is still under investigation.

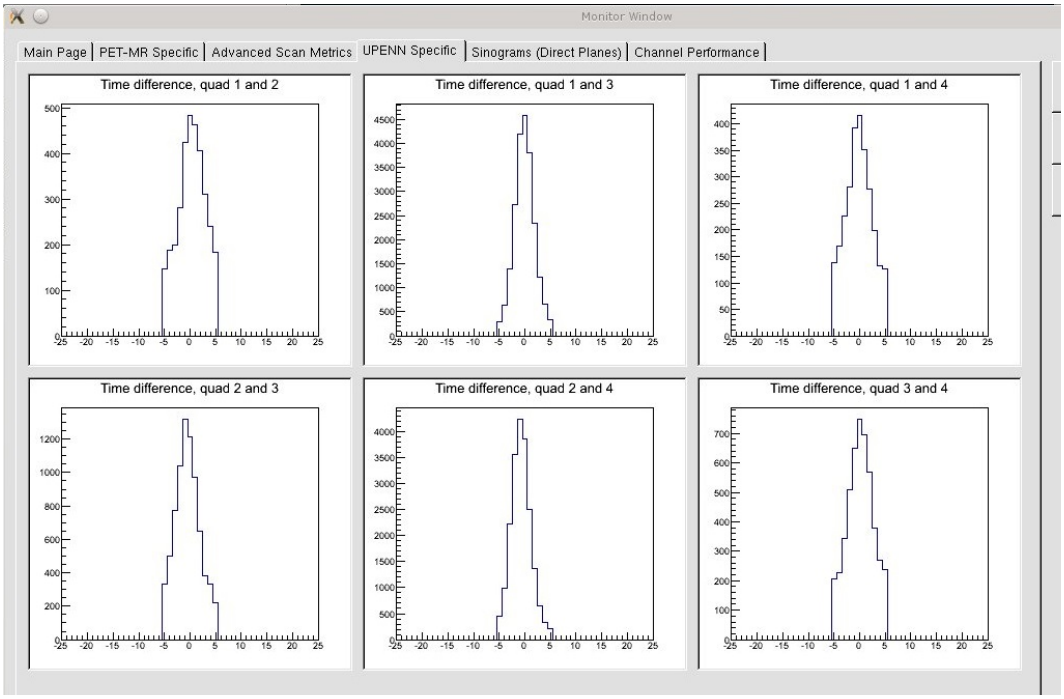

Figure.26 Monitor window showing time difference between each two quadrants

3.4.3 Normalization

Direct normalization is used for this system. A high statistics dataset is acquired with a uniform phantom (usually the same dataset for time correction). Since a significant portion of prompts are scattered events, scatter correction is needed for accuracy. The algorithm of calculating normalization factors is described as follows:

1. Reconstruct a non-corrected phantom image

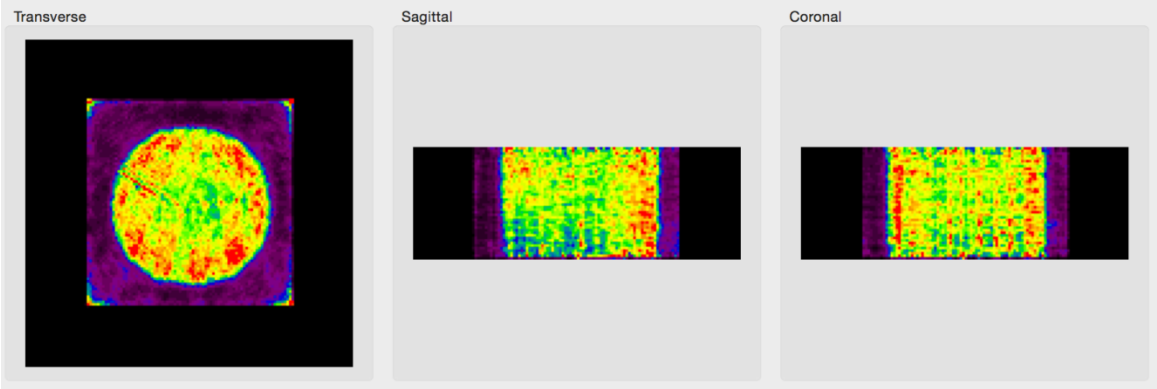

Figure.27 Uniform phantom image without any corrections

2. Generate an "ideal" uniform phantom emission and transmission image based on this image

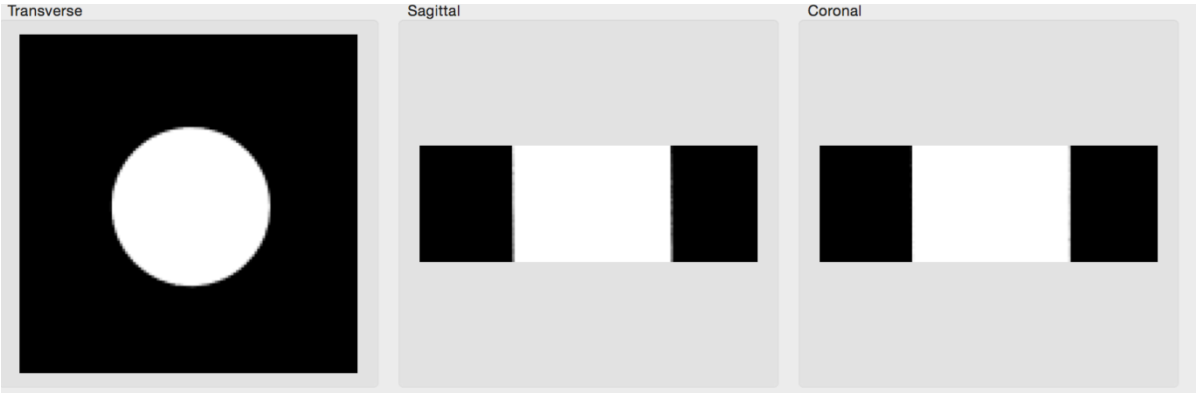

Fig.28 "ideal" emission image with uniform value in the phantom area

3. These ideal emission and transmission image are used as the input of SSS and a scatter distribution is created. Note that at this point the scatter distribution will not be fit to the tail of the data.

4. The scatter distribution is scaled by fitting to the tail region of the experimental data. The fitting model is $A \times scatter + c$ where c is a constant term which includes multiple scattering events and random events (assume random distribution is close to uniform). And then it is subtracted from the data to create a "scatter free" data. The normalization factors are obtained by calculating the ratio between this scatter free data and the "ideal" data.

5. The normalization factors are only in the center region within the phantom. So extrapolation is used to obtain factors in the rest area.

6. Note that the scatter distribution in step 4 does not include the real detector efficiency. So the normalization factor from step 5 is applied to the scatter distribution to generate a new distribution closer to the real scatter distribution. Then step 4 and 5 are repeated. In other words, the whole normalization process is done in an iterative manner. Usually four iterations are good enough to achieve a convergence.

3.5 Image reconstruction

3.5.1 Monte Carlo simulation based system model

The method is an extension of the reconstruction algorithm used in all of our previous systems[9, 71, 72]. Monte Carlo simulation potentially can give a very accurate model of the system response. The major drawbacks are the simulation requires a very long time and the system matrix could be very big. Historically it has not been a problem for our other systems because of their relatively small scale. However, with the BNL-PENN PET insert, the full system matrix would be more than 100 gigabytes which is not practical to implement. A proof of concept simulation was done with only 4 rings (out of 16 rings in total) since the detector has four folds of symmetry in the axial direction. However in this way the detector is not operated in fully 3D model because the maximum ring difference is 3 and there are no LORs between two modules in different axial positions.

The simulation is done with a C++ based package called Simulation System for Emission Tomography (SimSET) developed by University of Washington [73]. Compared with the more popular simulation package GATE [74] (which is based on the well-known high energy physics

simulation package Geant4), SimSET is optimized for PET applications so it is significantly faster with some flexibility trade-off. And SimSET is also a much smaller package then GATE which makes it a very convenient tool to do parallel computing. The basic simulation setup is similar to those for our previous systems [72]. However, a newer version of SimSET (2.9.1) is used instead of version 2.6.2.4 in the past. The new version supports block based PET detectors while the old version only has ring shape detector geometry built in (upon which we overlaid our detector geometry by customizing the code). Thus potentially it should give more accurate results for our block based PET systems.

Since the FOV has only 4 rings simulated and the image slice thickness is chosen as half of the crystal pitch, there are 9 image slices and each slice contains 10029 voxels. And the sinogram has $191 \times 96 \times 16 = 293376$ bins so the full system matrix is about 5.9G. The system matrix is then compressed with the open source Lempel-Ziv-Oberhumer (LZO) algorithm and the resulting final system matrix is 2.7G. The whole simulation process is distributed on the Open Science Grid (OSG) [75] in the manner that each job only contains 9 voxels with the same transaxial position. With 10 million decays simulated per voxel, the whole simulation could be done a few hours instead of months with a single workstation.

With this system matrix, images are reconstructed with the same framework as our other systems. A sample image is shown below.

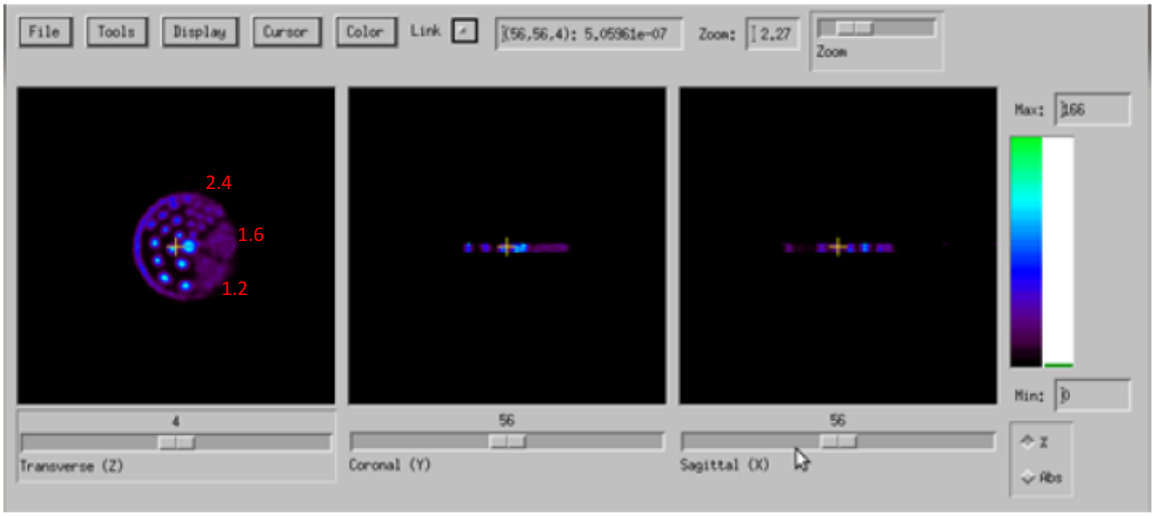

Fig.29 Image of a hot Derenzo phantom, 2.4 mm rods can be separated

3.5.2 Reconstruction with STIR

STIR is an open source software for use in tomographic imaging[76]. It provides a Multi-Platform Object-Oriented framework for all data manipulations in tomographic imaging. It is a C++ based package with good modular design. Multiple analytic and iterative 3D reconstruction algorithms are implemented such as FBP-3DRP (Filtered back projection with 3D reprojection), OS-MAP-OSL (Order Subset Maximum A priori with One Step Late) and list-mode EM. It also has tool sets for data processing such like SSRB (Single Slice Rebinning), FORE (Fourier Rebinning), arc correction and math tools for sinograms and images. Motion correction and SSS based scatter correction are implemented in STIR too.

STIR takes Interfile as the input data format. This format uses a separate header for each binary image file. The structure of sinogram has four dimensions, including segment, axial coordinate, view and tangential coordinate. The geometry of the detector is also defined in this header however right now STIR only supports detector geometry with equally spaced crystals both on axial and transaxial directions. A sample Interfile header for the BNL-PENN PET insert is shown below:

```
!matrix size [4] := 31
matrix axis label [3] := axial coordinate
!matrix size [3] := { 16,15,15,14,14,13,13,12,12,11,11,10,10,9,9,8,8,7,7,6,6,5,5,4,4,3,3,2,2,1,1}
matrix axis label [2] := view
!matrix size [2] := 96
matrix axis label [1] := tangential coordinate
!matrix size [1] := 191
minimum ring difference per segment := { 0,1,-1,2,-2,3,-3,4,-4,5,-5,6,-6,7,-7,8,-8,9,-9,10,-10,11,-11,12,-12,13,-13,14,-14,15,-15}
maximum ring difference per segment := { 0,1,-1,2,-2,3,-3,4,-4,5,-5,6,-6,7,-7,8,-8,9,-9,10,-10,11,-11,12,-12,13,-13,14,-14,15,-15}
Scanner parameters:=
Scanner type := PENN
Number of rings                          := 16
Number of detectors per ring             := 192
Inner ring diameter (cm)                 := 15.29
Average depth of interaction (cm)        := 0.1
Distance between rings (cm)              := 0.24
Default bin size (cm)                    := 0.24
View offset (degrees)                    := 0
Maximum number of non-arc-corrected bins := 191
Default number of arc-corrected bins     := 191
Number of blocks per bucket in transaxial direction        := 1
Number of blocks per bucket in axial direction             := 4
Number of crystals per block in axial direction            := 4
Number of crystals per block in transaxial direction       := 8
Number of detector layers                                  := 1
Number of crystals per singles unit in axial direction     := 1
Number of crystals per singles unit in transaxial direction := 1
end scanner parameters:=
effective central bin size (cm) := 0.24
number of time frames := 1
```

Fig.30 A sample Interfile header. This header matches the raw sinogram format without any compression

A cold Derenzo phantom image was reconstructed with STIR. The system matrix was calculated on-the-fly with Siddon's ray tracing. Ten rays were used for each LOR to get more accurate results than single ray tracing. MLEM algorithm (1 subset) was used with 50 iterations.

Random correction and normalization were applied with this phantom. Rods with size of 2.4 mm can be seen.

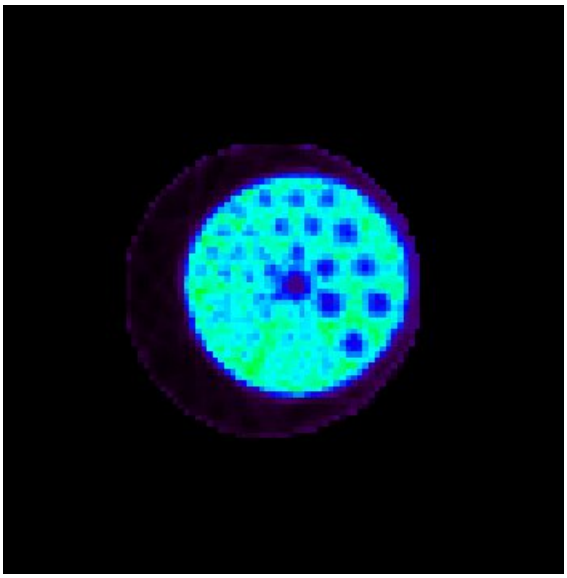

Figure.31 Cold Derenzo phantom image, reconstructed with STIR

Currently we are using the reconstruction package from our collaborators at the University of Pennsylvania [13, 77]. List mode reconstruction is used with Kaiser Bessel blob basis functions. The system response matrix is calculated through on-the-fly ray tracing. The final image is obtained by resampling the blob basis function. More images are shown in Chapter 4.

Chapter 4 Performance Evaluation and Image Results

4.1 Performance Analysis

The section presents a performance evaluation of the BNL-PENN PET insert using standard criteria. The evaluation has been made to comply with NEMA[78] as far as possible. However, due to limited access to required resources, the experimental design is not completely identical. The section also includes the PET system performance under MR environment as well as MR image quality parameters when PET is present.

4.1.1 PET spatial resolution

The spatial resolution of a system represents its ability to distinguish between two points after image reconstruction. Although spatial resolution does not fully represent the condition of realistic imaging situations, in which there is significant tissue attenuation and scatter, or where a limited number of acquired events require a trade-off between resolution and noise, the measured spatial resolution provides a reproducible comparison among scanners and gives a highest achievable performance of the scanner system.

A capillary tube (ID = ~1.1mm) filled with a tiny amount of FDG solution (<50 μCi) was used as a point source in this measurement. The tube was taped on a piece of foam with markers to place the source in different transaxial locations. The source was placed at 0, 5mm, 10mm, 15mm, 25mm transaxially and in the center axially. More than 1 million prompt coincidences were acquired in each case. FBP reconstruction is required in NEMA standard for resolution evaluation. However, FBP requires uniform sampling in the projection space while the raw sinogram is actually non-uniform sampling due to the block based detector and sinogram interleaving. The 3D sampling pattern is shown in Fig. 35 below. Obviously there are gaps caused by the block structure and the sampling rate changes from center to edge (arc effect). Thus the raw sinogram needs to be resampled into a uniform grid. This interpolation process is achieved with Delaunay triangulation of the data which is available in MATLAB. The sinogram was resampled into a uniform grid which ranges -70 to 70 mm in r direction with 0.25 mm bin and 0-179 degree in phi direction with 1 degree bins.

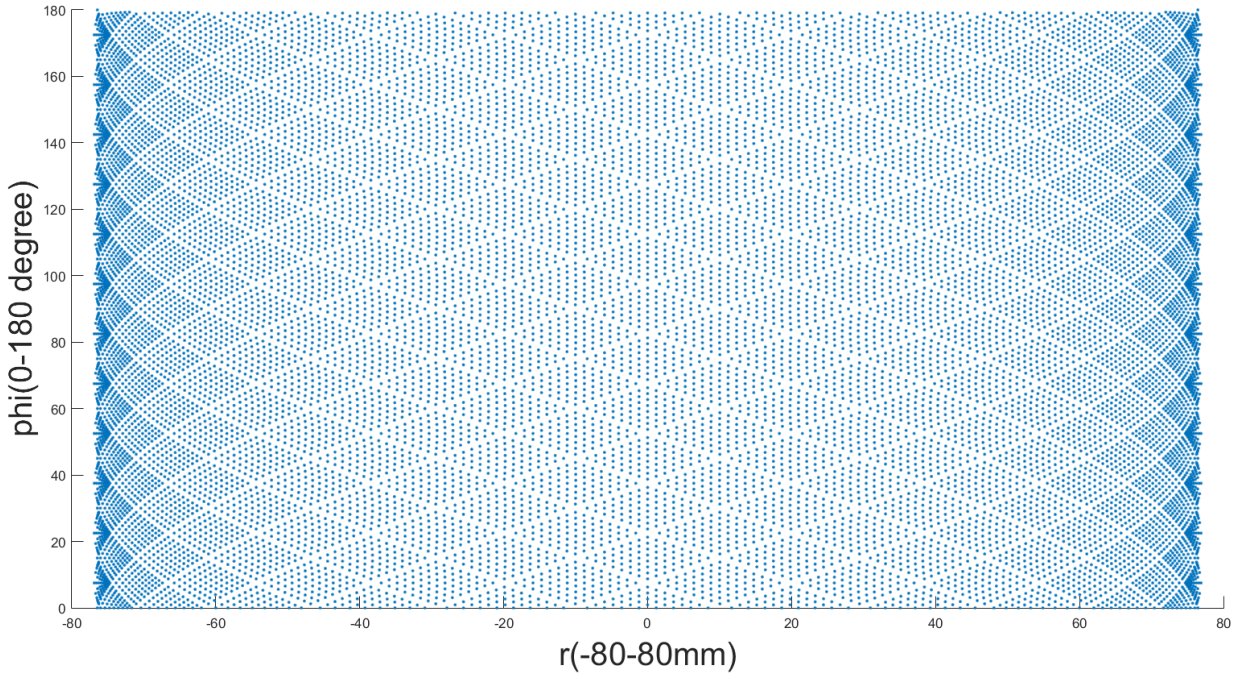

Figure.32. The sampling pattern of the raw sinogram

To increase the sampling rate in axial direction, +1/-1 slices of the sinogram are averaged into the planes in between each two direct planes (similar to SSRB). So the axial pitch between two adjacent sinogram slices are now half of the crystal pitch. FBP is done with basic ramp filter and no smoothing was employed on the images. The spatial resolution of the point source response function in both tangential and radial directions were measured by forming one-dimensional response functions through the peak of the image volume in two orthogonal directions. The response function is formed by summing all one-dimensional profiles that are parallel to the direction of measurement and within at least two times the FWHM of the orthogonal directions. FWHMs were measured from Gaussian fits on these one-dimensional profiles.

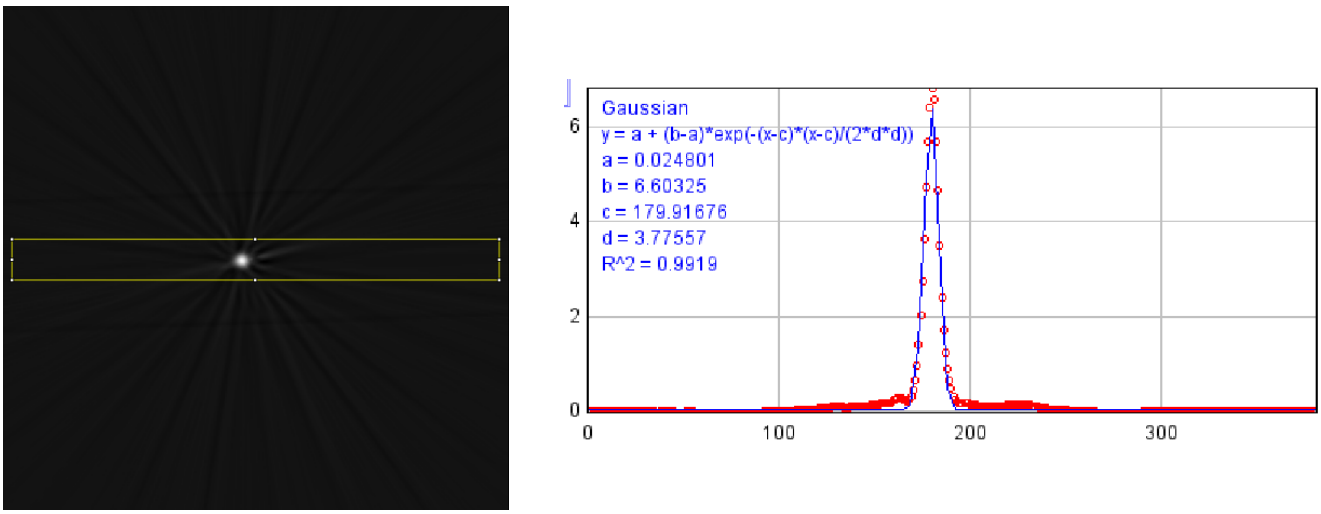

Figure. 33. (Left) Image of the point source in the center; (Right) The Gaussian fitting to extract resolution

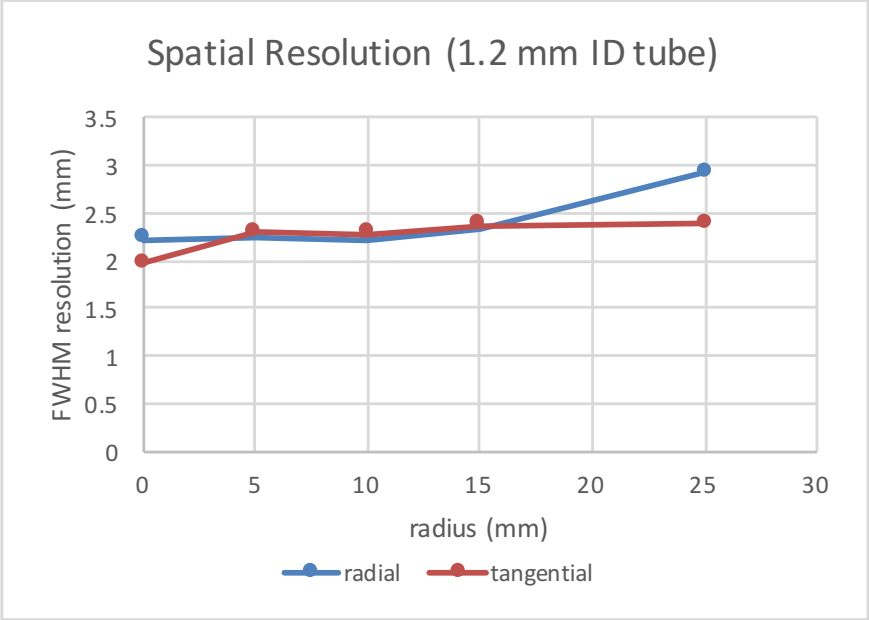

Figure.34 Spatial resolution in different locations across the FOV

The ratio between resolution (at 5 mm) and crystal size of most reported preclinical systems [43] are bigger than one, while this ratio for the BNL-PENN PET insert is ~0.95. Note that the point source size was not deconvolved from the result and NEMA standard requires the size of the point source should be no more than 0.3mm in all dimensions. Thus the resolution result of this system should be even better. The major reason of this outstanding performance is

due to the fact that this system has a one-to-one coupled crystal and photo detector which gives a perfect crystal decoding.

4.1.2 Count Rate Capability

Count rate capability is another important performance measurement of a PET system. It quantifies a PET system's ability to handle objects with high activity and to achieve high SNR in a limited time frame of data acquisition. Due to the photon counting nature of PET systems, there is a limit to the highest data acquisition rate achievable. Any part of the DAQ chain may limit the highest data rate achievable. The most fundamental limitation is the speed of the scintillator since the output (low energy photons) of any scintillator would contain a rising edge and a tail. When the rate of the incoming gamma photon is high enough, the signal of current gamma photon may overlap in time with the tails of previous gamma photons, which can degrade the information it carries. A similar pile-up effect also exists with the front-end electronics since electronics circuits always have limited bandwidth and in PET applications the bandwidth of electronics is usually being limited intentionally with shapers to achieve higher SNR (by limiting the contribution of noise). Moreover, the communication pathway and DAQ computer could also be the bottle neck if they are not designed properly. Modern PET systems are usually fast enough to handle scans in most normal applications. The BNL-PENN PET system can achieve singles rate of more than 10M/s which is far beyond the realistic event rate of a normal animal scan. However, detecting more counts does not mean better SNR in the final images because the rate of random events increases more quickly than the rate of prompts events. A better metric to measure the SNR of a PET system is Noise Equivalent Count Rate (NECR), developed by Strother[79] in the 90s.

If using letter P, T, R and S to represent counts in prompt events, true events, random events and scattered events, their relationship can be written as:

$P = T + R + S$ or $T = P - R - S$

The noise level of true events can be written as (Δ means noise):

$$\Delta T = \sqrt{(\Delta P)^2 + (\Delta S)^2 + (\Delta R)^2}$$

And considering the Poisson statistics,

$$\Delta T^2 = P + R + S$$

By definition, NECR is the count rate at which the SNR is the same as if there is no additive noise (randoms and scatters). Thus

$$\sqrt{NECR} = T / \Delta T \text{ so } NECR = \frac{T^2}{\Delta T^2} = \frac{T^2}{P + R + S}$$

The count rate capability is measured with the NEMA "rat-like" phantom[78]. This phantom is made of a solid, right circular cylinder composed of high density polyethylene 150 mm long and 50 mm in diameter. A cylindrical hole (3.2 mm in diameter) is drilled parallel to the central axis at the radial distance of 17.5 mm. The test phantom line source insert is clear flexible tubing with a fillable section of 140 mm long. We started with 1 mCi of F-18 FDG solution filled in the phantom. The data was taken with 425 keV energy threshold. The total acquisition time is about 14 hours. Furthermore, since the crystal (LYSO) used in this system has intrinsic activity, measurement is also performed without activity in the FOV to estimate background.

The data is then binned into multiple time frames. Since the count rate is higher in the beginning, the first 16 frames have 15 min duration while the following 24 frames have 25 min duration. For all sinogram slices in all frames, pixels located farther than 8 mm from the edges of the phantom were set to zero. For each projection angle within a sinogram, the pixel with the highest value gives the location of the center of the line source. A +7/-7 mm strip is then defined around this center. Within this strip, the combined random and scattered event is calculated by taking average value of the two pixels on the edge of this strip and multiplying this average with the number of pixels in this strip. Then the counts of true events can be estimated by subtracting the additive noise in the strip from the total counts in this strip. The overall additive noise is then calculated by subtracting the counts of true events from the overall counts. The same operation is applied to all sinogram frames and the measurement only containing intrinsic activity. And the crystal background was subtracted from each frame. The source activity of each frame is calculated from the initial activity and decay constant of FDG.

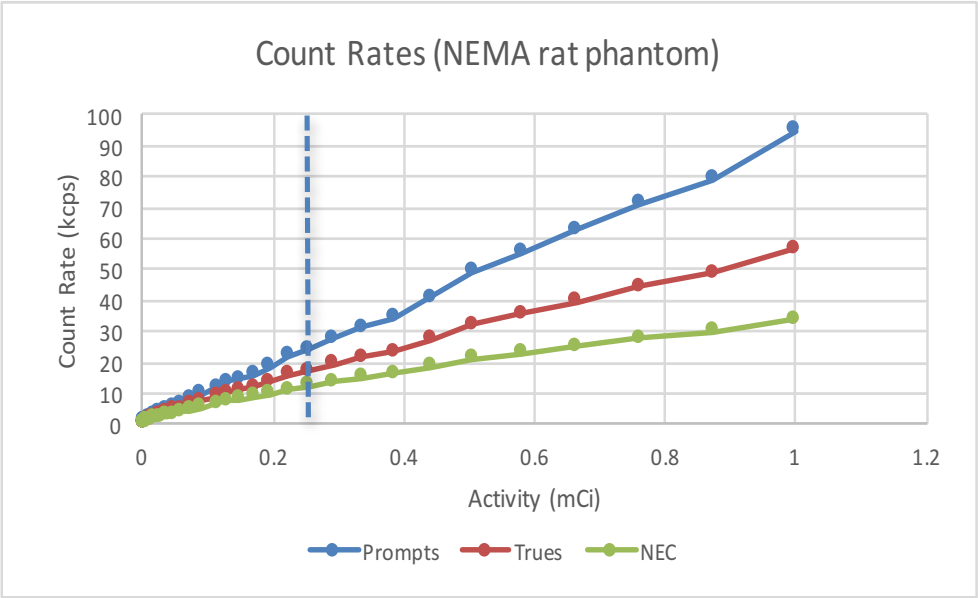

Figure 35. Count rates of prompts, trues and NEC at different activities. The dashed line indicates approximately the activity level at which many rodent scans are performed.

The NEC at 10 MBq at 425 keV threshold is about 13 kcps, while the reported NEC of other systems is in the range of 19 to 137 kcps at 10 MBq[43]. This number is mainly determined by sensitivity, time resolution and energy resolution of the system. The position of Peak NECR of the system is above 1 mCi and its exact value will need further measurements.

4.1.3 Sensitivity

Sensitivity of a PET system is defined as the ratio between the true coincidence events detected and the overall positron decays that happened in the source during the same time frame. The sensitivity of a system represents its ability of achieving high SNR with limited activity inside the FOV. It is mainly determined by the solid angle coverage of the system. Scanners with bigger axial length and smaller diameter would have higher sensitivity. Other important factors are the type of crystal and the length of crystal. Obviously with the same type of crystal, the longer the crystal is the better the stopping power which in turn gives better sensitivity.

Sensitivity was measured with a 5.5 μCi ^{22}Na source (as determined by the vendor-supplied activity value and reference date). This source was centered transaxially and moved across the axial FOV in steps of 2.4 mm (which is the crystal pitch). A scan lasting 2 min was taken in each position. The location of the source was verified with the direct sinogram readings

from the real time monitoring window. The scan was conducted with two different energy thresholds, 350 keV and 425 keV. A background scan without source was also conducted to account for the crystal intrinsic activity.

The sensitivity calculation procedure follows the NEMA standard. For each projection angle of the sinogram, the pixel with the highest value was located and all pixels greater than 1cm from the peak value was set to zero. And then the total counts in the sinogram were summed with no other corrections for scattered or random events performed. The same operation was also applied to the background datasets. The system sensitivity is calculated as:

$$Sensitivity = \frac{R - R_B}{A \times 0.9060}$$

Where R is the count rate of true events, R_B is the count rate of background, A is the activity in Bq and 0.9060 is the positron branching fraction for ^{22}Na.

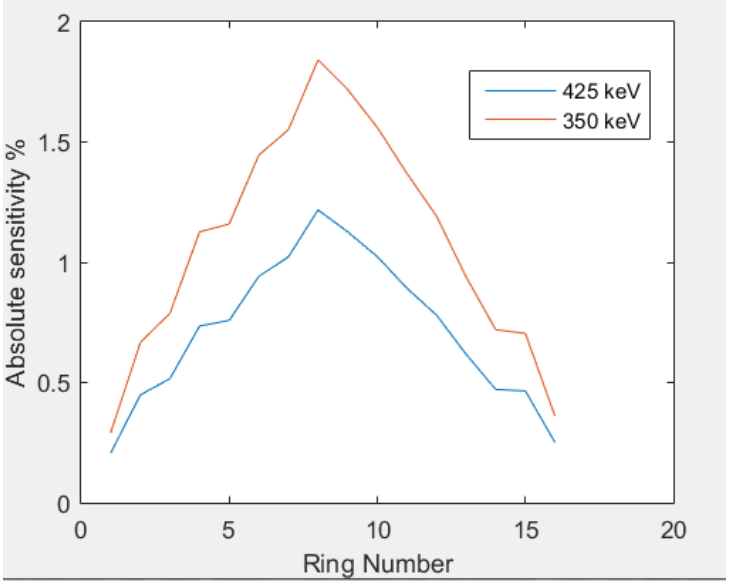

Figure.36 Sensitivity profile as a function of axial position

The peak sensitivity shows the maximum sensitivity at the center of the axial FOV, at about 1.84% and 1.22% for 350 keV LLD and 425 keV LLD correspondingly. The absolute sensitivity, calculated as the average absolute sensitivity over the entire axial FOV, is 1.09% and 0.71% for 350 keV LLD and 425 keV LLD correspondingly. The range of peak sensitivity of

other preclinical systems is 1.2% to 6.7% and the range of absolute sensitivity is 0.61% to 2.8% [43]. The relatively low sensitivity of this system is due to its short axial FOV and large transaxial FOV which is necessary for placing the RF coil inside.

4.1.4 NEMA Image Quality

Generally speaking, there is no one simple method to evaluate the performance of a PET system, since different data acquisition and reconstruction parameters might be used for different applications. In other words, there is no one best set of parameters most suitable for all applications. The choice has to be made for each specific application as trade-offs between noise property, image resolution, scan time, reproducibility etc. Thus the image quality measurement based on NEMA standard can only give indications of image quality for that particular imaging situation. The purpose of the NEMA image quality measurement is to simulate the imaging situation of a total body study of a small rodent with hot lesions, as well as uniform hot and some cold areas. The figure below shows the images of the NEMA image quality phantom. The phantom was filled with 100 uCi of F-18 FDG and imaged for 20 minutes as indicated by the NEMA standard.

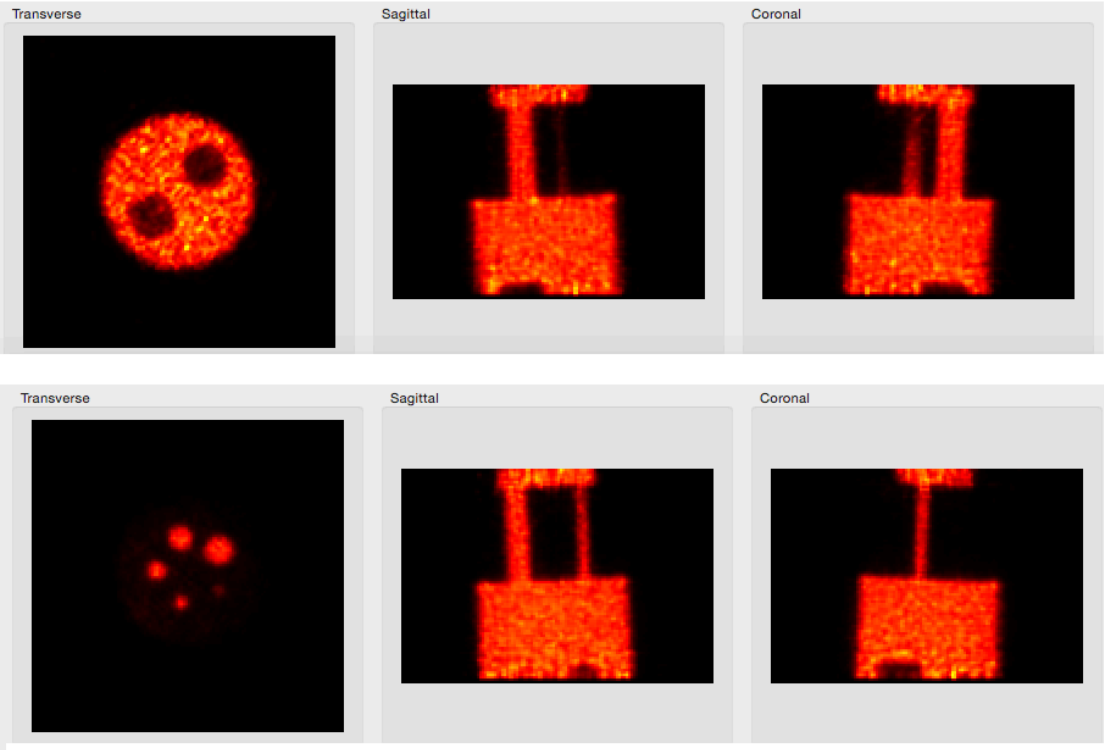

Figure.37 NEMA image quality phantom, 20 min data acquisition, list mmode reconstruction with 25 subsets and 10 iterations (the same as in other phantom or animal studies), the attenuation map was obtained from the PET image and SSS based scatter correction was applied.

The uniformity of the image was measured first. A 22.5 mm diameter by 10 mm long cylindrical region was drawn over the center of the uniform region of the image quality phantom. The average activity concentration was recorded as $Mean_{background}$, and the standard deviation was recorded as $STD_{background}$.

To calculate the recovery coefficients, the image slices covering the central 10 mm length of the rods were averaged to obtain a single image slice of lower noise. Circular ROIs were drawn around each rods in the image, with diameters twice the diameter of the corresponding rods. Then the transverse coordinates of the image pixels with the maximum value in each ROIs are recorded. The axial profiles were draw along the rods with these transverse coordinates. The recovery coefficient is defined as the ratio between the mean value along each axial profile and $Mean_{background}$.

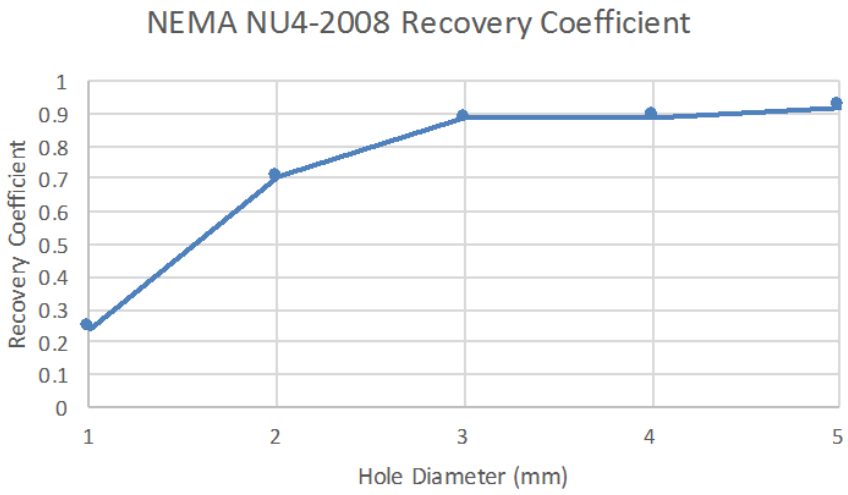

Figure.38 Recovery coefficient for each hole diameter

Recovery coefficient is among the best systems evaluated in [43].

4.2 Evaluation of PET-MRI interference

Different strengths of RF pulses were applied without gradient sequence, from 10 degree flip angle to 180 degree flip angle. No interference on PET from the MRI RF pulse was observed. Gradient sequence along would increase the background rate by about 10-20%, which can be considered insignificant for most applications. Initially, we observed a fact that the Ethernet communication between the scanner and the DAQ computer was not stable with strong gradient sequences. These two issues were solved later with a more stable ground connection.

Strong RF pickup was observed with our previous MRI PET insert systems using the same detector block technology. The major difference in this system is by using the highly integrated design, no physical cables transferring analog signals are used so the interference is avoided. Another difference is that the RF coil used is a commercial coil which is shielded and the distance between the coil and PET scanner is much greater than the previous systems.

On the MRI side, the main field (B0) homogeneity is evaluated with a uniform phantom filled with mineral oil (to avoid dielectric effect). Two gradient echo sequences with different echo time (TE) were used to generate B0 map: $\Delta B = \frac{P(TE1) - P(TE2)}{\gamma(TE1 - TE2)}$ in which ΔB indicates the magnetic field variations map, P() means the phase map, TE1 and TE2 are echo time of the two sequences, and γ represents the gyromagnetic ratio for ^{1}H protons. The B0 maps were acquired with and without the presence of the PET detector (on and off) inside the MRI FOV. There is minimum change after placing the PET detector inside the MRI but power off. While when the PET system is powered on, it induces a Z gradient on the B0 field. The difference field exhibits a Z gradient of about ±35 Hz. However, given the degree of linearity of the field, it can be shimmed out with active shimming.

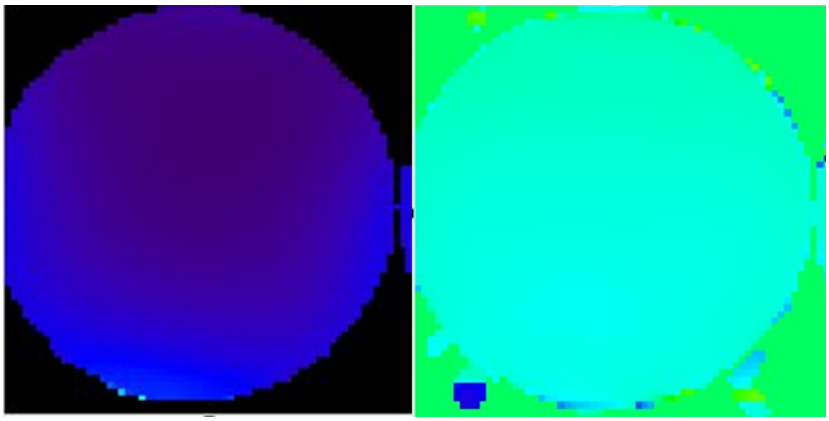

Figure.39 (left) B_0 map with PET on; (right) Difference between B_0 maps of PET on and off.

4.3 Image Studies

Derenzo phantoms were imaged first as proof of concept studies. Both hot and cold rod Derenzo phantoms were imaged and we had also conduced simultaneous PET-MRI image with the cold rod Derenzo phantom. Each phantom was filled with ~0.5 mCi ^{18}F-FDG and imaged for ~40 min. The MRI image was acquired with Spin Echo sequence with 5s TR and 17 ms TE. List mode reconstruction was used with 25 subset and 10 iterations without resolution model, which is our standard reconstruction routine for this system. Normalization and scatter correction (SSS) were applied.

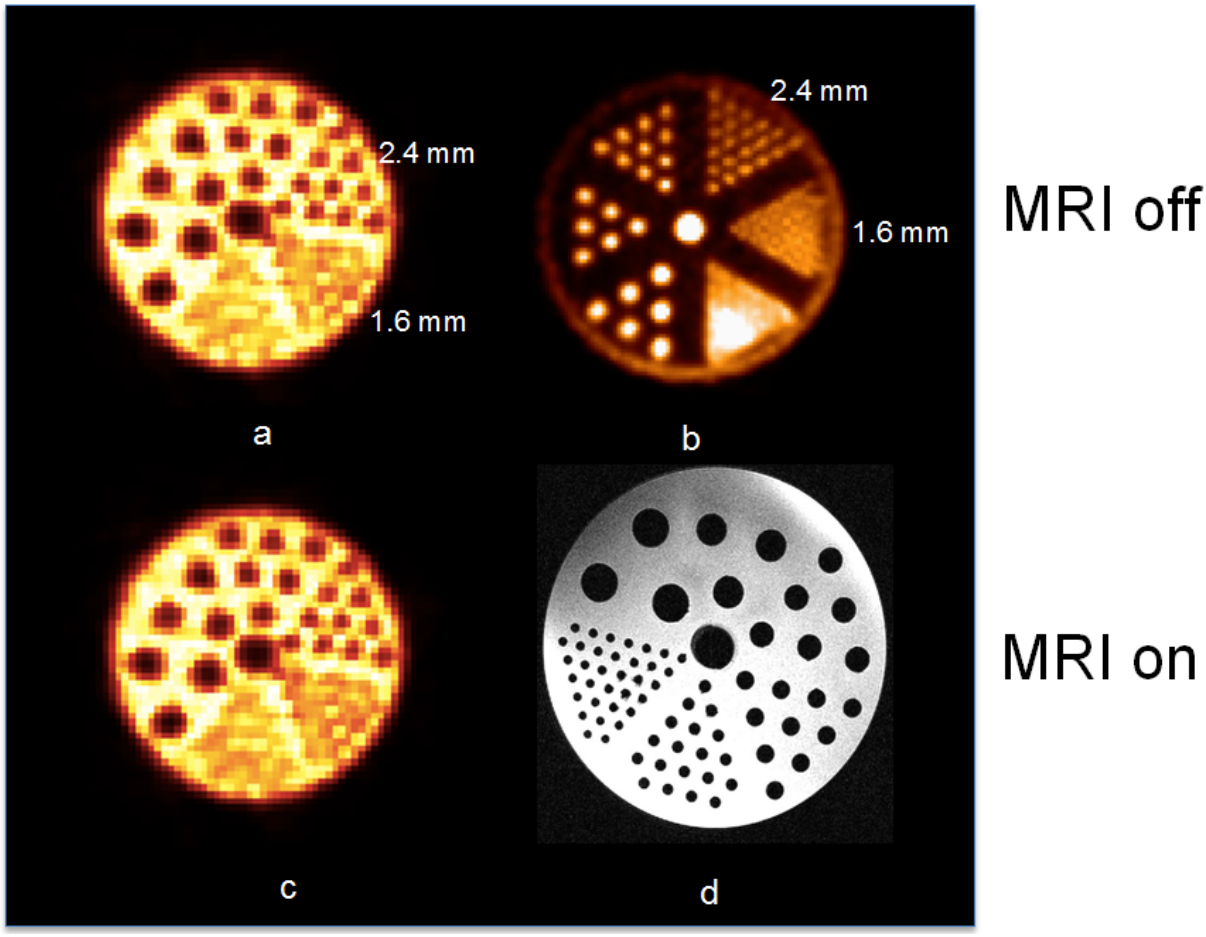

Figure.40. (a) Cold Derenzo phantom with MRI off; (b) hot Derenzo phantom with MRI off (c) Cold Derenzo phantom with MRI on; (d) MRI image with PET on

It can be seen that rod size of 2.4 mm can be clearly distinguished for both phantoms. There is no degradation on the PET side with MRI on and no distortions were observed on MR images due to the presence of the PET ring.

Initial simultaneous PET/MRI animal images were also generated with a rat injected with 1.2 mCi FDG. The head scan was ~10 min duration and stared ~1 hour after the injection, while the heart scan was ~50 min ling and started 2 hours after the injection.

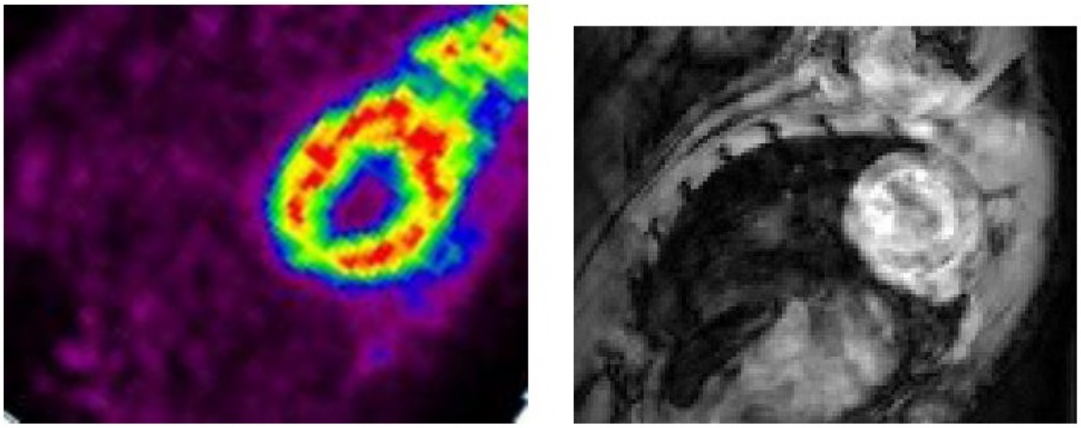

Figure.41 Simultaneous PET-MRI (Gradient Echo with 30 ms TR and 3.3 ms TE) images, no gating was used, ~50 million prompts collected for the PET image.

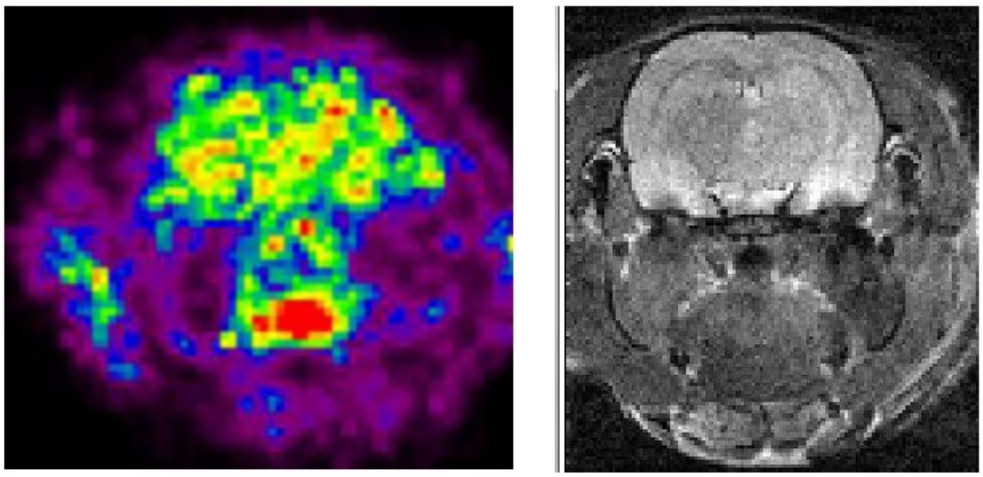

Figure.42 Simultaneous PET-MRI rat head image (T2 weighted Spin Echo), ~10 million prompts collected for the PET image.

Simultaneous PET-MRI images of a rat heart with ECG gating have also been obtained. The PET coincidences between two consecutive triggers are divided into 8 frames and each frame is summed with its corresponding frames between other triggers. Eventually 8 frames of raw data are reconstructed separately to form a series of dynamic images as shown below.

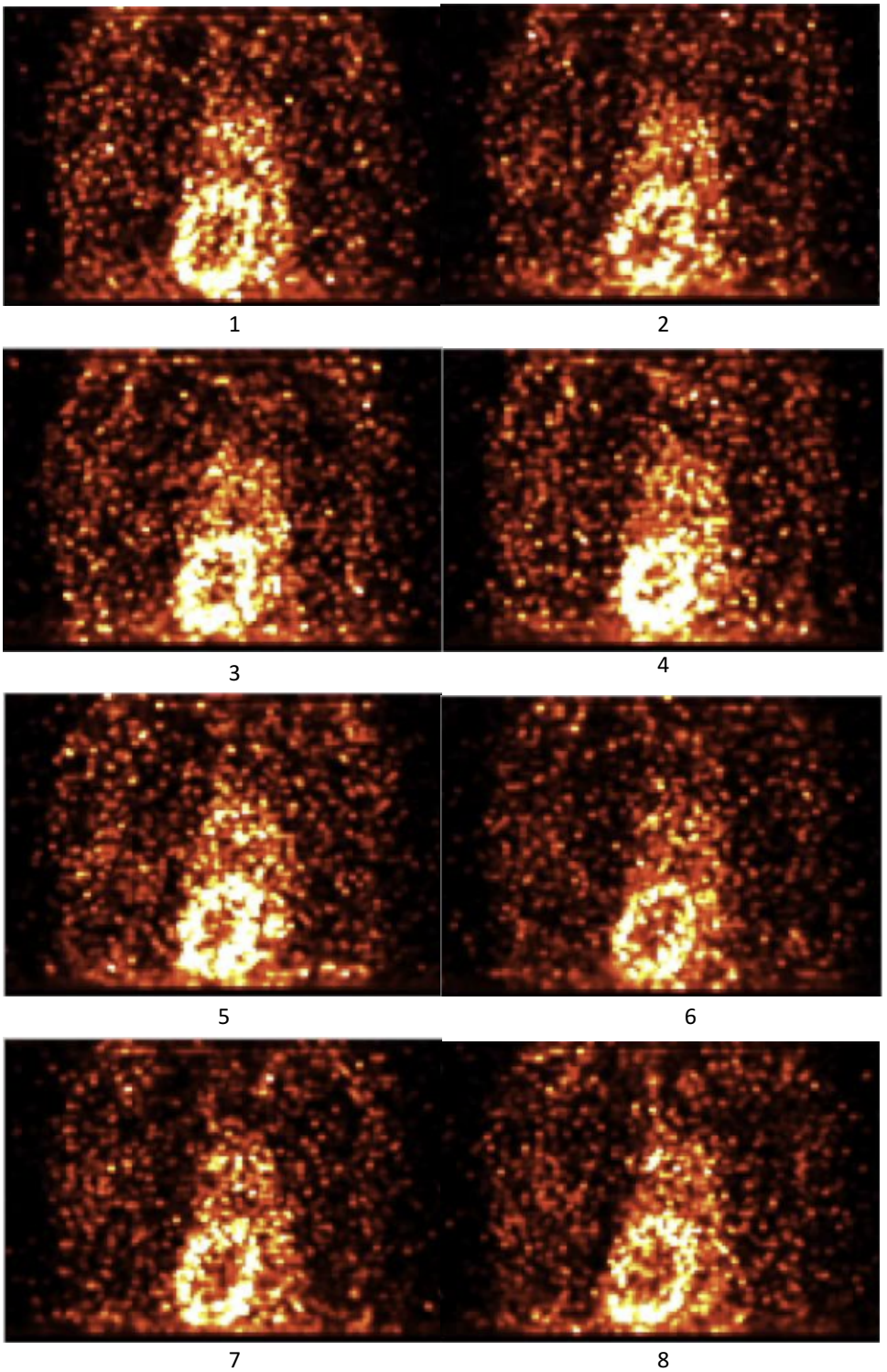

Figure.43 Dynamic rat heart images with ECG gating, index numbers are in time order.

The combined PET image and MRI image are shown below.

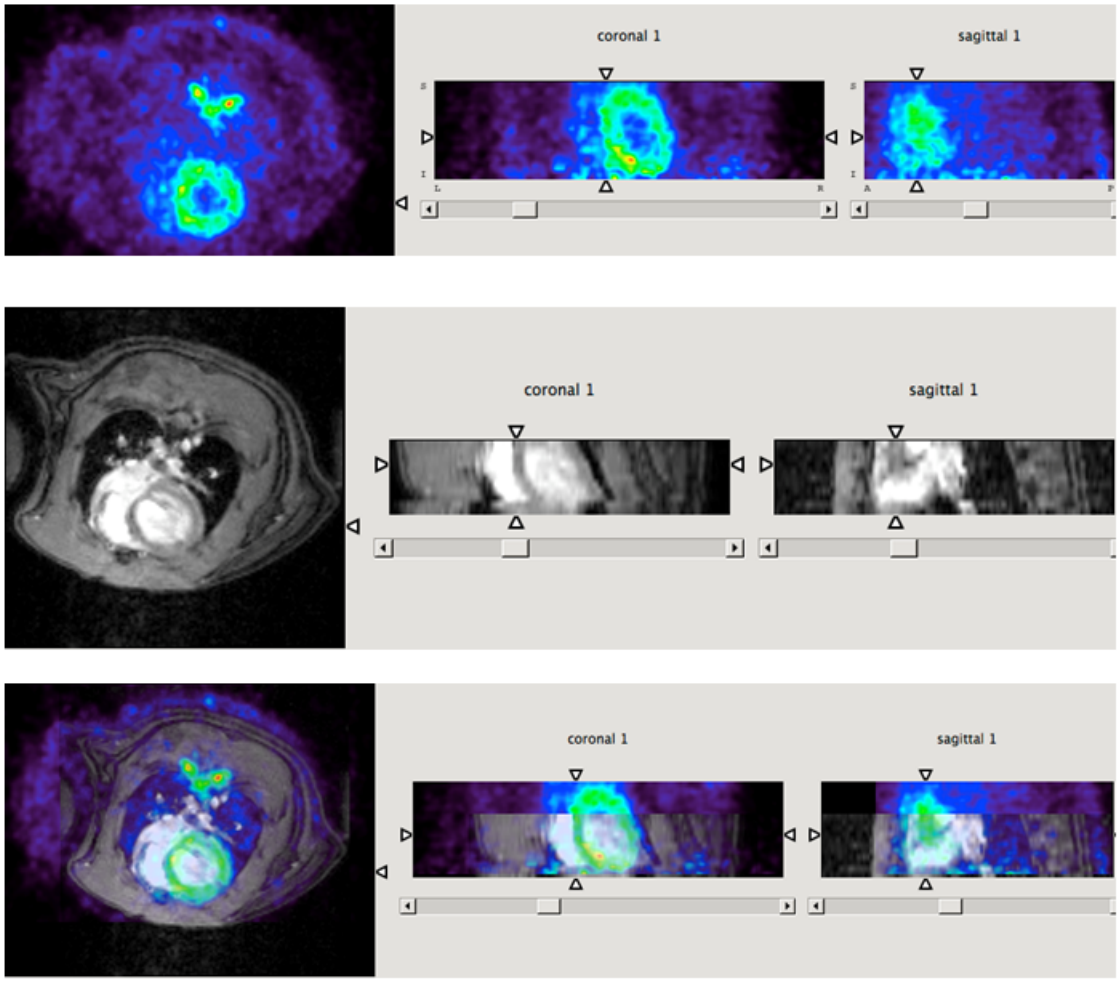

Figure.44 Combined PET and MRI images of the rat heart, MRI image was generated by a ECG gated fast gradient echo sequence using 60 degree flip angle.

4.4 Conclusions and Future Directions

In conclusion, a PET insert capable of working with a high field MRI system has been developed and tested. It is capable of conducing whole body rodent imaging with a highest performance 9.4 T MRI with commercial RF coil while only creating minimum to correctable distortions to the MRI system. The PET insert has state of the art animal PET performance with APDs. Beside applications for small animal imaging, it also has the potential of providing noninvasive input functions for PET/MRI brain scans and doing simultaneous breast PET/MRI

studies. This architecture is easily scalable so it can also be expanded to brain studies in the future.

Future Work

Software: On the software side, we are aiming to develop a whole package of reconstruction based on the open source software STIR. The major issue would be implementing a block based detector model with STIR. A simple modification would be adding a new "end-point" code in the "ProjMatrixByBinUsingRayTracing" class in the source code. However, it would require some careful thoughts to make STIR stable and flexible for different scanner geometries, such as a brain scanner in the future.

Hardware: On the hardware side, one of the major issue is that the SFP module used for communication contains ferromagnetic materials which is the primary source of main field distortion induced by the PET scanner. This problem is still manageable with the 9.4 T preclinical MRI system but will be a major obstacle for simultaneous breast PET/MRI applications in a clinical MRI, where shimming strength is limited. It may be due to the fact that the PET scanner axis is not aligned with the MRI axis but rather perpendicular to it for the breast imaging setup, so the asymmetry causes stronger distortion to the main field. Furthermore, the SFP module is under strong force when the gradient sequence is on which poses challenges to mechanical stability of the system. The best solution is certainly to replace the SFP modules with a different communication module containing only nonmagnetic materials. However, as far as we know there is no existing commercial product fulfilling this requirement. Another possible solution would be adding an adapt board to the mother board so the SFP module can be moved further away from the center of the FOV. Although this solution has other risks because the communication pathway between the mother board and SFP modules can induce unexpected interferences between two imaging systems.

Another potential improvement is the grounding of the PET system. Currently a 6 meter cable is used to connect power supplies and the PET scanner. Since there is about 10A current on this cable while the PET system is on, the ground is not solid enough and we had experienced communication issues with MRI gradient sequences. Also without proper shielding, the cable might transfer external noise to the inside of the MRI system. A better configuration might be

connecting the ground line of the cable to the ground plane of the MRI bore and adding a filter (could be as simple as a capacitor) to terminate the external noise on one side of the MRI bore.

Attenuation correction: We also need to explore the possibility of conducting MRI based PET attenuation correction. Initial study has been done on a rat body to create fat water contrast with Dixon sequence.

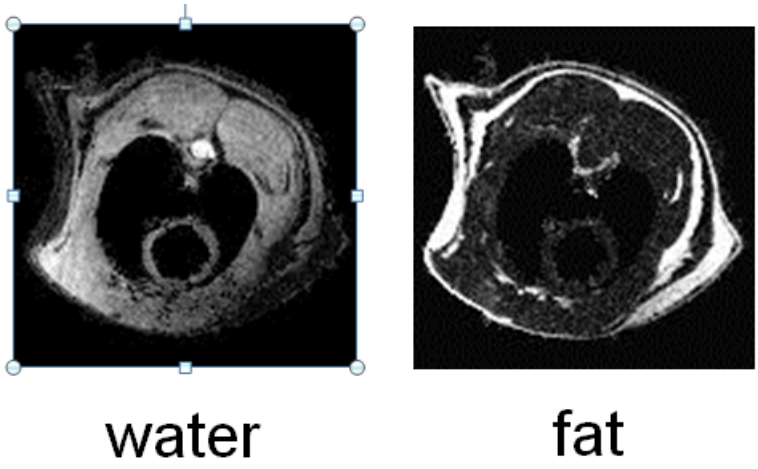

Figure.45 Water and fat images with Dixon sequence on a rat

Moreover, to achieve accurate quantification, it is also important to consider the attenuation effect from the RF coil. An attenuation map was reconstructed for the MRI rat body coil with a transmission scan [36] . It will be used to study the attenuation effect from the RF coil.

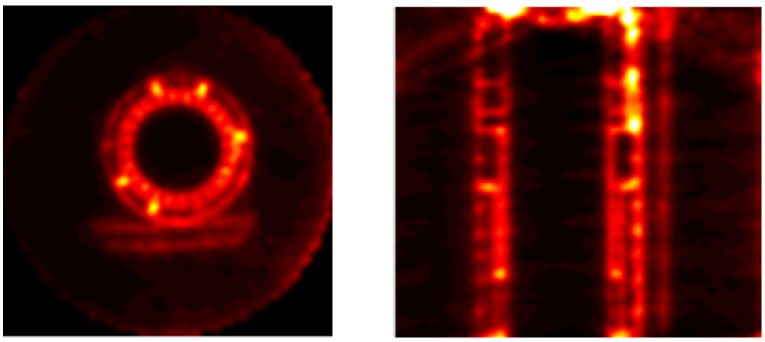

Figure.46 Attenuation mu-map of the RF rat body coil

To achieve accurate attenuation correction, accurate coregistration between the two systems is necessary. This requires the relative positioning information between the PET scanner, MRI field of view and the RF coil. A good setup needs to consider the workflow of practical animal studies thus it should also have a good animal handling system.

Data acquisition: Currently we are using 425 keV as the energy threshold for most scenarios. However, we might want to choose a lower threshold for certain applications such as the gated studies which is mainly limited by very low statistics. Moreover, we are currently using one threshold for all blocks. However due to the relatively large range of intrinsic gains of the crystal channels, by just adjusting ASIC gains may not be able to align peaks of all channels. Thus we would like to set different energy thresholds for different blocks in the future.

Another potential improvement with data acquisition is using a closed-loop system for temperature control. We usually consider the scanner temperature is stable after it reaches equilibrium, however the eddy current induced by the gradient sequences may affect the temperature. Furthermore, if the ambient temperature in the scanner room is drifting slowly, scans with a very long duration (such as normalization scan) may be affected.

Performance Evaluation with MRI on: Some of the NEMA measurements need to be conducted with MRI on. A good start would be a NECR test, which is a very good indication of the system performance change.

Chapter 5 GEM Tracking Detector for Imaging Positrons

Most of this chapter has been excerpted from my publication entitled "A Study of a GEM Tracking Detector for Imaging Positrons from PET Radioisotopes in Plants" by T. Cao, B. Azmoun, B. Babst, M. Blatnik, M. L. Purschke, S. Stoll, P. Vaska, and C. Woody, IEEE TNS 2014[80].

5.1 Introduction

Besides applications on animals and humans, PET has also been used in the area of plant science at Brookhaven National Laboratory[80]. Positron emitting isotopes were actually used to study photosynthesis in plants long before they were used in medical and preclinical applications [81]. Today, the use of Positron Emission Tomography (PET) to study plant biology is gaining more and more interest to elucidate physiological mechanisms [82-84]and develop new types of plants for biofuels and renewable food supplies. The goal of plant research at Brookhaven National Laboratory was to provide basic biological information about plant adaptation to changing environmental conditions, which are needed to develop crops dedicated for bioenergy - crops that grow larger and faster, can be converted into fuel efficiently, and can grow vigorously in less-than-ideal locations to avoid competition for prime agricultural land that is used to produce food and fuel. Positron emitting isotopes are used in both radio-metabolite assays and PET imaging to observe and quantify how biochemical materials are distributed throughout various types of plants that are being developed for these purposes[85-87].

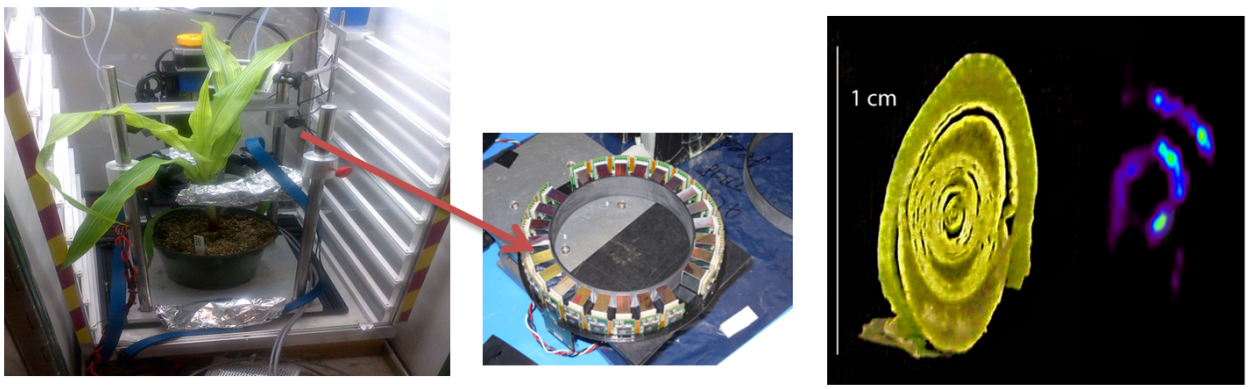

Figure.47 BNL plant PET system and PET image on corn stem (with phosphor plate image as comparison)

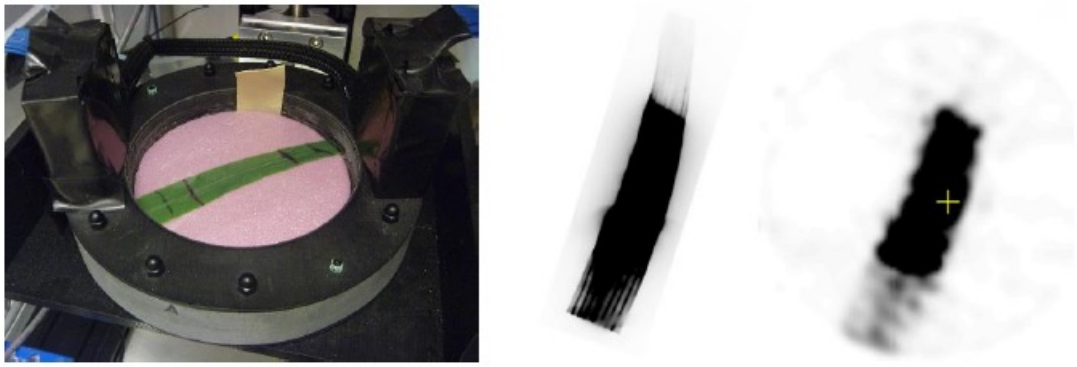

Figure.48 (left) A corn leaf which was cut one hour after ^{11}C-carbon dioxide uptake. (Center) A radiographic image of this leaf. (Right) a PET image taken with the BNL-plant scanner[88](©2013 IEEE)

However, adapting PET imaging techniques from clinical or preclinical uses to plant imaging poses some new challenges. In particular, the leaves of most plants are very thin and a large fraction of the positrons emitted from PET isotopes can escape from the object without annihilation. The escape fraction for ^{18}F could be as high as 60% and the proportion of escaping positrons varies for different regions of the sample, which could further limit the quantification accuracy of PET in this application [89]. As an example, Fig. 49 shows a Monte Carlo simulation and experimental data from a disk of F-18 solution of various thicknesses that is open to air on top, with a plastic plate above it to stop the escaped positrons. The escape fraction is calculated by the number of positrons that annihilated in the plate divided by the total number of positrons in the sample. In the experimental data, these values were measured from separate regions in a PET image taken in a microPET R4 scanner. Therefore, devising a method to detect these escaping positions could increase the efficiency and hence the sensitivity for obtaining PET images of plants, or provide a completely alternate means of producing such an image.

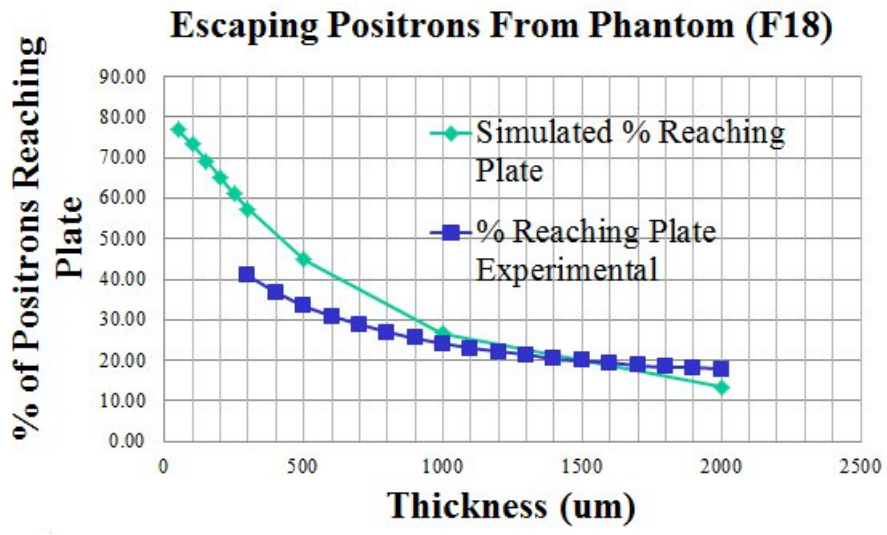

Figure.49 Simulation and experimental results of the positron escaping effect

Measuring the escaping positrons can also improve the ability to determine the actual tracer concentration in thin objects of varying thickness such as plant leaves, and therefore improve the quantitation accuracy of PET in these applications. This is because the conversion efficiency for producing 511 keV gammas with PET varies within the object (e.g., between the vasculature and the photosynthetic tissue), and measuring the non-converting positrons can be used to correct for the variable loss of signal in the PET image.

Systems for direct positron imaging have previously been discussed[90], and recently, PET compatible positron imagers are also under development. One group has proposed a direct positron imaging method consisting of a PET detector, comprised of an array of LSO crystals and a Position Sensitive PMT (PSPMT), combined with a thin plastic scintillator in front to detect both positrons and gamma rays from positron emitting isotopes [91].The positrons and gamma rays are differentiated based on their signal shapes from the two detectors. Another group at Jefferson Lab has proposed a similar beta detecting system called the PhytoBeta imager [92]. Their detector is also based on detecting positrons using a thin plastic scintillator read out with a PSPMT.

One drawback for all the detectors developed so far is that the object being imaged must be placed in direct contact with the detector surface and only a planar image can be obtained. Having the detector in close proximity to a plant leaf can cause a significant perturbation on the

normal metabolism of the plant because the detector blocks the light and airflow. This can be particularly important when doing real time dynamic studies. It is therefore preferable to place the detector some distance from the plant surface, which requires additional information about the direction of the emitted positron in order to produce a faithful image of their original distribution on the surface.

We have studied this problem using a Gas Electron Multiplier (GEM) detector[93] as a means to directly detect and measure the position and angle of the emitted positrons. We performed an initial investigation of this technique to track positrons in the sub-MeV energy range that are emitted by PET isotopes and used the track information to obtain images of various types of phantoms as well as actual leaf specimens. These results, along with a comparison to Monte Carlo simulations of the detector performance, are presented below.

5.2 Methods

5.2.1 Detector System

Gaseous detectors are widely used in nuclear and particle physics because of their high sensitivity to charged particles. We have used a gaseous drift detector consisting of a triple GEM configuration with a short (16.3 mm) drift region above the GEM stack to collect the ionization from positrons passing through the gas. A schematic representation of the detector is shown in Fig. 50. The charge produced by the incident positron is drifted from top to bottom in an electrical field and amplified by the triple GEM and collected on a set of readout electrodes below the bottom GEM. The geometry and segmentation of these readout electrodes largely determines the achievable position resolution in the transverse readout plane. The coordinate in the drift direction is determined by measuring the drift time for the arrival of the charge on each electrode. The charge measured on each readout electrode is subject to statistical fluctuations in the formation of the primary charge clusters, and in the diffusion process in both the drift and amplification regions. The signals are processed through a preamp-shaper combination and then sampled with a multi-channel flash ADC. The data is processed offline to reconstruct the original track and a planar image is formed by extrapolating each track back to the object plane.

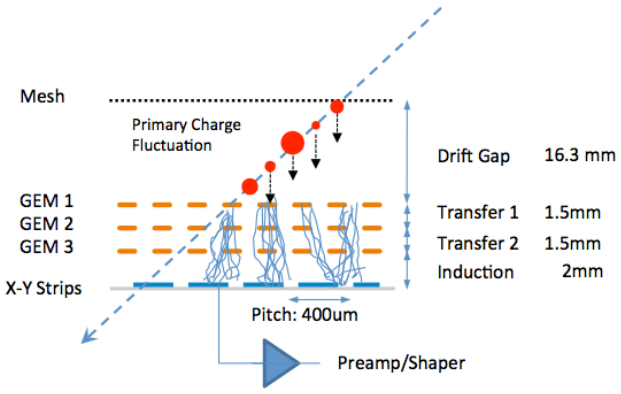

Fig.50 Triple GEM detector with a drift region above to collect the ionization from the incident positron and an XY strip readout below.

Fig. 51 shows a photo of the actual setup. Ar/CO2 (70/30) was used as the detector gas, which has a drift velocity of ~3 cm/μsec at a drift field of ~1 kV/cm, and corresponds to a drift time of ~550 ns for a 16.3 mm drift gap. The detector has a thin 25 μm mylar entrance window to minimize the effect of multiple scattering. The detector consists of a stack of three 10 x 10 cm GEM foils with XY strip readout plane similar to that used by the COMPASS experiment [94]. Both the X and Y strips have a pitch of 400 μm, but the Y-strips have a width of 90 μm, and the X strips, which sit below the Y strips, have a width of 350 μm. This is done to provide more equal charge sharing between the two views. The voltage across each GEM was approximately 400 V, resulting in a gain ~8.5x103 that provided a good signal to noise ratio.

The data acquisition system consists of a CERN Scalable Readout System (SRS) [95] which utilizes the APV-25 chip that has a sampling rate of 40 MHz. The peaking time of the preamp is ~100 ns and 28 time samples were collected for each event. The start time for measuring the drift time for each strip was provided by a common signal off the bottom of the bottom GEM. Due to variations in the arrival time of the first charge clusters that exceed our electronic trigger threshold (10 mV), this led to a resolution in measuring the drift time of ~60 ns, which corresponds to a resolution of ~1.8 mm in determining the spatial coordinate in the drift direction. The SRS system is read out through Ethernet by a PC using the RCDAQ software [96]. The maximum event rate for acquiring data was determined by the number of samples read out form the APV-25 chips and was limited to ~1 KHz. The fundamental limitation of event rate is determined by the electron drift time in the gas and can be as high as 1 MHz, which could be approached by using a faster data acquisition system.

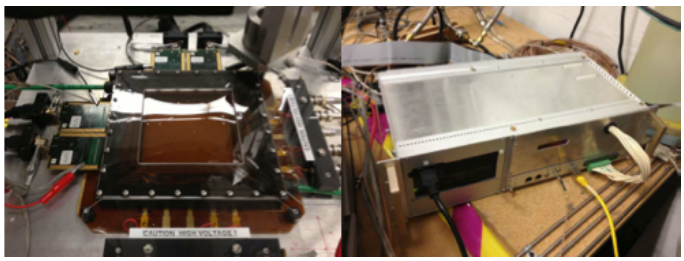

Fig. 51 Detector with APV-25 readout cards (left) and SRS system (right)

5.2.2 Simulations

A Monte Carlo simulation was developed to estimate the position resolution which could be obtained by simulating charged particles emitted from a source and reconstructing their tracks using such a gas detector. The program simulates the energy deposit due to ionization in the gas, the drift of the primary charge through the drift region, including longitudinal and transverse diffusion, the amplification process in the GEM stack (including additional diffusion), the deposition of the amplified charge on the readout electrodes, and the development of the signal pulse and shaping time in the readout electronics. Of particular importance are the fluctuations in the energy loss along the track, which results in charge clusters of widely varying magnitude. As these clusters drift in to the amplification region, diffusion causes spreading of the charge in both the longitudinal and transverse directions, thereby causing dispersion in both the position and time information carried by these clusters, which affects the resolution for determining the direction of track.

In addition to diffusion and cluster size fluctuations, multiple scattering is also an important factor that limits the resolution. Gaseous micro pattern detectors are typically used to detect high energy particles, which produce straight tracks within the detector (in the absence of a magnetic field). However, electrons and positrons with energy below 1 MeV may suffer from large multiple Coulomb scattering along the path of the particle through the detector, resulting in tracks that deviate significantly from a straight line.

A second Monte Carlo simulation, based on GEANT4 [97], was also developed that allowed us to study the amount of multiple scattering in the detector setup and determine its effect on the position and angular resolution for measuring low energy positrons in our detector.

5.2.3 High Energy Beam Test

The intrinsic performance of the GEM detector was studied in a high energy beam test at CERN with a well collimated beam of 120 GeV/c pions. The position and angular resolution of the detector was measured at different incident beam angles using a separate set of four micromegas detectors as a beam telescope [17]. The micromegas were able to measure the angle of the beam track to ~50 microradians, which was used to project the track to the GEM detector located ~2 m away. This resulted in an extrapolation error of ~100 μm when measuring the position resolution of the GEM detector, but contributed negligibly to the measured angular resolution.

5.2.4 Phantom Tests

Three different phantoms, shown in Fig. 52, were used to study the performance of the GEM detector for measuring low energy positrons. All of the phantoms had through holes that were sealed with a 25 μm kapton window at one end. One phantom had a single 10 mm diameter hole and the other two had two holes: one with 2 mm diameter holes and 6 mm hole-to-hole separation, and the other with 3 mm diameter holes and 10 mm hole-to-hole separation. The holes were filled with a solution of FDG containing 18F which produces positrons with an average energy of 250 keV and a maximum energy of 634 keV. For measuring the position resolution of the GEM, the phantoms were placed directly on top of the entrance window of the detector.

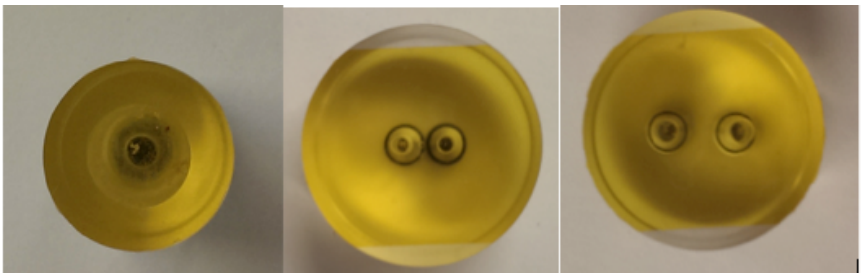

Fig.52 Three phantoms used for detector studies: Left: 10 mm cylindrical hole, Middle: 2 mm holes separated by 6 mm Right: 3 mm holes separated by 10 mm. Yellow surface is 25 micron thick kapton window.

5.2.5 Leaf Imaging

Pea leaf:

Figure 53 illustrates the setup for imaging a pea leaf. The selected pea leaf containing two leaflets was exposed to a 30 second pulse of [^{11}C]CO2 in continuous stream of air flowing at 200 mL/min. The leaf was illuminated with red and blue LED light to allow it to assimilate the ^{11}C by photosynthesis and then incubated for twenty minutes to allow the tracer to be distributed within the leaf. The leaves were then cut from the plant and sealed in a lucite container having a 25 μm thick mylar window. This container was then placed directly on top of the GEM detector. The total activity of the leaf was ~0.1 mCi at the beginning of the imaging study. A radiography with 1 minute exposure was conducted followed by a GEM imaging with 20 minutes exposure.

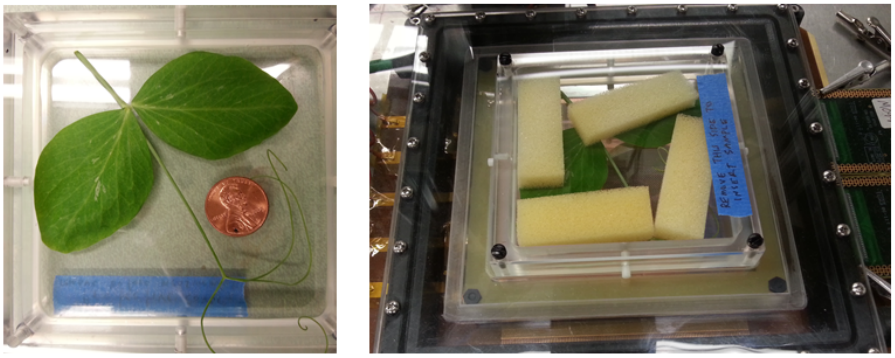

Fig. 53 Pea leaf inside the lucite container. Soft foam was used on the back side of the leaf to keep it flat.

Poplar leaf:

Fig.54 illustrates the setup for imaging a poplar leaf. The poplar leaf was selected and its petiole was immersed into a solution of [^{18}F]fluoride and exposed to natural light, allowing the fluoride to move with the bulk flow of water up through the veins and into the leaf. After ~1 hour uptake, a phosphor plate radiograph was taken of the leaf with a 15 second exposure and then scanned in a MicroPET R4 scanner with a 20 minute exposure. The leaf was then sealed into the same lucite container as used for the pea leaf and imaged by the GEM detector with direct contact. The activity in the poplar leaf was estimated as ~25 μCi using the GEM trigger rate. Data was collected with the GEM detector over a 4 hour period and produced approximately 15 million events that were used in the subsequent image reconstruction. The long imaging time was required due to the count rate limitation in the data acquisition electronics.

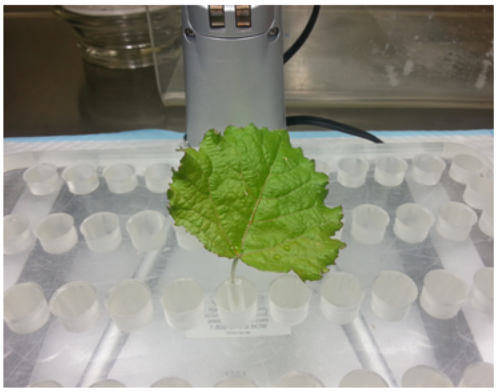

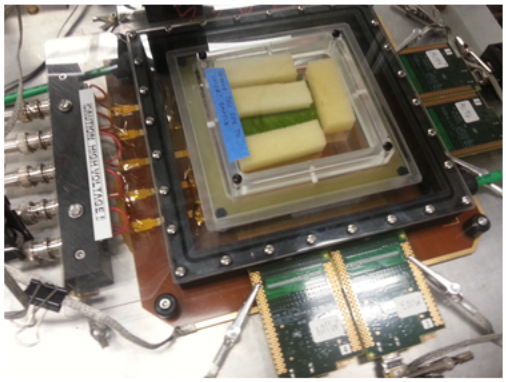

Fig. 54 Left: Petiole of the leaf was immersed into a ^{18}FDG solution for uptake. Right: Poplar leaf inside the lucite container.

5.3 Results

5.3.1 Simulation Results

Figure 55 shows the results from the stand alone Monte Carlo showing the expected error on the extrapolated position of the track at the entrance window of the detector and the error on the angle of track as a function of angle measured relative to the normal to the window. At larger angles (>10 degrees), the error on the position is on the order of a hundred microns and the error on the track angle is less than 10 mrad. However, for small angles, both the position and angular resolution become much worse due to the fact that it is very difficult to measure the track angle, since all of the charge from the track is collected on just a few strips. In this region, there is no precise angle measurement and it is better just to use a simple weighted average of the charge distribution to determine a centroid and measure only the track position.

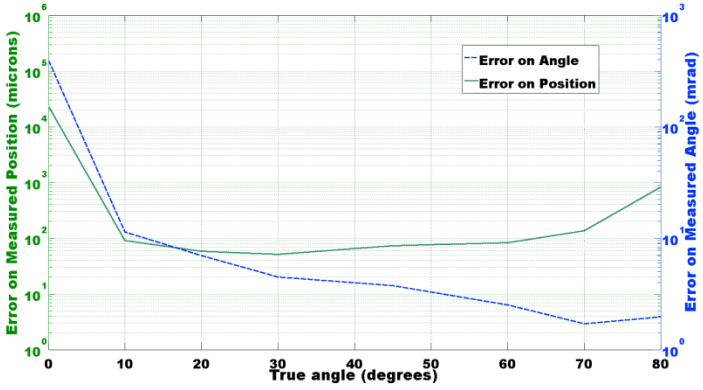

Fig. 55. Monte Carlo simulation of the error on the reconstructed position (left) and the measured angle (right) versus the true angle of incidence for a detector with a 16.3 mm drift gap and readout electrodes with 0.4 mm pitch

The Geant4 simulation was used to study the effect of multiple scattering in the detector. In this simulation, a point source was positioned directly on the window and the contribution to the position resolution due to multiple scattering from the window and the gas was determined. Figure 57 shows how the spatial resolution is affected by multiple scattering as a function of incident angle. It is clear that the resolution depends strongly on the energy of the incident particle, and that particles with lower energy suffer more from multiple scattering. The average energy of positrons emitted by ^{18}F is 250 keV, but their average energy after passing though the leaf and the detector window is only ~220 keV when they enter the drift region. The resolution (sigma) varies from 0.6 mm at normal incidence to ~1.7 mm at 70 degrees incidence. The resolution gets worse at larger angles due to the longer path length. Note that the multiple scattering in the window does not directly affect the extrapolated position resolution when the source is placed directly in contact with the window. However, Fig. 58 shows the simulation result when a point source of 250 keV or 500 keV positrons is positioned 1 cm above the window. In this case, the multiple scattering in the window significantly degrades the spatial resolution due to the error introduced in the extrapolation of the reconstructed track.

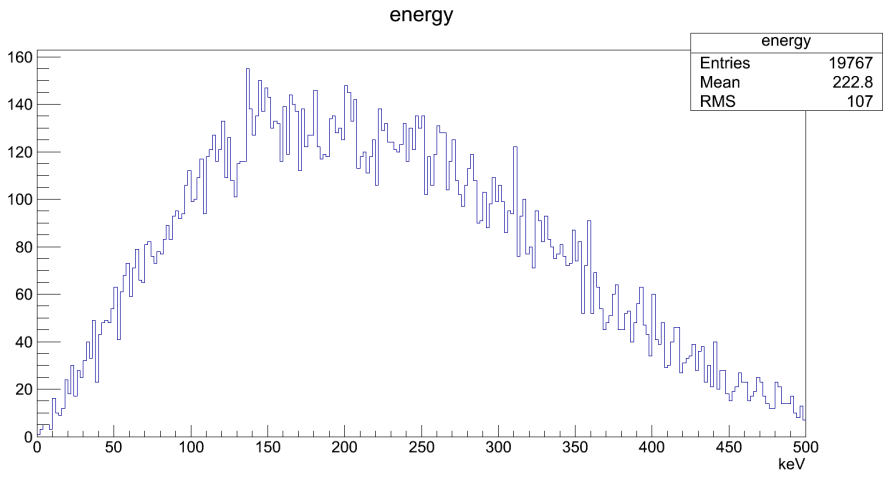

Figure.56 Energy spectrum of F-18 positron entering the detector, simulated by Geant4, the thickness of the leaf is set to be 500 um.

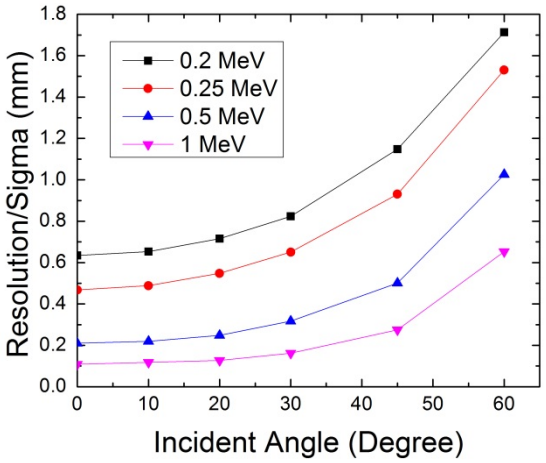

Fig.57 Geant4 simulation of the spatial resolution (sigma) versus angle of incidence for particles with different energies with a point source positioned directly on the window.

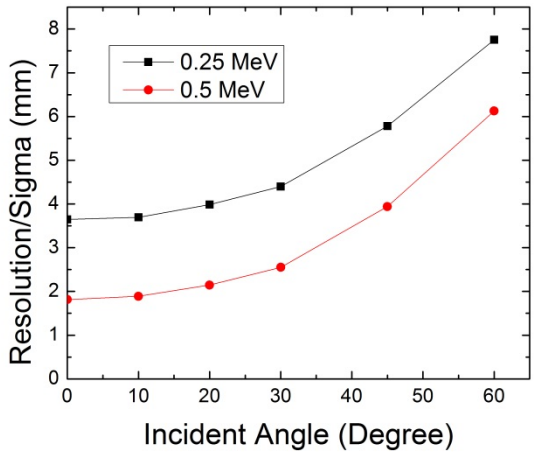

Fig.58 Spatial resolution versus angle of incidence for point sources with positron energies of 250 keV and 500 keV positioned 1 cm away from the 25 μm mylar window.

5.3.2 Track Reconstruction

Figure 59 illustrates the procedures used to measure tracks with the detector. Fig. 60a shows the raw waveforms on the X-strips for a single event. The shift in the peaking time towards later times clearly shows the effect of an inclined track. Fig. 60b shows the digitization of a single strip as a function of time. The arrival time of the charge on a given pad is determined by fitting the rising edge of the pulse and extrapolating it to a point on the time axis. From the time information, the vertical position of the electron clusters above each pad can be calculated and the trajectory of the track in both the XZ and YZ planes can be calculated (Z being along the

drift direction). An example of a track fit in the XZ plane is shown in Fig. 60c. The reconstructed track vector is then used to extrapolate back to the image plane to form a two dimensional image.

When reconstructing low energy positrons, in addition to multiple scattering, one has to also deal with the effects of background and noise, including events with large scattering angle, pile up events and electronics noise. Therefore, several event selection and track quality cuts were applied. A threshold cut was used to reduce noise and background, and the signals on the pads were required to have a reasonable shape. A minimum number of good pads was required to form a track and a reduced chi-square was also used to test the goodness of fit. This event selection method could potentially induce bias to the quantification result since it has different sensitivity to positrons with different energy. However, a Geant4 simulation result shows that the difference between the mean energies of F-18 positrons passing through 0.1 mm and 0.5 mm water is less than 5%, which means the bias is insignificant.

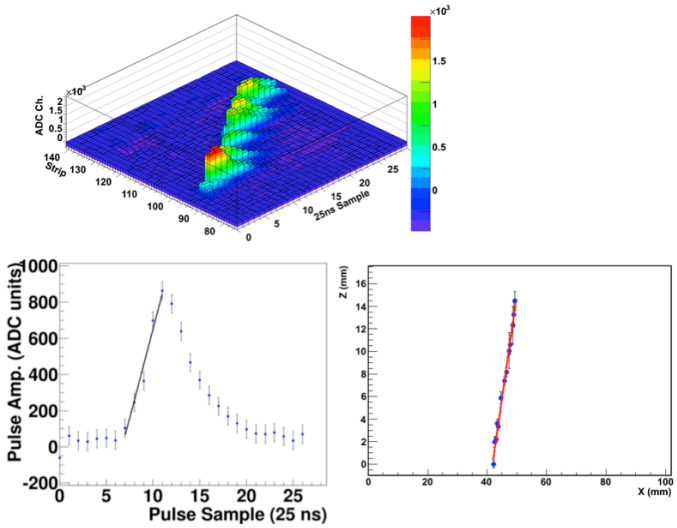

Fig. 59 a) Raw waveforms for all x-strips b) Fit to the rising edge of the pulse to give timing information c) An example of a reconstructed track in the x-z plane

Figure 60 shows the distribution of reconstructed angles obtained from the vector fitting procedure using the 10 mm cylindrical phantom. The dip around zero degrees is due to the fact that it is not possible to accurately determine a vector for small incident angles. Therefore, for tracks near zero degrees, if it was not possible to fit a vector in a particular view (X and/or Y), a simple centroid was used to determine the track position at the readout place, which was then assumed to correspond to the same position of the track at the image plane. The peaks at large

angles near 90 degrees are due to noise that was not eliminated by the cuts and were not used in any final image reconstruction. When forming images in the studies shown below, only reconstructed track vectors between 30 and 80 degrees were used, and only the centroid values were used for tracks at smaller angles.

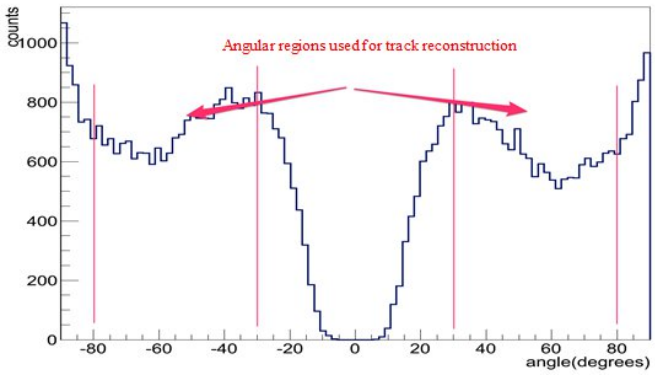

Fig. 60 Distribution of angles of reconstructed tracks from the 10 mm cylindrical phantom data.

5.3.3 High Energy Beam test

Figure 62 shows the position resolution (averaged for X and Y) and the angular resolution of the detector measured at different angles in the CERN beam test. The contribution to the position resolution resulting from the projection of the track measured in the micromegas (~100 μm) has been unfolded from each of the data points. For angles greater than 10 degrees, the position resolution is in the range of 100-200 μm. The position resolution computed in the Monte Carlo (Fig. 55) is somewhat better than what was measured in the test beam and continues to improve with increasing angle, presumably because the effects of noise and multiple scattering were not included in the Monte Carlo model. The angular resolution for the GEM was measured to be ~10 mrad for angles above 10 degrees and agrees reasonably well with the Monte Carlo. Moreover, since the position is determined by extrapolating the reconstructed track to a known plane, the angular error would be magnified due to a longer distance at larger angles. Thus both results show the position resolution increasing with the incident angle. And also the signal on each pad would be weaker for larger angle tracks since the signal is spread over more pads, which would degrade the signal to noise ratio and potentially also degrade the resolution

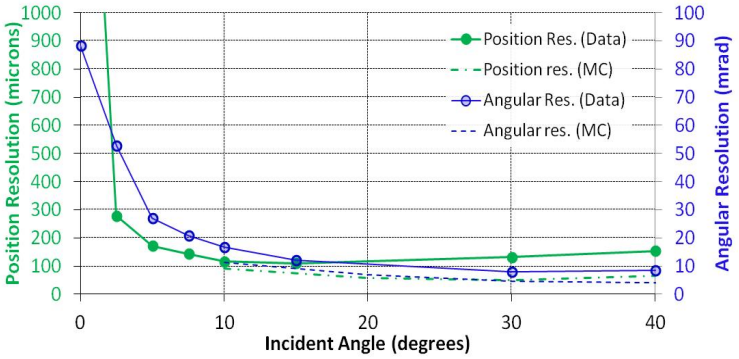

Fig.61 Position resolution (left) and angular resolution (right) of the GEM detector versus angle measured in the CERN beam test. Results from Monte Carlo simulation are shown here again with dash lines.

5.3.4 Phantom Tests

Figure 62 shows the reconstructed images of the two double hole phantoms containing the solution of FDG. The two holes are clearly resolved in both cases. For the image with the 2 mm holes on the right, the concentration of the tracer in the two holes was not equal due to difficulty in filling the small holes, so the peaks are not of the same intensity. For the 3 mm holes on the left, the FWHM of each peak is contained within a diameter of 4.2 mm, which gives measure of the spatial resolution of the reconstructed images.

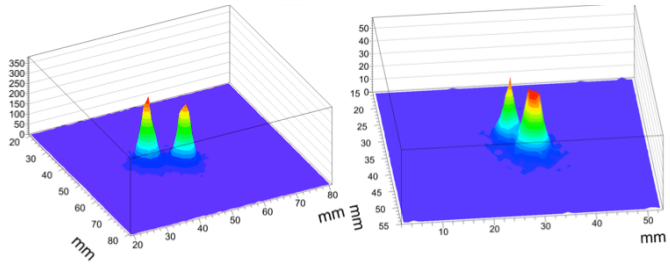

Fig.62 Two hole phantom images. Left: 3 mm holes with 10 mm separation. Right: 2 mm holes with 6 mm separation.

The efficiency of the detector was measured using the phantom with the 10 mm hole. From the raw trigger rate, the sensitivity was determined to be 0.3 counts per second per nCi/cc concentration of ^{18}F in the phantom. Approximately 35% of these triggers were selected by the reconstruction algorithm to form the final image. If one defines an active volume by assuming a 200 micron leaf thickness, the sensitivity can be expressed as a percentage of total decays, which

we find to be 3.1%. This can be compared to a similar value for a point source for the MicroPET of 1.9%.

5.3.5 Leaf Imaging

1) Pea leaf

Figure 63 on the left shows the GEM image for the pea leaf after its uptake of [^{11}C]CO2. On the right is a radiograph of the same leaf for comparison taken 20 minutes after administration of the radioactive tracer.

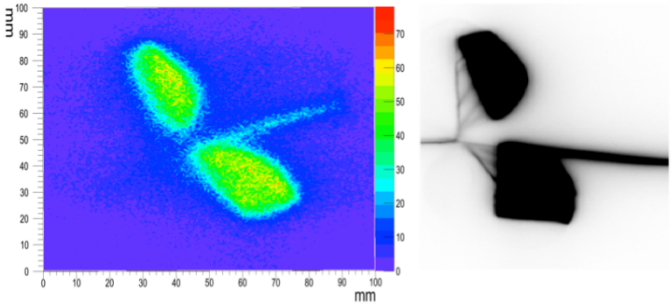

Fig. 63 Left: Image of a pea leaf taken with the GEM detector. Right: Radiograph of the same leaf.

2) Poplar leaf

Figure 64 shows a series of images of the poplar leaf. Figure 64(a) shows the radiograph which gives an indication of the actual tracer distribution after the initial uptake. Figure 64(b) shows the image obtained with the GEM detector. One can see a correlation with the activity in the upper right hand quadrant of the leaf, although the detailed vein structure is not observed due to the lower resolution and the possibility that the tracer distribution changed during the relatively long imaging period. Figure 64(c) shows the image from the MicroPET scanner at its nominal resolution (~2 mm) taken shortly after the initial uptake. The tip of the petiole that was immersed in the tracer solution can be seen as an area of high activity and the vein structure is more apparent. Figure 64 (d) shows the same MicroPET image blurred to a resolution of 4 mm (FWHM), similar to the resolution of the GEM detector. The vein structure is still apparent, indicating that the blurring of the GEM image may be more due to redistribution of the tracer from the veins out to other parts of the leaf.

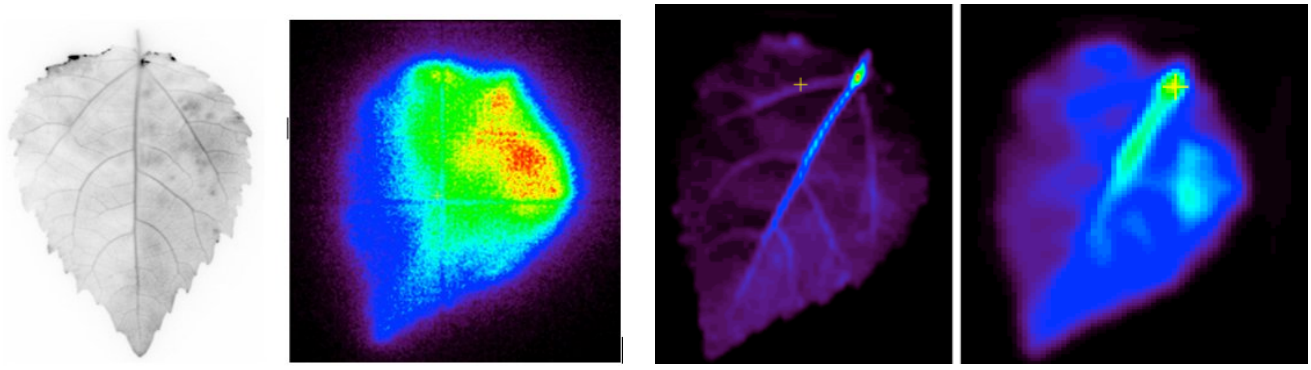

Fig.64 Images of the poplar leaf after administration of 18F fluoride: (a) radiograph with 15 seconds exposure taken after the initial uptake (b) GEM detector image (c) MicroPET image, 20 minute scan after initial uptake at nominal resolution (d) Same MicroPET image blurred to 4 mm resolution

5.4 Discussion

The main purpose of this study was to investigate the possibility to image objects containing positron emitting isotopes using a GEM tracking detector. These types of detectors have very small stopping power for 511 keV gamma rays, and they could therefore potentially be used with PET imagers simultaneously. Gas tracking detectors are ideally suited for measuring charged particles due to their high efficiency and low mass, and are extensively used in high energy particle physics applications. However, it is much more challenging to measure low energy positrons, such as those emitted by PET isotopes, due to a number of fundamental limitations. These include multiple scattering and energy loss in the object being imaged and in the detector itself. Interactions in the object limit the ability to image the object only at its surface, which makes this type of detector better suited for imaging thin objects, such as leaves. However, interactions in the detector and surrounding material affect the position and angular resolution that can be achieved. We believe that this is the most important limitation overcome in order to be able to image thin objects, especially when they are not in direct contact with the detector.

It was shown that with high energy particles the mini-drift GEM detector is capable of achieving a position resolution in the range of 100-200 μm and an angular resolution <10 mrad when the effects of multiple scattering are negligible. However, the energy of the positrons from typical PET isotopes is in the few hundred keV range, where the energy loss and multiple scattering in the detector window and gas become significant. This can be seen in Fig. 57, which

shows that for positrons with an energy of 200 keV, corresponding to roughly the average energy of the positrons from ^{18}F decay after passing through the leaf and the detector window, the multiple scattering in the gas results in a spread in the position resolution to more than 1 mm RMS at an incident angle of zero degrees, and almost 2 mm RMS at 60 degrees. For tracks in the angular range that we use for image reconstruction (30-80 degrees), this contributes ~4 mm FWHM to our image resolution, as can be seen in the phantom image in Fig. 62, and in the leaf image in Fig. 64. This, along with the resolution in the ability to measure the drift time using a common signal from the GEM with a finite threshold, are the dominant contributions to the final image resolution in this application, and not the intrinsic detector resolution.

The effect of multiple scattering in the gas can possibly be reduced by using a lower Z gas, such as helium or ethane, and/or reducing the drift gap, which are possibilities we wish to explore in the future. Multiple scattering in the detector window does not directly affect the position resolution of the reconstructed image when the object is placed directly on the window, but, as shown in Fig. 58, it does degrade the resolution when the object is placed some distance from the window. The effect can illustrated by the figure below. This is because any scattering in the window will change the direction of the positron before entering the detector and therefore result in measuring an incorrect angle for the track pointing back to the object. The error on the projected position also gets worse with increasing distance of the object from the detector and quickly degrades the image quality. It would therefore be highly desirable to reduce the thickness of the window, or to eliminate the window completely. It may be possible to reduce the window thickness to ~10 μm , depending on the size of the detector and the operating pressure.

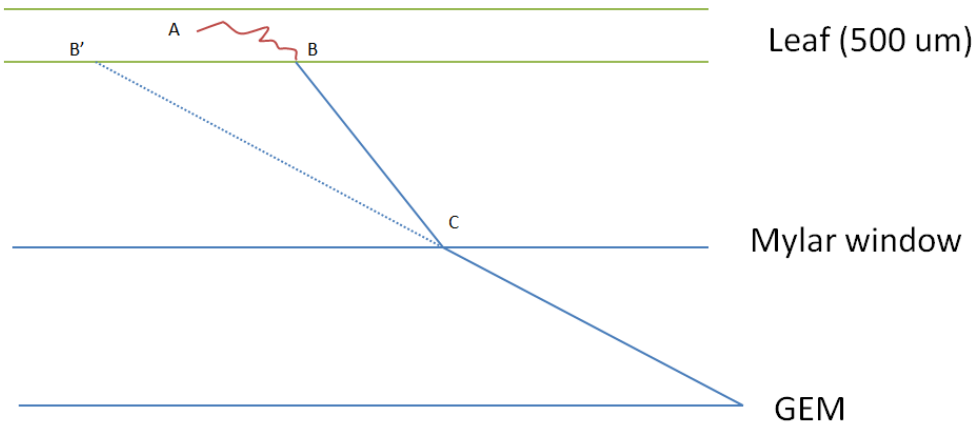

Figure.65 Illustration of the effect of scattering in the window, note that the dimension the figure does not represents the real ratio: A is the original position of the positron, after a zigzag path within the leaf (~500 um thick) the positron exits the leaf at point B and arrives at the detector at C. Because of the scattering in the window, there is a reconstruction error BB' (in the range of mm) which will increase with the gap between the object and the detector. While even there is strong scattering inside the leaf, the spatial uncertainty is below 1 mm, which will not be the dominating effect.

Another limitation encountered in this study was the effect of having a very high trigger rate at the beginning of the leaf imaging studies. The ^{18}F isotope was introduced into the leaf by immersing the petiole in an aqueous solution containing the isotope. This resulted in a high concentration of the isotope at the uptake site, which produced a very high trigger rate from this region and, due to dead time limitations in our data acquisition system, reduced the sensitivity to other areas of the leaf. Having the tracer absorbed farther away from the region of interest of the plant would improve this situation and may also provide additional information about the plant physiology, uptake and metabolism.

In addition, the readout of the detector system was triggered by the signal produced on the bottom of the bottom GEM foil, which does not provide a very precise determination of the arrival time of the first charge clusters drifting in from the drift gap. A possible improvement to this would be to coat the top surface of the top GEM with a photosensitive material such as cesium iodide and use this as a photocathode to detect scintillation light produced in the gas. This could work particularly well for bright scintillating gases such as CF_4 [98]and could provide a prompt signal on the readout pads that could be used as fast trigger for the data acquisition. This is also a possibility we wish to explore in the future.

Finally, we used ^{18}F for most of our measurements even though it has the lowest positron energies of the common PET isotopes, and thus is expected to produce the poorest resolution in this type of detector. Several ^{11}C tracers have already been developed for plant studies [86, 99, 100], and the higher positron energies should produce better results. However, due to the count rate limitations of our readout electronics, we needed the five times longer half-life of ^{18}F to acquire sufficient statistics. With future upgrades to our data acquisition system, we expect to be able to more fully evaluate the performance of the detector with other isotopes.

While we have identified a number of inherent challenges with this technique, we feel that there is room for substantial improvement beyond these initial studies, some of which are

given above. Directly measuring the emitted positrons from PET isotopes used in plant imaging will improve the quantitation in determining the tracer concentration and also improve the overall sensitivity when combined with PET. The main area for improvement for positron imaging would be to reduce the contribution from multiple scattering in the gas and detector window, improve the timing resolution, and reduce the dead time in the readout system.

5.5 Conclusions

A GEM detector system has been studied for directly measuring positrons from PET isotopes that can be used to image plants. This technique has the possibility for improving both the quantitation in determining the tracer concentration and the efficiency for imaging plants with PET, as well as providing an alternative means for producing images from positron emitting isotopes. It was shown that the detector has sufficient intrinsic resolution to produce images with better resolution than conventional PET. However, the effects of multiple scattering for low energy positrons in the current GEM design degrades the resolution to be somewhat worse than PET when the object is placed in contact with the detector, and degrades rapidly with increasing distance from the detector. There are a number of possibilities that can be used to overcome these limitations which we intend to explore in future studies.

Chapter 6

A Time-of-Flight Neutron Activation Method for Measuring Trace Element Concentrations in vivo

6.1 Introduction

In the spirit of investigating complementary and potentially multimodal imaging techniques to study normal and pathological processes in the human body, we have studied the feasibility of an imaging approach that might for the first time assess elemental composition non-invasively. Substantial evidence now exists that trace element concentrations in normal and diseased tissue can be substantially different for elements such as copper, calcium, iron and zinc[101]. The evidence covers a broad range of disease from viral hepatic disease to cancer of the lung, colon, liver and breast, with concentration difference up to a factor of 2 or more. Thus it is of great interest to explore the extent to which these differences could serve as unique new biomarkers of cancer and other diseases. However, in vivo trace element analysis has not been pursued in an intensive way because there are not yet any clinically feasible methods – techniques such as x-ray fluorescence require unacceptably high levels of radiation and are most often used with thin samples. A group at Duke University has proposed a method to measure trace element concentration in vivo called Neutron Stimulated Emission Computed Tomography [102] (NSECT), which is similar to SPECT imaging with the principal difference that the radioactivity is generated within the body by the neutron source, instead of via the injection of a radiotracer. This approach has notable limitations especially in sensitivity. Here we propose a new technique based on neutron activation that not only is expected to substantially improve the sensitivity, but also provides the spatial distribution of trace elements in a direct way. The proposed method will enable a quantitative measurement of concentrations for a multitude of elements simultaneously.

6.2 Method

The basic idea is a form of associated particle imaging [103]. As depicted in Figure 66 below, a beam of neutrons is created in such a way that the direction, speed and emission time of each neutron is known. When a neutron enters the tissue, it can scatter off and excite an atomic nucleus, which responds by emitting characteristic gamma rays. A gamma-ray detector outside

the subject measures the energy and arrival time of this gamma ray. The energy of the gamma ray conveys the isotopic identity of the nucleus that emitted it, since only certain quantum levels can be excited in any given isotope. The elapsed time between the neutron emission and gamma detection is closely related to the time-of-flight of the neutron, which can be converted to distance because of the known, fixed speed of the neutron. Thus, not only can the isotopic identity of the excited nucleus be determined, but also its location in three dimensions – the direction of emission given by an appropriately outfitted neutron generator, and the distance along this direction from the time-of-flight information. The result is an imaging system that can provide the spatial distribution of the neutron-excitable elements in the subject, as well as a quantitative measure of their concentrations.

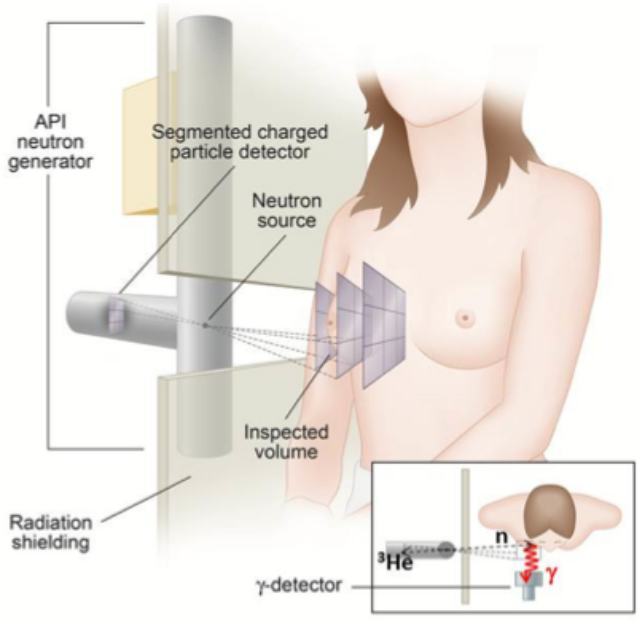

Fig. 66 The proposed associated particle neutron imaging system, as set up for breast imaging. The inset is a top view that shows the back-to-back emission of a neutron (n) and an associated helium-3 particle (^3He) along with the induced gamma ray (γ) from an atomic nucleus.

Specifically, monoenergetic neutrons are produced using a compact neutron generator, which could utilize one of the following fusion reactions:

$$(1)\quad {}^2_1D + {}^3_1T \longrightarrow {}^4_2He(3.5MeV) + n(14.1MeV)$$

$$(2)\quad {}^2_1D + {}^2_1D \xrightarrow{50\%} {}^3_1T(1.01MeV) + p(3.02MeV)$$
$$\xrightarrow{50\%} {}^3_2He(0.82MeV) + n(2.5MeV)$$

We choose the 2.5 MeV neutron because (a) it eliminates the background from C, N and O which require higher excitation energies, (b) most trace elements of interest have low lying excited states which are accessible with neutron inelastic scattering, and (c) the lower energy leads to a >2x reduction neutron speed and a corresponding improvement in spatial resolution for a given detector time resolution. Furthermore, 2.5 MeV neutrons still have relatively good penetration power.

As illustrated in the equations above, the neutrons are generated by accelerating deuterium ions into a deuterium target. In the ensuing fusion reaction, a 2.5 MeV neutron and an associated 0.8 MeV helium-3 particle are produced back-to-back, in a way analogous to PET imaging. The direction and emission time of each neutron is measured by detecting the helium-3 particle using a position-sensitive particle detector. The energy resolving capability of the particle detector is used to distinguish helium-3 particles from other reaction products. The time delay between detecting the helium-3 particle and detecting the neutron-induced characteristic gamma ray from a nuclear de-excitation determines the neutron time-of-flight. Since we know that 2.5 MeV neutrons travel at 2.2 cm/ns, and gamma rays at 30 cm/ns, the time delay can be used to determine the distance travelled by the neutron along its path, and hence to determine the 3-dimensional location of the interaction. Standard gamma spectroscopic methods are used to separate out and quantify the various elements of interest by analyzing appropriate gamma lines. An important feature is that the timing information can be used to reject background events originating outside the volume of interest, reducing the need for bulky shielding of the gamma-ray detectors.

Proof of concept simulations have been done with Geant4 [97]. The figure below shows the result of Geant4 simulation of a beam of 2.5 MeV neutrons impacting the center of a 10 cm cube of water. The water cube contains 6 major trace elements with their actual concentration in vivo. The energy spectrum is of the neutron-induced, inelastic scattering gamma rays emitted from a 3 cm cube target volume. The neutron fluence used would produce 10 mSv effective radiation dose with 10% gamma detection efficiency.

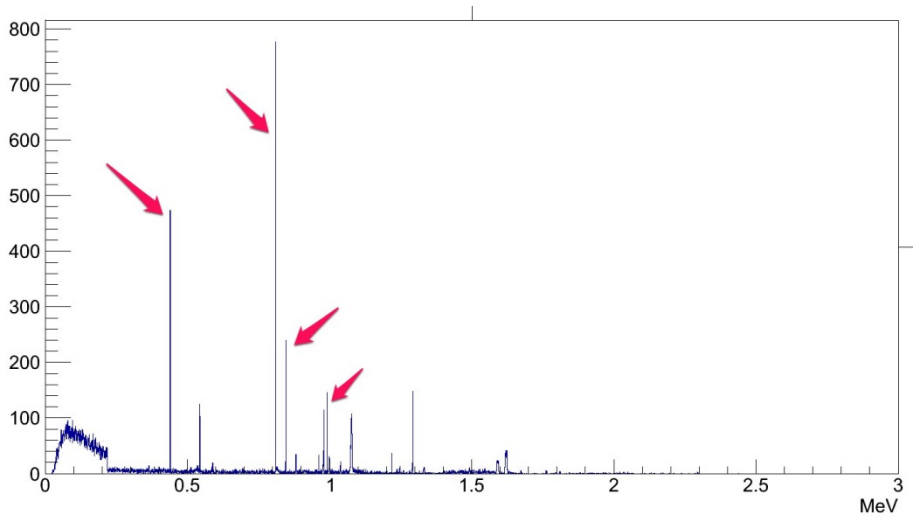

Figure.67 Energy spectrum of gammas from neutron inelastic scattering

Since neutron scattering would make neutrons deviate from their original path. This effect has been evaluated with simulation. A beam of neutrons with 1 cm^2 profile was created and shot to a water cube (similar to the last simulation described above), and a spatial distribution of the 992-keV gamma (characteristic gamma for Zinc) emission points was plotted. The result show neutron scattering in this geometry produces only ~10% of these gammas outside the 1 cm^2 beam, suggesting that the effect of scattering on spatial resolution is modest.

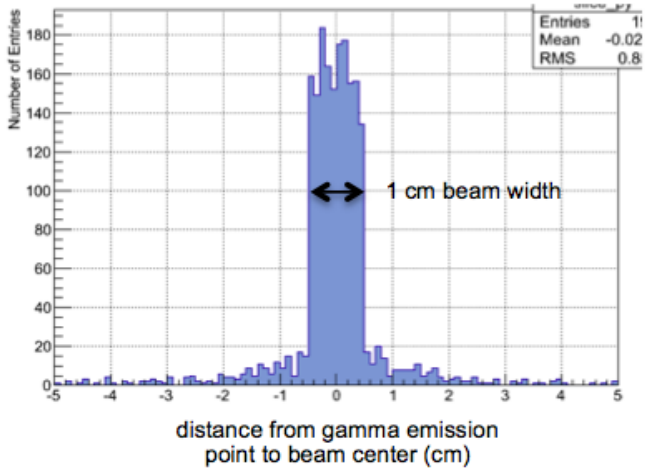

Figure.68 Histogram of 992 keV gamma emission points for a 2.5 MeV incident neutron beam with 1 cm^2 profile

Compared to NSECT, the fundamental improvement of our technique is that we know the maximum possible information from every emitted neutron (direction, time and energy), so faithful imaging requires far fewer neutrons. The increase in sensitivity has a significant impact on clinical feasibility.

6.3 Dose Evaluation

A major potential limitation of this technique is radiation dose since the cross section of neutron inelastic scattering is usually very small. For most elements the cross section is below 1 barn [104]. To evaluate the dose in a realistic scenario, the simulation is based on a whole body human phantom with Geant4. The phantom is a male MIRD mathematical phantom [105]. A large germanium block is used to simulate the detector. The detector has the same vertical axis as the body and with an inner radius of 20 cm, an outer radius of 60 cm and length of 160 cm. It covers 150 degrees of the solid angle to minimize direct illumination of neutrons to the detector.

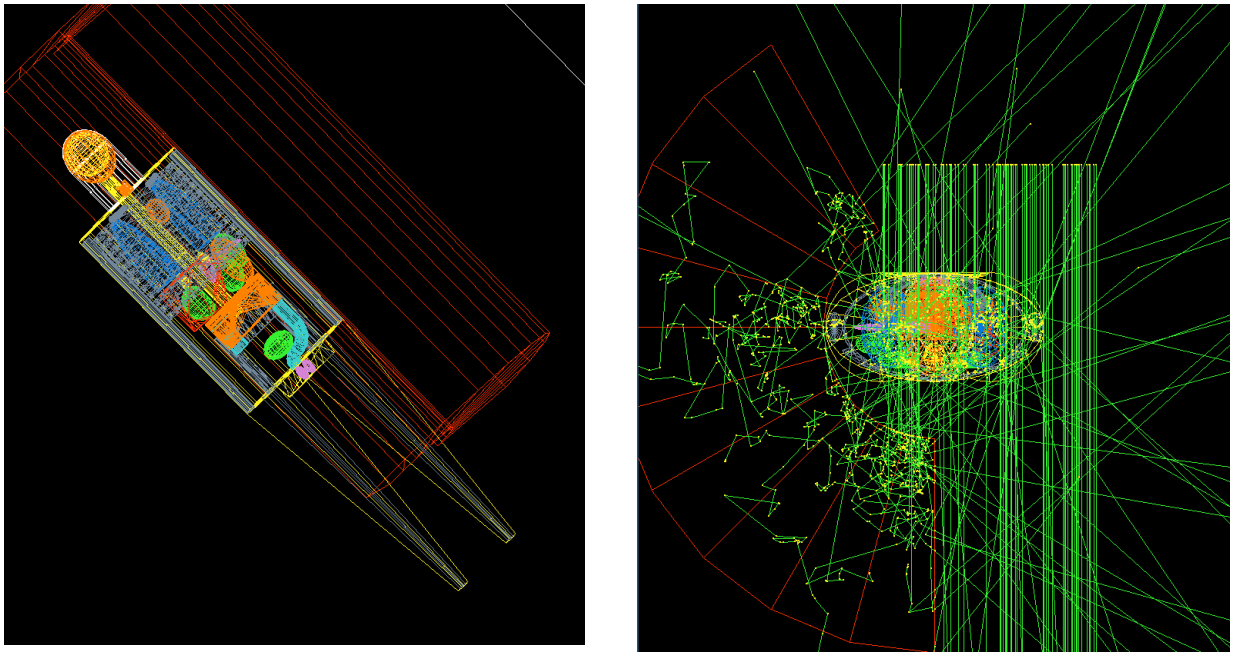

Figure.69 The MIRD body phantom and the detector tube (red), the green lines shows the incident neutron beam

The target clinical application in this simulation is iron overload in liver, which is also known as haemochromatosis. In normal tissue, the concentration of iron is ~50 ppm while for iron overload patient, the concentration of iron in liver could be as high as 2000 ppm [106]. In this simulation, liver is filled with 98% water and 2% of iron. The usage of high iron

concentration is to reduce the simulation time. All the other organs are filled with water except bones. The neutron source has 40 by 40 cm beam profile and 2.5 MeV energy.

Geant4 “Shielding” physics list [107] is used to model the neutron physics. It is originally developed for neutron penetration studies and ion-ion collisions. And it covers all the hadron physics as well as electromagnetic interactions.

Secondary gamma photons are detected by the Germanium detector and the time and energy information are recorded. The timing is determined by the arrival time of the first hit and energy is obtained by sum up the energy deposited of all hits for each gamma event. The energy spectrum is shown below.

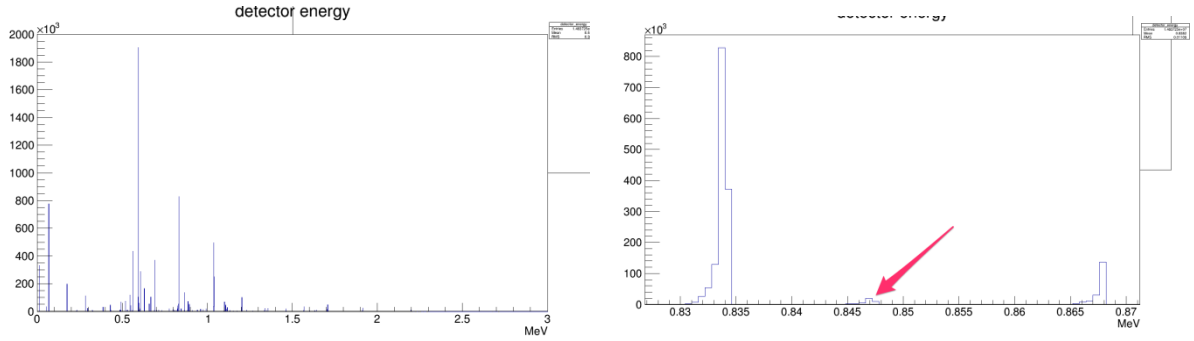

Figure.70 Left: energy spectrum of the gammas from 50 million incident neutrons, all the big peaks are the characteristic gammas of germanium. Right: zoom in view of the spectrum where the red arrow pointing out the 847 keV peak from Fe-56

If we spread the spectrum in another dimension, which is time, the characteristic gamma peak from iron can be separated from the background now.

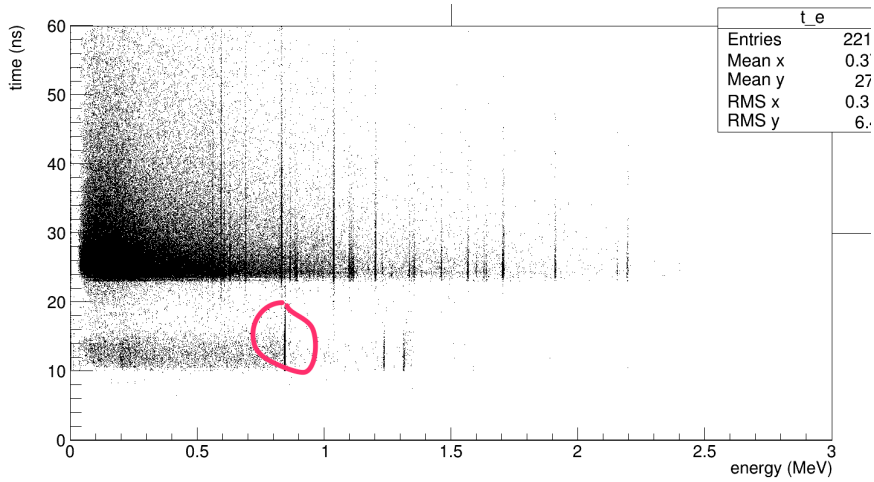

Figure.71 2D histogram (time and energy) of the secondary gammas, the red circle shows the F-56 peak

Image could be reconstructed by selecting gammas with energy of 847 keV. The image is made by simply back projecting the gammas based on the timing information.

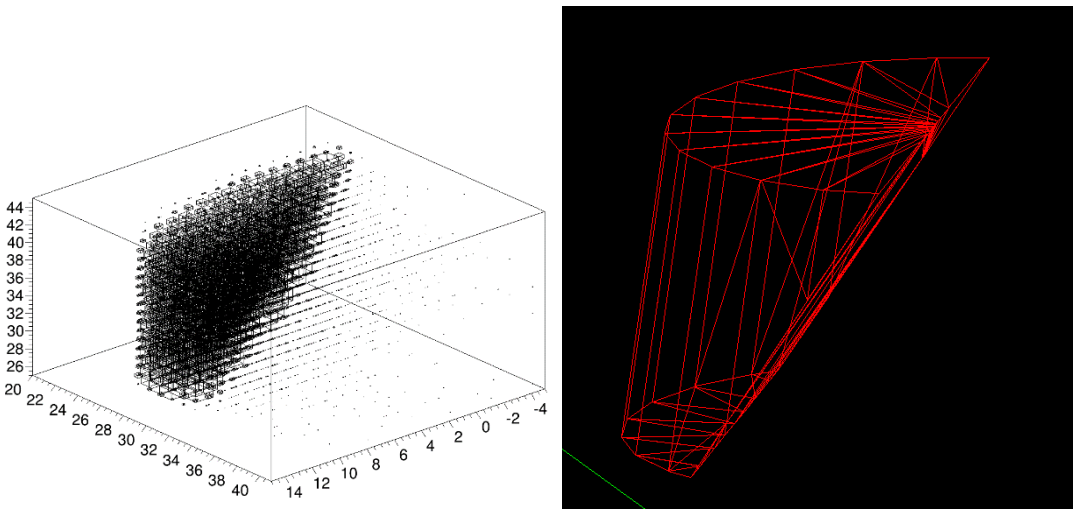

Figure.72 Left: the reconstructed image of liver based on the characteristic gammas from Fe-56; Right: the analytical model for liver for comparison

With the setup described above, 50 million neutrons create about $\mathbf{7\times10^{-3}}$ mSv effective dose (after considering the tissue weighting factor). And ~5000 gammas at the Fe-56 peak (847 keV) are created and about 1000 gammas are detected. So with 50 ppm iron concentration and 10 mSv effective dose, we can expect ~18000 gammas overall and about 3600 gammas detected. The volume of the liver is about 1500 cc, which gives about 2.4 counts/ cm^3 in the tissue.

6.4 Conclusion

In conclusion, we demonstrated the possibility of using fast neutrons to non-invasively detect the trace element in vivo. It has the potential of build a 3D concentration map of trace elements and the result can be quantitative. A remaining concern of this technique is the radiation dose. Gamma detectors with big solid angle coverage are required for high sensitivity and trading off resolution (using big voxels) might be necessary.

References:

[1] T. Ido, C. N. Wan, V. Casella, J. S. Fowler, A. P. Wolf, M. Reivich*, et al.*, "Labeled 2-deoxy-D-glucose analogs. 18F-labeled 2-deoxy-2-fluoro-D-glucose, 2-deoxy-2-fluoro-D-mannose and 14C-2-deoxy-2-fluoro-D-glucose," *Journal of Labelled Compounds and Radiopharmaceuticals,* vol. 14, pp. 175-183, 1978.

[2] D. Schulz, S. Southekal, S. S. Junnarkar, J. F. Pratte, M. L. Purschke, S. P. Stoll*, et al.*, "Simultaneous assessment of rodent behavior and neurochemistry using a miniature positron emission tomograph," *Nat Methods,* vol. 8, pp. 347-52, Apr 2011.

[3] S. H. Maramraju, S. D. Smith, S. S. Junnarkar, D. Schulz, S. Stoll, B. Ravindranath*, et al.*, "Small animal simultaneous PET/MRI: initial experiences in a 9.4 T microMRI," *Phys Med Biol,* vol. 56, pp. 2459-80, Apr 21 2011.

[4] S. H. Maramraju, S. D. Smith, S. Rescia, S. Stoll, M. Budassi, P. Vaska*, et al.*, "Electromagnetic Interactions in a Shielded PET/MRI System for Simultaneous PET/MR Imaging in 9.4 T: Evaluation and Results," *IEEE Transactions on Nuclear Science,* vol. 59, pp. 1892-1899, 2012.

[5] B. Ravindranath, S. S. Junnarkar, M. L. Purschke, S. H. Maramraju, S. S. Southekal, S. P. Stoll*, et al.*, "3D tomographic wrist scanner for non-invasive determination of input function," pp. 2917-2919, 2009.

[6] B. Ravindranath, S. S. Junnarkar, M. L. Purschke, S. H. Maramraju, X. Hong, D. Tomasi*, et al.*, "Results from Prototype II of the BNL Simultaneous PET-MRI Dedicated Breast Scanner," *2009 Ieee Nuclear Science Symposium Conference Record, Vols 1-5,* pp. 3315-3317, 2009.

[7] M. Budassi, S. Stoll, M. L. Purschke, B. Ravindranath, J. Fried, T. Cao*, et al.*, "First results from the BNL plant imaging system," pp. 3530-3532, 2012.

[8] J.-F. Pratte, S. Junnarkar, G. Deptuch, J. Fried, P. O'Connor, V. Radeka*, et al.*, "The RatCAP front-end ASIC," pp. 19-25, 2007.

[9] M. Budassi, "Development and Characterization of High-Resolution Modular PET Imaging Systems," *Ph.D. thesis,* 2015.

[10] J. S. Karp, S. Surti, M. E. Daube-Witherspoon, and G. Muehllehner, "Benefit of time-of-flight in PET: experimental and clinical results," *J Nucl Med,* vol. 49, pp. 462-70, Mar 2008.

[11] A. P. Jeavons, R. A. Chandler, and C. A. R. Dettmar, "A 3D HIDAC-PET camera with sub-millimetre resolution for imaging small animals," *IEEE Transactions on Nuclear Science,* vol. 46, pp. 468-473, 1999.

[12] P. Vaska, A. Dragone, W. Lee, D. H. Kim, J. F. Pratte, Y. G. Cui*, et al.*, "A prototype CZT-based PET scanner for high resolution mouse brain imaging," pp. 3816-3819, 2007.

[13] S. Matej and R. M. Lewitt, "Practical considerations for 3-D image reconstruction using spherically symmetric volume elements," *IEEE Trans Med Imaging,* vol. 15, pp. 68-78, 1996.

[14] L. M. Popescu and R. M. Lewitt, "Ray tracing through a grid of blobs," vol. 6, pp. 3983-3986, 2004.

[15] K. Saha, K. J. Straus, Y. Chen, and S. J. Glick, "Iterative reconstruction using a Monte Carlo based system transfer matrix for dedicated breast positron emission tomography," *Journal of Applied Physics,* vol. 116, p. 084903, 2014.

[16] J. Qi, R. M. Leahy, S. R. Cherry, A. Chatziioannou, and T. H. Farquhar, "High-resolution 3D Bayesian image reconstruction using the microPET small-animal scanner," *Physics in Medicine and Biology,* vol. 43, pp. 1001-1013, 1998.
[17] R. L. Siddon, "Fast calculation of the exact radiological path for a three-dimensional CT array," *Med Phys,* vol. 12, pp. 252-5, Mar-Apr 1985.
[18] F. Jacobs, E. Sundermann, B. De Sutter, M. Christiaens, and I. Lemahieu, "A fast algorithm to calculate the exact radiological path through a pixel or voxel space," *Journal of computing and information technology,* vol. 6, pp. 89-94, 1998.
[19] C. Schretter, "A fast tube of response ray-tracer," *Medical Physics,* vol. 33, p. 4744, 2006.
[20] S. Moehrs, M. Defrise, N. Belcari, A. D. Guerra, A. Bartoli, S. Fabbri*, et al.*, "Multi-ray-based system matrix generation for 3D PET reconstruction," *Phys Med Biol,* vol. 53, pp. 6925-45, Dec 7 2008.
[21] J. Zhou and J. Qi, "Fast and efficient fully 3D PET image reconstruction using sparse system matrix factorization with GPU acceleration," *Phys Med Biol,* vol. 56, pp. 6739-57, Oct 21 2011.
[22] J. Y. Cui, G. Pratx, S. Prevrhal, and C. S. Levin, "Fully 3D list-mode time-of-flight PET image reconstruction on GPUs using CUDA," *Med Phys,* vol. 38, pp. 6775-86, Dec 2011.
[23] M. A. Nassiri, S. Hissoiny, J.-F. Carrier, and P. Després, "Fast GPU-based computation of the sensitivity matrix for a PET list-mode OSEM algorithm," *Physics in Medicine and Biology,* vol. 57, p. 6279, 2012.
[24] J. Cui, G. Pratx, B. Meng, and C. S. Levin, "Distributed MLEM: an iterative tomographic image reconstruction algorithm for distributed memory architectures," *IEEE Trans Med Imaging,* vol. 32, pp. 957-67, May 2013.
[25] C. Cloquet, F. C. Sureau, M. Defrise, G. Van Simaeys, N. Trotta, and S. Goldman, "Non-Gaussian space-variant resolution modelling for list-mode reconstruction," *Phys Med Biol,* vol. 55, pp. 5045-66, Sep 7 2010.
[26] V. Y. Panin, F. Kehren, C. Michel, and M. Casey, "Fully 3-D PET reconstruction with system matrix derived from point source measurements," *IEEE Transactions on Medical Imaging,* vol. 25, pp. 907-921, 2006.
[27] A. Rahmim, J. Qi, and V. Sossi, "Resolution modeling in PET imaging: theory, practice, benefits, and pitfalls," *Med Phys,* vol. 40, p. 064301, Jun 2013.
[28] M. N. Wernick, and John N. Aarsvold, "Emission tomography: the fundamentals of PET and SPECT," *Academic Press,* 2004.
[29] A. P. L. Dempster, Nan M.; Rubin, Donald B., "Maximum Likelihood from Incomplete Data via the EM Algorithm " *Journal of the Royal Statistical Society,* 1977.
[30] C. F. J. Wu, "On the Convergence Properties of the EM Algorithm," *The Annals of Statistics,* vol. 11, pp. 95-103, 1983.
[31] K. Lange and R. Carson, "EM reconstruction algorithms for emission and transmission tomography," *J Comput Assist Tomogr,* vol. 8, pp. 306-16, Apr 1984.
[32] L. Xu and M. I. Jordan, "On Convergence Properties of the EM Algorithm for Gaussian Mixtures," *Neural Computation,* vol. 8, pp. 129-151, 1996.
[33] H. M. Hudson and R. S. Larkin, "Accelerated image reconstruction using ordered subsets of projection data," *IEEE Trans Med Imaging,* vol. 13, pp. 601-9, 1994.

[34] C. a. H. E. J, "Quantitation in positron emission computed tomography: 7. A technique to reduce noise in accidental coincidence measurements and coincidence efficiency calibration," *J. Comput. Assist. Tomogr,* vol. 10, pp. 845–50, 1986
[35] R. Badawi, M. Miller, D. Bailey, and P. Marsden, "Randoms variance reduction in 3D PET," *Physics in medicine and biology,* vol. 44, p. 941, 1999.
[36] J. S. Karp, G. Muehllehner, H. Qu, and X. H. Yan, "Singles transmission in volume-imaging PET with a 137Cs source," *Phys Med Biol,* vol. 40, pp. 929-44, May 1995.
[37] P. E. Kinahan, D. W. Townsend, T. Beyer, and D. Sashin, "Attenuation correction for a combined 3D PET/CT scanner," *Med Phys,* vol. 25, pp. 2046-53, Oct 1998.
[38] H. Zaidi, M. L. Montandon, and D. O. Slosman, "Magnetic resonance imaging-guided attenuation and scatter corrections in three-dimensional brain positron emission tomography," *Med Phys,* vol. 30, pp. 937-48, May 2003.
[39] I. Bezrukov, F. Mantlik, H. Schmidt, B. Scholkopf, and B. J. Pichler, "MR-Based PET attenuation correction for PET/MR imaging," *Semin Nucl Med,* vol. 43, pp. 45-59, Jan 2013.
[40] H. Zaidi, N. Ojha, M. Morich, J. Griesmer, Z. Hu, P. Maniawski*, et al.*, "Design and performance evaluation of a whole-body Ingenuity TF PET-MRI system," *Phys Med Biol,* vol. 56, pp. 3091-106, May 21 2011.
[41] B. D. Coombs, J. Szumowski, and W. Coshow, "Two-point Dixon technique for water-fat signal decomposition with B0 inhomogeneity correction," *Magn Reson Med,* vol. 38, pp. 884-9, Dec 1997.
[42] Y. Berker, J. Franke, A. Salomon, M. Palmowski, H. C. Donker, Y. Temur*, et al.*, "MRI-based attenuation correction for hybrid PET/MRI systems: a 4-class tissue segmentation technique using a combined ultrashort-echo-time/Dixon MRI sequence," *J Nucl Med,* vol. 53, pp. 796-804, May 2012.
[43] A. L. Goertzen, Q. Bao, M. Bergeron, E. Blankemeyer, S. Blinder, M. Canadas*, et al.*, "NEMA NU 4-2008 comparison of preclinical PET imaging systems," *J Nucl Med,* vol. 53, pp. 1300-9, Aug 2012.
[44] C. C. Watson, D. Newport, and M. E. Casey, "A single scatter simulation technique for scatter correction in 3D pet," *Three-Dimensional Image Reconstruction in Radiology and Nuclear Medicine,* vol. 4, pp. 255-268, 1996.
[45] J. M. Ollinger, "Model-based scatter correction for fully 3D PET," *Physics in Medicine and Biology,* vol. 41, pp. 153-176, 1996.
[46] C. S. Levin, M. Dahlbom, and E. J. Hoffman, "A Monte Carlo correction for the effect of Compton scattering in 3-D PET brain imaging," *IEEE Transactions on Nuclear Science,* vol. 42, pp. 1181-1185, 1995.
[47] C. H. Holdworth, C. S. Levin, M. Janecek, M. Dahlbom, and E. J. Hoffman, "Performance analysis of an improved 3D PET Monte Carlo simulation and scatter correction," vol. 2, pp. 13/53-13/57, 2000.
[48] C. H. Holdsworth, C. S. Levin, T. H. Farquhar, M. Dahlbom, and E. J. Hoffman, "Investigation of accelerated Monte Carlo techniques for PET simulation and 3D PET scatter correction," *Ieee Transactions on Nuclear Science,* vol. 48, pp. 74-81, Feb 2001.
[49] M. Gaens, J. Bert, U. Pietrzyk, N. J. Shah, and D. Visvikis, "GPU-accelerated Monte Carlo Based Scatter Correction in Brain PET/MR," *2013 Ieee Nuclear Science Symposium and Medical Imaging Conference (Nss/Mic),* pp. 1-3, 2013.

[50] C. C. Watson, "Extension of Single Scatter Simulation to Scatter Correction of Time-of-Flight PET," vol. 5, pp. 2492-2496, 2005.
[51] R. Accorsi, L.-E. Adam, M. E. Werner, and J. S. Karp, "Optimization of a fully 3D single scatter simulation algorithm for 3D PET," *Physics in Medicine and Biology,* vol. 49, pp. 2577-2598, 2004.
[52] Q. Hua, R. Manjeshwar, and K. Thielemans, "A comparative study of multiple scatter estimations in 3D PET," pp. 2700-2702, 2010.
[53] B. Bai, Q. Li, C. H. Holdsworth, E. Asma, Y. C. Tai, A. Chatziioannou*, et al.*, "Model-based normalization for iterative 3D PET image reconstruction," *Phys Med Biol,* vol. 47, pp. 2773-84, Aug 7 2002.
[54] R. D. Badawi and P. K. Marsden, "Developments in component-based normalization for 3D PET," *Phys Med Biol,* vol. 44, pp. 571-94, Feb 1999.
[55] R. D. Badawi, M. A. Lodge, and P. K. Marsden, "Algorithms for calculating detector efficiency normalization coefficients for true coincidences in 3D PET," *Phys Med Biol,* vol. 43, pp. 189-205, Jan 1998.
[56] K. F. K. Matt A. Bernstein, Xiaohong Joe Zhou, "Handbook of MRI Pulse Sequences," *Elsevier,* 2004.
[57] N. L. Christensen, B. E. Hammer, B. G. Heil, and K. Fetterly, "Positron Emission Tomography within a Magnetic-Field Using Photomultiplier Tubes and Lightguides," *Physics in Medicine and Biology,* vol. 40, pp. 691-697, Apr 1995.
[58] R. Slates, S. Cherry, A. Boutefnouchet, S. Yiping, M. Dahlborn, and K. Farahani, "Design of a small animal MR compatible PET scanner," *IEEE Transactions on Nuclear Science,* vol. 46, pp. 565-570, 1999.
[59] R. R. Raylman, S. Majewski, S. K. Lemieux, S. S. Velan, B. Kross, V. Popov*, et al.*, "Simultaneous MRI and PET imaging of a rat brain," *Phys Med Biol,* vol. 51, pp. 6371-9, Dec 21 2006.
[60] M. Imaizumi, S. Yamamoto, M. Kawakami, M. Aoki, E. Sugiyama, Y. Kanai*, et al.*, "Simultaneous imaging of magnetic resonance imaging and positron emission tomography by means of MRI-compatible optic fiber-based PET: a validation study in ex vivo rat brain," *Jpn J Radiol,* vol. 27, pp. 252-6, Jul 2009.
[61] A. J. Lucas, R. C. Hawkes, P. Guerra, R. E. Ansorge, R. E. Nutt, J. C. Clark*, et al.*, "Development of a combined microPET-MR system," pp. 2345-2348, 2006.
[62] S. Takamatsu, S. Yamamoto, H. Murayama, and K. Minato, "Design and construction of a multi-slice, depth-of-interaction MR-compatible PET," vol. 6, pp. 3810-3813, 2004.
[63] H. F. Wehrl, M. Hossain, K. Lankes, C. C. Liu, I. Bezrukov, P. Martirosian*, et al.*, "Simultaneous PET-MRI reveals brain function in activated and resting state on metabolic, hemodynamic and multiple temporal scales," *Nat Med,* vol. 19, pp. 1184-9, Sep 2013.
[64] C. Catana, D. Procissi, Y. Wu, M. S. Judenhofer, J. Qi, B. J. Pichler*, et al.*, "Simultaneous in vivo positron emission tomography and magnetic resonance imaging," *Proc Natl Acad Sci U S A,* vol. 105, pp. 3705-10, Mar 11 2008.
[65] H. S. Yoon, G. B. Ko, S. I. Kwon, C. M. Lee, M. Ito, I. Chan Song*, et al.*, "Initial results of simultaneous PET/MRI experiments with an MRI-compatible silicon photomultiplier PET scanner," *J Nucl Med,* vol. 53, pp. 608-14, Apr 2012.

[66] S. Yamamoto, T. Watabe, H. Watabe, M. Aoki, E. Sugiyama, M. Imaizumi, *et al.*, "Simultaneous imaging using Si-PM-based PET and MRI for development of an integrated PET/MRI system," *Phys Med Biol,* vol. 57, pp. N1-13, Jan 21 2012.
[67] J. Wehner, B. Weissler, P. Dueppenbecker, P. Gebhardt, D. Schug, W. Ruetten, *et al.*, "PET/MRI insert using digital SiPMs: Investigation of MR-compatibility," *Nuclear Instruments and Methods in Physics Research Section A: Accelerators, Spectrometers, Detectors and Associated Equipment,* vol. 734, pp. 116-121, 2014.
[68] M. L. Purschke, "Online and Offline Computing systems in the PHENIX experiment," *arXiv preprint hep-ex/0305103,* 2003.
[69] M. L. Purschke, M. Budassi, T. Cao, J. Fried, E. Gualtieri, S. S. Junnarkar, *et al.*, "Readout technologies for the BNL-UPenn MRI-compatible PET scanner for rodents," pp. 617-620, 2011.
[70] R. Brun and F. Rademakers, "ROOT — An object oriented data analysis framework," *Nuclear Instruments and Methods in Physics Research Section A: Accelerators, Spectrometers, Detectors and Associated Equipment,* vol. 389, pp. 81-86, 1997.
[71] B. Ravindranath, "Development of a Simultaneous PET-MRI Breast Scanner," *Ph.D. thesis,* 2011.
[72] S. Southekal, "Strategies for Quantitative Neuroimaging with the Rat Conscious Animal PET (RatCAP)," *Ph.D. thesis,* 2009.
[73] "University of Washington. SimSET Home Page. Available at http://depts.washington.edu/simset/html/simset_main.html. Accessed 20 Oct 2015."
[74] S. Jan, G. Santin, D. Strul, S. Staelens, K. Assie, D. Autret, *et al.*, "GATE: a simulation toolkit for PET and SPECT," *Phys Med Biol,* vol. 49, pp. 4543-61, Oct 7 2004.
[75] R. Pordes, D. Petravick, B. Kramer, D. Olson, M. Livny, A. Roy, *et al.*, "The open science grid," *Journal of Physics: Conference Series,* vol. 78, p. 012057, 2007.
[76] K. Thielemans, C. Tsoumpas, S. Mustafovic, T. Beisel, P. Aguiar, N. Dikaios, *et al.*, "STIR: software for tomographic image reconstruction release 2," *Phys Med Biol,* vol. 57, pp. 867-83, Feb 21 2012.
[77] L. M. Popescu, S. Matej, and R. M. Lewitt, "Iterative image reconstruction using geometrically ordered subsets with list-mode data," vol. 6, pp. 3536-3540, 2004.
[78] "Performance Measurements for Small Animal Positron Emission Tomographs," *NEMA Standards Publication NU4-2008ed: National Electrical Manufactures Association,* 2008.
[79] S. C. Strother, M. E. Casey, and E. J. Hoffman, "Measuring PET scanner sensitivity: relating countrates to image signal-to-noise ratios using noise equivalents counts," *IEEE Transactions on Nuclear Science,* vol. 37, pp. 783-788, 1990.
[80] T. Cao, B. Azmoun, B. Babst, M. Blatnik, M. L. Purschke, S. Stoll, *et al.*, "A Study of a GEM Tracking Detector for Imaging Positrons from PET Radioisotopes in Plants," *IEEE Transactions on Nuclear Science,* vol. 61, pp. 2464-2471, 2014.
[81] S. Ruben, W. Z. Hassid, and M. D. Kamen, "Radioactive Carbon in the Study of Photosynthesis," *Journal of the American Chemical Society,* vol. 61, pp. 661-663, 1939.
[82] S. Fujimaki, N. Suzui, N. S. Ishioka, N. Kawachi, S. Ito, M. Chino, *et al.*, "Tracing cadmium from culture to spikelet: noninvasive imaging and quantitative characterization of absorption, transport, and accumulation of cadmium in an intact rice plant," *Plant Physiol,* vol. 152, pp. 1796-806, Apr 2010.

[83] K. e. al, "Real Time Visualization of 13N-Translocation in Rice under Different Environmental Conditions Using Positron Emitting Tracer Imaging System," *Plant Physiology,* vol. 125, pp. 1743-53, 2001.
[84] S. Jahnke, M. I. Menzel, D. van Dusschoten, G. W. Roeb, J. Buhler, S. Minwuyelet*, et al.*, "Combined MRI-PET dissects dynamic changes in plant structures and functions," *Plant J,* vol. 59, pp. 634-44, Aug 2009.
[85] M. R. Kiser, C. D. Reid, A. S. Crowell, R. P. Phillips, and C. R. Howell, "Exploring the transport of plant metabolites using positron emitting radiotracers," *HFSP J,* vol. 2, pp. 189-204, Aug 2008.
[86] A. P. F. M.R. Thorpe, M.M. Herth, R.A. Ferrieri. , "C-11-imaging: methyl jasmonate moves in both phloem and xylem, promotes transport of jasmonate, and of photoassimilate even after proton transport is decoupled," *Planta* vol. 226, pp. 541-51, 2007.
[87] B. A. Babst, A. A. Karve, and T. Judt, "Radio-metabolite analysis of carbon-11 biochemical partitioning to non-structural carbohydrates for integrated metabolism and transport studies," *Plant Cell Physiol,* vol. 54, pp. 1016-25, Jun 2013.
[88] M. Budassi, et al., "Imaging performance of the BNL PET imaging system for plant science," pp. 1-3, 2013.
[89] D. L. Alexoff, S. L. Dewey, P. Vaska, S. Krishnamoorthy, R. Ferrieri, M. Schueller*, et al.*, "PET imaging of thin objects: measuring the effects of positron range and partial-volume averaging in the leaf of Nicotiana tabacum," *Nucl Med Biol,* vol. 38, pp. 191-200, Feb 2011.
[90] A. Breskin, "Advances in gas avalanche radiation detectors for biomedical applications," *Nuclear Instruments and Methods in Physics Research Section A: Accelerators, Spectrometers, Detectors and Associated Equipment,* vol. 454, pp. 26-39, 2000.
[91] H. Wu and Y. C. Tai, "A novel phoswich imaging detector for simultaneous beta and coincidence-gamma imaging of plant leaves," *Phys Med Biol,* vol. 56, pp. 5583-98, Sep 7 2011.
[92] A. G. Weisenberger, B. Kross, S. Lee, J. McKisson, J. E. McKisson, W. Xi*, et al.*, "PhytoBeta imager: a positron imager for plant biology," *Phys Med Biol,* vol. 57, pp. 4195-210, Jul 7 2012.
[93] F. Sauli, "GEM: A new concept for electron amplification in gas detectors," *Nuclear Instruments and Methods in Physics Research Section A: Accelerators, Spectrometers, Detectors and Associated Equipment,* vol. 386, pp. 531-534, 1997.
[94] C. Altunbas, M. Capéans, K. Dehmelt, J. Ehlers, J. Friedrich, I. Konorov*, et al.*, "Construction, test and commissioning of the triple-gem tracking detector for compass," *Nuclear Instruments and Methods in Physics Research Section A: Accelerators, Spectrometers, Detectors and Associated Equipment,* vol. 490, pp. 177-203, 2002.
[95] M. Chefdeville, "RD51, a world-wide collaboration for the development of Micro Pattern Gaseous Detectors," *Journal of Physics: Conference Series,* vol. 309, p. 012017, 2011.
[96] M. L. Purschke, "Readout of GEM stacks with the CERN SRS system," in *Real Time Conference (RT), 2012 18th IEEE-NPSS*, 2012, pp. 1-3.
[97] D. H. Wright, "Geant4: A Simulation Toolkit," 2002.
[98] B. Azmoun, M. Rumore, J. Sinsheimer, N. Smirnov, S. Stoll, and C. Woody, "A measurement of scintillation in CF<inf>f4</inf> using GEM foils and a CsI photocathode," pp. 623-626, 2007.

[99] A. E. Reid, S. W. Kim, B. Seiner, F. W. Fowler, J. Hooker, R. Ferrieri*, et al.*, "Radiosynthesis of C-11 labeled auxin (3-indolyl[1-11C]acetic acid) and its derivatives from gramine," *Journal of Labelled Compounds and Radiopharmaceuticals,* vol. 54, pp. 433-437, 2011.
[100] M. Best, A. N. Gifford, S. W. Kim, B. Babst, M. Piel, F. Rösch*, et al.*, "Rapid radiosynthesis of [11C] and [14C]azelaic, suberic, and sebacic acids for in vivo mechanistic studies of systemic acquired resistance in plants," *Journal of Labelled Compounds and Radiopharmaceuticals,* vol. 55, pp. 39-43, 2012.
[101] K. Gurusamy, "Trace element concentration in primary liver cancers--a systematic review," *Biol Trace Elem Res,* vol. 118, pp. 191-206, Sep 2007.
[102] C. E. Floyd, Jr., J. E. Bender, A. C. Sharma, A. Kapadia, J. Xia, B. Harrawood*, et al.*, "Introduction to neutron stimulated emission computed tomography," *Phys Med Biol,* vol. 51, pp. 3375-90, Jul 21 2006.
[103] S. Pesente, G. Nebbia, M. Lunardon, G. Viesti, S. Blagus, K. Nad*, et al.*, "Tagged neutron inspection system (TNIS) based on portable sealed generators," *Nuclear Instruments and Methods in Physics Research Section B: Beam Interactions with Materials and Atoms,* vol. 241, pp. 743-747, 2005.
[104] "National Nuclear Data Center," *http://www.nndc.bnl.gov/*.
[105] S. Guatelli, B. Mascialino, M. G. Pia, and W. Pokorski, "Geant4 Anthropomorphic Phantoms," pp. 1359-1362, 2006.
[106] A. J. Kapadia, G. D. Tourassi, A. C. Sharma, A. S. Crowell, M. R. Kiser, and C. R. Howell, "Experimental detection of iron overload in liver through neutron stimulated emission spectroscopy," *Phys Med Biol,* vol. 53, pp. 2633-49, May 21 2008.
[107] J. Apostolakis, G. Folger, V. Grichine, A. Howard, V. Ivanchenko, M. Kosov*, et al.*, "GEANT4 Physics Lists for HEP," pp. 833-836, 2008.